High Bandwidth CMOS Magnetic Sensors Based on the Miniaturized Circular Vertical Hall Device

PAR

Mirjana BANJEVIC

EPFL

ÉCOLE POLYTECHNIQUE
FÉDÉRALE DE LAUSANNE

Suisse
2011

To the memory of my grandfather

Acknowledgments

_____

First of all, I would like to thank my thesis adviser Prof. Radivoje S. Popovic for giving me the opportunity to pursue research in his group and learn from him. I appreciate his valuable input in many aspects of my work. I am thankful to my thesis co-adviser Prof. Jürgen Brugger for helping me through the final year of my thesis.

I owe immense gratitude to Dr. Beat Furrer for numerous fruitful discussions we had, as well as for his support and availability during the work on the Marie Curie project. I am greatly indebted to him for his willingness to read and comment on the thesis manuscript.

I am grateful to the committee members Prof. Adrian Ionescu, Prof. Pierre-André Farine, Dr Andreas Friedrich, and Prof. Oliver Paul for their constructive suggestions to improve the quality of the manuscript.

I am indebted to my Master and Diploma thesis adviser Prof. Niksa Tadic for opening the door of microelectronics to me.

Many thanks go to LMIS3 group members: Serge for transferring to me his enthusiasm and love of Hall devices; Jens for sharing his IP on CAD tools with me, many discussions we had, five SMA connectors he gave me, to mention but a few; Pavel for his help with design submissions; Giovanni for his valuable advices on many subjects; Ozge, my officemate, and Malika, for their help and friendship during my first year in Lausanne, then Bernard, Cristiano, Chen, David, Fred, Gilles, Jorge, Kota, Marc, Marek, Milan and Paul, and our dear Ilona.

My profound gratitude goes to my friends in Lausanne who made these years memorable: Marija for being the best friend one can imagine, my dearest neighbor Ivana T. , Zorana, Ivana J. , my "sister" Jelena, my half-flatmates Tamara and Tatjana, Anica for sharing the burden of the last year of the PhD, Jugoslava, Danica, Ana, Aleksandar, Nikola, Marko, Mihailo, Ivan, Bane, Dusko and Nikodin.

Finally, my gratitude and love go to my family: my Mom, my Dad, my Sister and my Brother for their love, support and understanding; to my aunts and uncles, and my late Grandfather for his example of a lifelong thirst for knowledge.

Abstract

———

Hall-effect devices make up by far the largest part of all magnetic sensors on the market today. The main reason is compatibility of Hall devices with modern semiconductor technology. In particular, integrated Hall sensor micro-systems fabricated in low-cost complementary metal oxide technology (CMOS) have dominated the market of magnetic sensors over the last decade.

Recently, a new Hall device – the circular vertical Hall device (CVHD) - joined the family of CMOS compatible Hall devices. The CVHD can be biased and Hall voltage retrieved from it such that its output is a sine wave signal. The amplitude of the sine wave signal contains the information on the magnitude of the magnetic field, while the phase of the sine wave signal carries the information on the direction of the magnetic field. This is why a CHVD can be thought of as the first Hall device measuring an in-plane magnetic induction vector. It is due to this feature that the CVHD was first used as a sensing device in magnetic angular sensors. These CVHDs had a large number of contacts leading to a high angular accuracy, but limiting bandwidth of the sensor.

This thesis was devoted to exploring and pushing the limits of CVHDs and integrated magnetic sensors based on CVHDs. The first aim of the thesis was to study the limits of bandwidth increase while keeping satisfying accuracy of angular sensors based on the CVHD.

In order to increase the angular sensor's bandwidth, we optimized the CVHD, the front end of the sensor comprising the device and interface electronics, and finally the system level topology.

The CVHD was ultimately miniaturized to the device containing only eight contacts (8CVHD). The smaller the number of contacts, the faster is obtained the sine wave signal from the CVHD. A novel symmetric Hall voltage retrieval facilitated by the geometry and including all contacts was used. It led to the residual offset voltage comparable with devices having a much larger number of contacts.

It was shown that the increase of the sensor's bandwidth is not only limited by the device but also by the interface electronics. This is particularly so because the sensor system relies on the spinning current method for offset reduction. In this case, the interface electronics includes spinning switches and a preamplifier. The spinning current method introduces voltage spikes that decrease accuracy when increasing bandwidth. The modeling of the horizontal Hall device and the interface electronics containing spinning switches and preamplifier was presented. The model was extended for the specific case of the sensors based on the 8CVHD.

Three solutions to tackling the challenge of increasing the spinning frequency, or equivalently sensor's bandwidth, while maintaining accuracy were proposed and discussed. The first one is a novel solution relying on the high input capacitance of the preamplifier which together with the sensing switch on-resistance filters out the voltage spikes. The second solution examines the partial guard band to remove a part of the spikes' energy without compromising the high spinning frequency.

The third solution is based on the cancellation of the voltage spikes by the time-shifted clockwise and counterclockwise spinning current method on two pairs of devices. These solutions were employed in three different sensors based on the 8CVHD.

On the system level, a novel concept of the angular sensor based on two 8CVHDs was used. The outputs of the 8CVHDs are separately processed in two channels and they act as mutual reference signals. The Hall voltage retrieval is done in the clockwise direction for the first device, and in the counter clockwise direction for the second one. In this way there is no need for the reference signal as in the known concept. The use of two devices doubles the sensitivity of the sensor.

Finally, the optimized device, the solutions for the design of interface electronics, and the system level topology were combined in two implementations in 0.35 μm CMOS technology. The first implementation employed one 8CVHD per channel. The average angular error was found to be ± 4 º with the sensor's bandwidth of about 300 kHz. The second implementation employed an array of 8CVHDs per channel. The average angular error was found to be ± 1.5 º with the sensor's bandwidth of about 500 kHz.

The second aim of the thesis was to investigate the feasibility of magnetic sensors based on the 8CVHD for some challenging applications. To this end a two-dimensional (2D) magnetometer and a magnetic sensor for use in open-loop current transducer were designed and experimentally characterized.

The novel system level concept for the 2D CMOS integrated magnetometer based on the 8CVHD was proposed. It enables common biasing, signal retrieval, dynamic cancellation of offset and low frequency noise, and front-end signal conditioning electronics for both components of the measured in-plane magnetic field vector. Separation of two channels is postponed to the point where signal levels are high and less susceptible to nonidealities and mismatches of signal conditioning electronics. The magnetometer features bandwidth around 60 kHz, wide dynamic range 0-1.5 T, high spatial resolution, and a high measurement resolution of 300 μT over frequency range 0-30 kHz.

The magnetic sensor for the open-loop current transducer is based on the high bandwidth angular sensor and a tangent converter circuit. The initial experimental verification showed the bandwidth around 100 kHz, along with a wide dynamic range and good linearity.

Keywords: circular vertical Hall device, spinning current method, voltage spikes, high bandwidth magnetic angular sensor, two-dimensional magnetometer, open-loop current transducer

Résumé

_____

Les dispositifs à effet Hall constituent la plus grande partie de tous les capteurs magnétiques sur le marché aujourd'hui. La raison principale est leur compatibilité avec la technologie des semi-conducteurs modernes. En particulier, les capteurs Hall à bas coût de fabrication, comme la technologie Complementary Metal Oxide Semiconductor (CMOS), ont dominé le marché des capteurs magnétiques au cours de la dernière décennie. Récemment, un nouveau dispositif à effet Hall - le dispositif de Hall circulaire vertical (CVHD) - a rejoint la famille des dispositifs Hall compatibles avec la technologie CMOS. Le CVHD peut être opéré de sorte que le signal de sortie est sinusoïdal. L'amplitude du signal sinusoïdal contient l'information sur l'intensité du champ magnétique, tandis que la phase du signal sinusoïdal porte l'information sur l'orientation du champ magnétique. C'est pourquoi un CHVD peut être considéré comme un dispositif mesurant le vecteur du champ magnétique. C'est la raison pour laquelle le CVHD a d'abord été utilisé dans les capteurs angulaires. Le CVHD utilisé dans les capteurs angulaires avait grand nombre de contacts menant à une haute précision angulaire, mais limitant la bande passante du capteur.

Cette thèse a été consacrée à l'exploration des limites du CVHD et des capteurs magnétique intégrés basés sur le CVHD.

Le premier objectif de la thèse était d'étudier les limites de l'augmentation de la bande passante des capteurs angulaires basés sur le CVHD tout en gardant une précision satisfaisante. Afin d'augmenter la bande passante du capteur intégré nous avons optimisé le CVHD, le front-end du capteur comprenant le CVHD et l'électronique d'interface, et enfin la topologie au niveau du système.

Au cours ce cette recherche, le CVHD a été miniaturisé de manière extrême, ce qui a donné un CVHD à seulement huit contacts (8CVHD). Le signal sinusoïdal du CVHD est obtenu plus rapidement lorsque le nombre de contacts est plus petit. Une nouvelle façon de la polarisation du capteur ainsi que l'acquisition de la tension Hall ont été utilisée. Celles-ci sont symétrique grace à la géométrie du 8CVHD qui permet d'utiliser tous les contacts à la fois. La nouvelle acquisition de la tension Hall a conduit à une tension d'offset résiduelle comparable avec les dispositifs à plus grand nombre de contacts.

Il a été montré que l'augmentation de la bande passante du capteur n'est pas seulement limitée par le dispositif à effet Hall, mais également par l'électronique d'interface. C'est particulièrement vrai lorsque le capteur à effet Hall repose sur le procédé nommé « spinning current », nécessaire pour réduire la tension d'offset. Dans ce cas-là, l'électronique d'interface comprend des interrupteurs et un préamplificateur. Le spinning current introduit des pics de tension qui diminuent la précision quand on augmente la bande passante. Le modèle de dispositif à effet Hall horizontal avec une électronique d'interface contenant des interrupteurs et le préamplificateur a été présenté de points de vue de pics de tension. Le modèle a été étendu pour le cas spécifique du capteur 8CVHD. Trois solutions pour

v

relever le défi d'augmenter la fréquence de « spinning current », ou de façon équivalente la bande passante du capteur, tout en maintenant la précision ont été proposées et discutées. La première est une nouvelle solution s'appuyant sur la capacité d'entrée du préamplificateur qui avec la résistance de l'interrupteur filtre les pics de tension. La deuxième solution porte sur « guard-band » partiel pour enlever une partie de l'énergie des pics de tension sans pour autant compromettre la fréquence élevée de « spinning current ». La troisième solution est basée sur l'annulation des pics de tension par le « spinning current » décalés et dans les deux sens, le sens horaire et le sens antihoraire, sur les deux paires de dispositifs. Ces solutions ont été employées dans trois capteurs Hall différents basés sur le 8CVHD.

Au niveau du système un nouveau concept du capteur angulaire reposant sur deux 8CVHDs a été utilisé. Les sorties des 8CVHDs sont traitées séparément dans deux canaux et agissent comme un signal de référence l'une à l'autre. L'acquisition de tension Hall est faite dans le sens horaire pour le premier dispositif, et dans le sens antihoraire pour le second. De cette façon, le signal de référence n'est pas nécessaire. L'utilisation de deux dispositifs double la sensibilité du capteur.

Enfin, une fois le dispositif optimisé, les solutions pour la conception de l'électronique d'interface, et la topologie au niveau du système ont été combinés dans deux implémentations dans la technologie CMOS 0.35 µm. Dans la première implémentation on utilise un 8CVHD par canal. L'erreur moyenne angulaire mesurée a été ± 4 º pour le capteur à une bande passante d'environ 300 kHz. La deuxième implémentation utilise un array de 8CVHDs par canal. L'erreur moyenne angulaire mesurée a été ± 1.5 º pour le capteur à une bande passante d'environ 500 kHz.

Le deuxième objectif de la thèse était d'étudier la faisabilité de capteurs magnétique intégrés basés sur le 8CVHD pour certaines applications difficiles. A cette fin, un magnétomètre à deux dimensions (2D) et un capteur magnétique pour une utilisation dans un transducteur de courant en boucle ouverte ont été conçus et caractérisés expérimentalement.

Un nouveau concept pour un magnétomètre 2D CMOS basé sur le 8CVHD a été proposé. Les deux composantes du champ magnétique ont en commun : la polarisation, l'acquisition du signal, l'annulation dynamique du bruit de basse fréquence et tension de l'offset, et le front-end condition-nement du signal. La séparation des deux canaux est reportée au point où les niveaux de signal sont élevés et moins sensibles aux variations de l'électronique de conditionnement. Les caractéristiques obtenues sont: une bande passante autour de 60 kHz, une large gamme dynamique de 0 à 1.5 T, une haute résolution spatiale, et une grande résolution de mesure de 300 µT pour 0-30 kHz.

Le transducteur de courant en boucle ouverte est fondé sur un capteur angulaire à haute bande passante et un circuit de conversion qui calcule la fonction « tangente ». Une vérification expéri-mentale a montré une bande passante d'environ 100 kHz, avec une large gamme dynamique et une bonne linéarité.

Mots-clés: dispositif Hall circulaire vertical, le « spinning current » procédé, les pics de tension, capteur angulaire magnétique à haute bande passante, magnétomètre à deux dimensions, transducteur de courant en boucle ouverte

Contents

List of Figures

xvi

Chapter 1

Introduction

Magnetic sensors represent one of the most pervasive types of sensors sold today [1]. They are used in high-cost applications like industrial motors that require accurate knowledge of rotor position to control loads. They are ever present in automotive industry, Fig. 1.1, where they serve many purposes: measuring of rotation speed, angle, position, to name but a few. They are extensively used for contactless current measurements. They can be also found in low-cost home appliances. A completely new product in the family of magnetic sensors - the electronic compass, was a market hit in 2009 due to its use in general positioning system (GPS)-equipped handsets. Hall devices and Hall effect sensor integrated circuits make up by far the largest part of magnetic sensors on the market today.

In this chapter will be given a short overview of the past and remaining challenges in the design of Hall effect magnetic sensors. It will be followed by the motivation and objectives of the thesis. The overview of the thesis will be given at the end of the chapter.

1.1   CMOS Hall effect magnetic sensors

The Hall effect was discovered by E. W. Hall in 1879 [6]. It is a galvanomagnetic effect occurring in a piece of conductor or semiconductor biased by electrical current and exposed to magnetic field. The Lorentz force deflects the trajectory of carriers and gives rise to an electromotive force. The electromotive force is perpendicular to both electric and magnetic fields. It generates an electrical voltage proportional to biasing current and magnetic field.

The compatibility of Hall devices with modern semiconductor technology has led to the widespread use of Hall effect magnetic sensors. The fabrication of Hall devices, both horizontal and vertical ones, does not require any modification of a standard technology process flow. Hall devices fabricated in low-cost complementary metal oxide technology (CMOS) have dominated the market in the last decade. Their characteristic performances are inferior to those of discrete Hall devices made of high mobility compound semiconductors, such as GaAs or InSb [7]. A Hall device as a stand alone device in CMOS technology suffers from: a voltage without applied magnetic field referred to as the offset
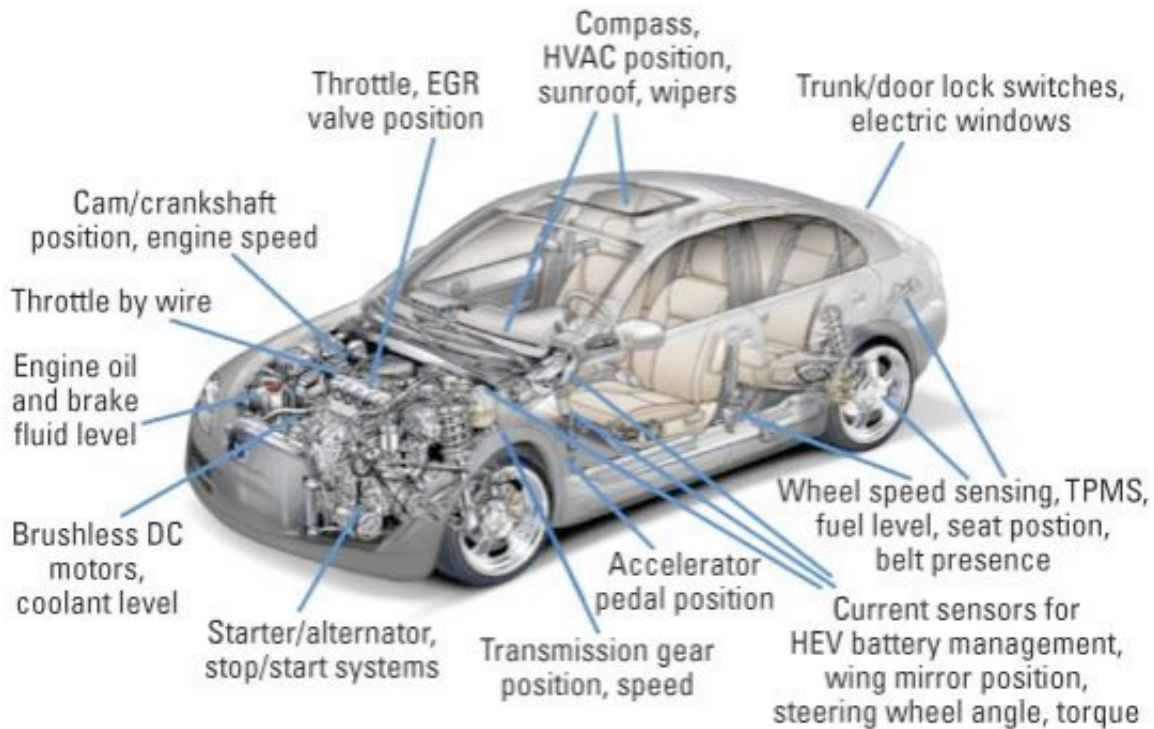
Figure 1.1: Magnetic sensors in a car (source [1])

voltage, a small value of the Hall voltage, noise in the Hall voltage that may bury the useful signal, temperature and stress cross sensitivity [3], etc.

The drawbacks of CMOS Hall devices are compensated by the possibility to cointegrate signal conditioning electronics. The cointegration of electronics enables system level approach to designing Hall effect magnetic sensors. The system level approach offers a more efficient implementation of various techniques dedicated to enhancing both characteristics of Hall devices and Hall effect sensors. Hall effect sensors in CMOS technology usually comprise biasing circuits, interface electronics between a device and the first signal conditioning stage, signal conditioning electronics, electronics dedicated to offset voltage and noise voltage reductions, to temperature stabilization and non-linearity correction, etc. Signal conditioning electronics contribute to the overall performance of the Hall effect magnetic sensor by its own unavoidable non-idealities.

One of the main limitations of Hall effect magnetic sensors in CMOS technology is their modest magnetic resolution. Magnetic resolution of a sensor is the smallest change in the magnetic field that can be detected in the output signal. We distinguish between the resolution of an AC magnetic signal and that of a quasi- DC magnetic signal.

The resolution of an AC magnetic signal is limited by the noise of the sensor and depends on the frequency band of interest. The AC resolution is usually expressed as the noise-equivalent magnetic field spectral density of a transducer. The noise of the Hall effect sensor is dominated by the noise

2

of the Hall device and the input-referred noise of signal conditioning electronics. The noise voltage at the output of a Hall device is superposition of several noise components, including thermal noise, 1/f noise, and sometimes shot noise and generation-recombination noise due to a leakage current. At sufficiently high frequencies above the 1/f corner frequency (which is usually between 100 Hz and 100 kHz), i.e., in the thermal noise region, the noise equivalent magnetic field spectral density of an integrated silicon Hall device is about 50 nT/√Hz at room temperature. The input-referred noise voltage of a Hall magnetic sensor is the quadratic sum of the noise voltage at the output of a Hall device and the input-referred noise voltage of signal conditioning electronics. The input referred noise of the first amplifier dominates in the input referred noise of signal conditioning electronics. In modern discrete realizations of Hall effect sensors, the noise voltage of the preamplifier is usually negligible. In contrast, in integrated Hall sensors the noise contributions of a Hall device and that of the preamplifier are of the same order of magnitude .

The resolution of a quasi-DC magnetic signal depends on the measurement environment. In laboratory measurements the offset voltage of a sensor can be zeroed just before taking a measurement. The resolution is then expressed as the integrated noise over a frequency bandwidth, usually between 0.1 Hz and 10 Hz. However, in industrial applications the offset voltage of a sensor is usually zeroed once. Thus, the resolution is limited by the offset voltage drift in time and with temperature.

The offset of a Hall device is caused by geometrical lithographic errors and etching randomness, process gradients in physical characteristics of a Hall device, the junction-field effect, the self-magnetic field, piezo-resistance effect caused by mechanical and/or thermal stress, and various thermal and thermoelectric effects. The typical offset equivalent magnetic field of a Hall device realized in the silicon integrated technology is 5-50 mT. A good portion of the offset voltage of a Hall device is deterministic and behaves as a voltage at the output of a Wheatstone bridge: it is proportional to the voltage applied at the input terminals of a Hall device. But, there are always non-deterministic changes in the offset voltage: the fluctuations caused by 1/f and other low-frequency noise, the fluctuations related to packaging stress, aging, and other unknown causes. This unpredictable change of offset is referred to as the offset drift. As explained above, the offset drift may severely limit the quasi-DC resolution of Hall magnetic transducers in most industrial applications.

The offset of a Hall effect magnetic sensor is the sum of the uncanceled offsets of a Hall device and the signal conditioning electronics. In discrete Hall effect sensors the preamplifier's offset is usually negligible, unlike that in integrated Hall effect sensors.

There are several techniques for offset voltage reduction of a Hall device in a Hall effect sensor. These techniques reduce to some extent offset drift as well. One of them is orthogonal coupling of Hall devices. It is based on pairing of an even number of Hall devices and biasing them orthogonally [8]. A Hall device is non-reciprocal for the Hall voltage and reciprocal for the offset voltage. As a result, the outputs of the devices can be connected such that the respective Hall voltages are

averaged while offset voltages are cancelled out. This method is also referred to as the averaging of the Hall voltage in space.

Another method of offset voltage reduction is spinning-current method [9], also known as the connection-commutation, switched Hall plate or dynamic method. Unlike the orthogonal coupling, this method requires only one symmetric Hall device. The direction of the biasing current is made to spin along the symmetry axes of a Hall device. The Hall voltage is taken from the pair of contacts with transverse position with respect to the direction of the biasing current. In other words, biasing and sensing contacts are made to spin. The Hall voltage is invariant with respect to the symmetry axes to the first approximation. However, the offset voltage changes its sign but remains almost constant in magnitude. The technique is also referred to as the averaging over time, since the signal at the output is available after one spinning period. The orthogonal coupling and spinning-current method can be combined in an array of Hall devices, as demonstrated in [10]. The remaining offset after offset reduction techniques is referred to as residual offset.

The traditional spinning current modulation-demodulation system level topology of a Hall effect magnetic sensor [3] is given in Fig. 1.2. The spinning current method for offset reduction requires switches for commutation of biasing and sensing contacts. Each time the biasing and sensing switches are commutated, the time is needed for the voltage on the sensing contacts to settle down from biasing voltages to the common-mode voltage plus the Hall voltage [11]. This creates the voltage spikes, also referred to as the switching noise [12]. The settling time of the spikes represents a negligible part of the spinning period for low spinning frequencies. In contrast, with the increase of the spinning frequency, the settling time of the spikes stretches over the spinning period. In this way, the settling time poses the limit to the maximum spinning frequency. This in turn means the limitation to the maximum bandwidth of the Hall sensor.

The spinning current method is the most effective means for offset reduction of Hall devices. Since it is a variation of the chopped amplifier technique [13], it also reduces the 1/f noise of a Hall device. As such, it is extremely useful and always used in modern CMOS Hall sensors. It is indispensable to the increase of magnetic resolution for low bandwidth Hall sensors. However, for high bandwidth Hall sensors requiring high spinning frequencies, its efficiency decreases due to voltage spikes. Namely, the voltage spikes can not be filtered out in the traditional topology shown in Fig. 1.2. Their contribution to the useful Hall voltage behaves like a residual offset voltage. It increases with the increase of the spinning frequency and is temperature dependent.

The influence of the voltage spikes on accuracy can be avoided by using an alternative system topology to that shown in Fig. 1.2. The demodulation by switches can be replaced by synchronous demodulators with delayed signal sampling to avoid spikes. This was done in high sensitivity magnetometer [14], in [15] where correlated double sampling was used, as well as in [16], to name but a
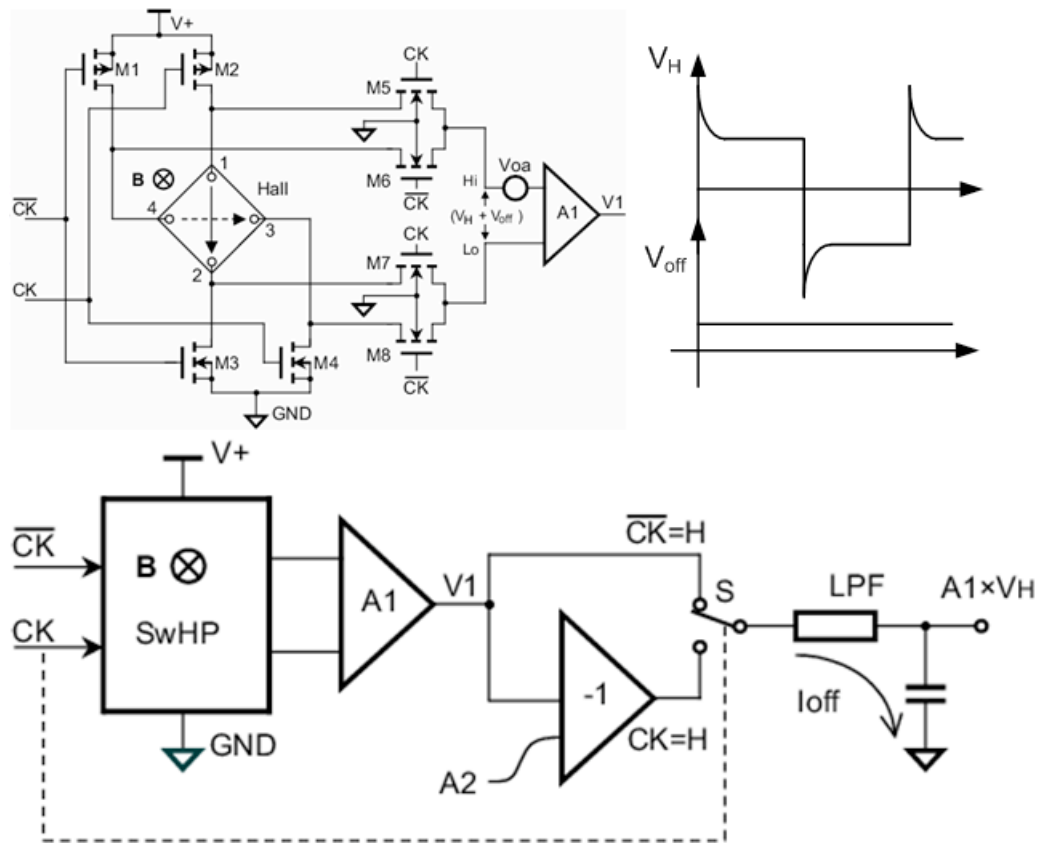
Figure 1.2: Traditional spinning current modulation (top) - demodulation (bottom) topology of a Hall effect magnetic sensor
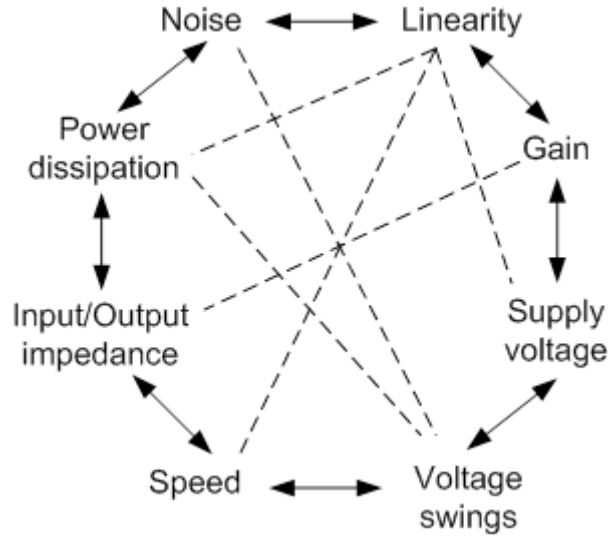
Figure 1.3: Analog design octagon (reprinted from [2])

few. The design specifications for this type of demodulators are highly demanding at high spinning-frequencies. In addition, the overall noise in sampled systems increases with the increase of the sampling frequency.

The traditional topology shown above suffers from the same non-idealities as a chopped amplifier [17]. The DC value of the demodulated signal is decreased due to the finite bandwidth of the amplifier. There is an additional requirement in order to maintain a maximum DC gain. The phase shift between the spinning current modulator and demodulator has to match precisely the phase shift introduced by the amplifier. One way to simplify the system would be to design the amplifier such that its bandwidth is at least one decade greater than the spinning frequency. In this case the phase shift introduced by the amplifier is negligible [18]. However, the integrated noise of a high bandwidth amplifier can severely reduce the overall sensor's resolution.

In conclusion, there is a trade off between the sensor's bandwidth and its resolution and accuracy. In general, the design of a Hall effect magnetic sensor is a multi-parameter optimization of both Hall device and signal conditioning electronics. The analog design octagon, Fig. 1.3, [2] depicting the trade-offs in the analog design can be used to describe the design of Hall effect sensors (e.g. , input/output impedance can be applied to input/output resistance of a Hall device). There is always a trade off between the sensor's power consumption, bandwidth, linearity, residual offset, noise and magnetic resolution.

1.1.1 State-of-the-art in CMOS Hall effect magnetic sensors

Over the last decade there were four major achievements in the development of Hall effect magnetic sensors in CMOS technology: increase of magnetic resolution, development of monolithic three

dimensional (3D) Hall effect sensors, increase of sensors' bandwidth, and stabilization of sensors' sensitivity and offset drift.

The first achievement was increase of magnetic resolution and sensitivity with the aim to enter low field measurements and eventually the booming electronic compass market. The Hall effect magnetic sensor based on the spinning Hall device with nested-chopper technique achieved 5 µT offset equivalent magnetic field at the expense of low bandwidth of the sensor [19]. In [20] four eight-contact Hall devices were orthogonally coupled. The eightfold spinning current method was applied simultaneously with the orthogonal coupling to reach 2 µT offset equivalent magnetic field. Neither additional trimming nor calibration was employed to reduce the offset voltage. The Hall effect magnetic sensor presented in [21] has 5.2 µT noise equivalent magnetic field over 1 kHz bandwidth. The special emphasis was put on driving up the sensitivity of the used gated horizontal Hall device, and driving down the input referred noise of the signal conditioning electronics. The system architecture of the above mentioned sensors was based on the traditional topology, Fig. 1.2. The noise equivalent magnetic field of 2 µT over 400 Hz bandwidth was reported in the Hall effect magnetic sensor dedicated to position, angle and current sensing [22] .

The second achievement was measurement extension from one axis to three axes, with high measurement resolution on all three axes and low power consumption. The monolithic CMOS integrated 3D magnetometer was presented in [23]for the first time. The sensor's front end consists of one horizontal Hall device for measurement of the perpendicular component of a magnetic field, and two pairs of vertical Hall devices dedicated to measurement of the in-plane components of a magnetic field. The sensor's bandwith is 30 kHz. In [24] a similar configuration for the front end was employed. The bandwidth of the magnetometer is 1.6 kHz with the resolution of 20 µT for the perpendicular component, and at best 100 µT for the in-plane components of the magnetic field.

The best results were achieved in 3D sensors with an integrated magnetic concentrator (IMCs) [25]. These sensors combine a horizontal Hall device with an integrated ferromagnetic disc on top of it. The ferromagnetic material changes the direction of the magnetic field from the in-plane to perpendicular. The ferromagnetic material requires one post-CMOS processing step. The technology offers voltage- and current-related sensitivities for the in-plane components of the magnetic field comparable with those for the perpendicular component of the field. Owing to this, the most widespread compass in the smart phones today is based on the horizontal Hall devices with IMCs [26]. The concept achieved magnetic resolution of 0.3 µT in commercially available compasses [27].

The third achievement was automatic calibration of the sensor's sensitivity and offset voltage dominantly for current transducers and magnetometers applications. The sensitivity and offset voltage of a Hall device and Hall effect sensor change with temperature. There are two distinct concepts to stabilize sensitivity and offset drift. The first concept relies on digital calibration in dominantly digital Hall effect sensor, as for instance in [22]. The system includes temperature sensors

and EEPROM memory for digital calibration of sensitivity and offset drift. The second concept is an all analog solution based on an integrated coil whose function is to create reference field [28]. The Hall device used in this sensor is a horizontal one. The reference field is temperature insensitive to the first approximation. The Hall voltage output proportional to the reference field drifts along with the drift of sensitivity. The difference between the Hall voltage and a preset reference voltage serves to change the biasing current of a Hall device. In this way, the output voltage of the Hall device is kept constant with temperature. Many solutions based on the proposed concept were reported [29, 30, 15]. They deal differently with the problem of distinguishing between the measured and reference fields. However, they have in common the tacit supposition that the reference field is temperature independent. This is difficult to achieve due to voltage-to-current conversion which always requires a resistor. The resistance of this resistor drifts with temperature.

The fourth achievement was increase of sensors' bandwidth mainly in magnetometers applications. In 3D CMOS Hall effect magnetometers, the highest bandwidth with satisfying resolution was reported in [23]. The resolution of 100 µT for all three axes over 30 kHz was reported. The highest bandwidth of CMOS Hall effect magnetometers for use in current transducers was reported in [16]. Theoretically, the system allows measurement of an AC magnetic field or current of up to 500 kHz (after removal of the low pass filter). To our knowledge, in Hall effect sensors based on the traditional topology and available on market the highest reported cut-off frequency is about 100 kHz. This is more than sufficient for all position sensing and low-frequency current measurement. However, modern electrical switched power systems would require low-cost sensors for current measurement having the bandwidth from DC to about 1 MHz.

The last decade also saw a new concept in magnetic angular sensors facilitated by a new device - a circular vertical Hall device (CVHD). It was first presented in [5], [31]. The CVHD can be biased and its signal sensed such that the signal at the output is a sine wave whose frequency is proportional to the clock frequency and the number of contacts. Its amplitude is proportional to the magnitude of the in-plane magnetic field. The phase of the sine wave is proportional to the angle included between the vector of the magnetic field and a reference axis. In this way there is no need for additional arctg function as in the majority of the angular sensors. This is why the CVHD was first used in magnetic angular sensors. The device in [5], [31] has a large number of contacts to efficiently suppress offset and noise. This in turn leads to low bandwidth of angular sensors, but sufficient for majority of applications today.

1.2 Thesis Motivation and Objectives

The field of Hall devices and sensors has been extensively studied in the last decades. It might be argued that from the scientific point of view it is in the saturation region of the learning curve. Nevertheless, the theoretical limits of Hall devices, e.g., resolution and maximum operation frequency,

have not yet been attained. From the industrial point of view, the Hall sensors available on market today meet the needs of existing applications. However, there is still room to find new applications for existing Hall sensors. This was the case with the electronic compass in smart phones. On the other hand, there is still room for new Hall devices to change the concepts and push the limits of Hall sensors in existing applications. This was the case with the CVHD in magnetic angular position sensors.

In this view, the motivation for this thesis work is to explore the features and limits of the CVHD. The exploration of limits can focus on minimum/maximum number of contacts, maximum operation frequency, best achievable resolution, etc. The unique features of the CVHD are appealing since they may offer new concepts for some standard Hall sensors architectures.

The objective of the thesis is to increase bandwidth with satisfying accuracy of the sensors based on the CVHD. To this end we study three levels of abstraction of a Hall sensor based on the CVHD:

1) the device level,

2) the front end level comprising the device and interface electronics,

3) system level topology with optimization of analog building blocks.

On the device level, we want to study and optimize the ultimately miniaturized version of a CVHD - an eight contact circular vertical Hall device (8CVHD). The device miniaturization and reduction of the number of contacts was motivated by desire to increase the system's bandwidth and spatial resolution. The smaller the number of contacts of a CVHD, the faster is obtained the signal containing the information on the magnetic field. However, there is a trade-off between the number of contacts and the residual offset of the device [5]. We investigate the alternative Hall voltage retrieval from the 8CVHD in order to circumvent this disadvantage.

On the front end level, we study the interface between the device and the first amplifier. The spinning current method as an efficient means for offset reduction has to be kept in the system topology. Since we want to increase the sensor's bandwidth, the optimal design of the interface electronics including spinning switches and the first amplifier should be investigated.

On the system level, we want to investigate novel topologies facilitated by the features of the CVHD. The CVHD can be thought of as the first Hall device that measures vector of the magnetic field: the information on the magnitude and direction is obtained simultaneously. The information on the magnitude of the magnetic field is contained in the amplitude, while the information on the direction of the magnetic field is contained in the phase of the sine wave. This enables alternative signal conditioning. It allows us to modulate the Hall voltage without the need for demodulation. Instead of processing the amplitude of the signal, we process the phase of the sine wave. The processing of the phase opens up possibility for novel system level architectures. The output of a CVHD is an AC signal even for a DC field. This feature removes the need for the traditional spinning current method modulation-demodulation architecture. The offset voltage and noise of the

preamplifier can be highpass filtered. Besides, we will show that the voltage spikes due to spinning current method can be frequency separated from the useful Hall voltage. As a result of this frequency separation, the voltage spikes can be efficiently filtered out. This is not the case in the traditional modulation-demodulation topology.

A further objective of the thesis is to implement the findings mentioned above and test feasibility of using the CVHD in other types of magnetic sensors:

- low-noise high bandwidth two dimensional magnetometer,

- high bandwidth 0-90$^{\text{o}}$ magnetic angle sensor based on two 8CVHDs;

- proof of concept of a novel architecture for current transducer based on the magnetic angle sensor described above and the tangent converter.

1.3   Thesis Overview

In Chapter 2 is given a short overview of the Hall effect and characteristics of the vertical Hall devices in CMOS technologies. It is followed by the state of the art in circular vertical Hall devices (CVHDs). The miniaturized circular vertical Hall device containing eight contacts is then introduced. Its characteristics and performances are then discussed. A novel symmetric biasing of the device including all contacts is presented at the end of the chapter.

In Chapter 3 we study limitations of bandwidth increase while keeping satisfying accuracy in Hall sensors employing spinning current method for offset reduction. It will be shown that in CMOS integrated Hall sensors both the design of a Hall device and the interface electronics determine the contribution of voltage spikes to the overall sensor's accuracy. The model of the ideal Hall device and the interface electronics containing spinning switches and preamplifier is presented. The nonidealities of the device and electronics are then added to the ideal model and discussed. Finally, three solutions to tackling the challenge of increasing the spinning frequency (and consequently sensor's bandwidth) while maintaining accuracy in the sensors based on the 8CVHD are presented.

In Chapter 4 we test the characteristics of the 8CVHD as a sensing device in a two-dimensional (2D) CMOS magnetometer. The novel system level concept allows for the common biasing, Hall voltage retrieval, offset cancellation, and front end signal conditioning electronics for the two in-plane components of magnetic field. This leads to good matching of the output signals proportional to two components of the magnetic field. The explanation of the novel concept is followed by the measured characteristics of the CMOS implementation.

In Chapter 5 we investigate the limits of bandwidth increase with satisfying accuracy in the angular sensor based on the pair of 8CVHDs. The novel concept of the sensor is based on two eight contact circular vertical Hall devices (8CVHD). The smaller number of contacts allows for faster Hall voltage sensing from the device. The outputs of the 8CVHDs are separately processed in two channels and act as a reference signal one to another. The Hall voltage retrieval is done in the

clockwise direction for the first device, and in the counterclockwise direction for the second one. In this way, there is no need for the reference signal as in [31, 32]. The output of the sensor is a pulse width modulated (PWM) signal whose width is proportional to twice the angle enclosed between the in-plane magnetic induction vector and the reference axis. The information on the angle is directly present in the pulse width modulated signal. The use of two devices doubles the sensitivity of the sensor.

In Chapter 6 we investigate feasibility to design a high-bandwidth CMOS integrated magnetic sensor based on the 8CVHD for use in open-loop current transducers. State-of-the-art open-loop current transducers dominantly contain magnetic sensors based on horizontal Hall devices. We use a new design of the current transducer where a magnetic sensor is placed directly on the current carrying conductor. This is why a vertical Hall device is needed as a sensing device. In addition, open-loop current transducers require magnetic sensors with low temperature cross-sensitivity. Different calibration and auto-calibration techniques are implemented to reduce sensitivity and offset drift of the magnetic sensors with horizontal Hall devices. We examine a novel system level topology and its efficiency to reducing sensitivity drift with temperature of the magnetic sensor. Lastly, we want to use the features of the 8CVHD as well as the system level concept to extend the bandwidth and dynamic range of the open-loop current transducer.

In Chapter 7 are given conclusions as well as the outlook for the future work.

Chapter 2

Miniaturized Circular Vertical Hall Device

The chapter begins with a short overview of the Hall effect. It is followed by an overview of the characteristics of the vertical Hall devices in CMOS technologies. The state-of-the art in circular vertical Hall devices (CVHDs) is given next. An ultimately miniaturized circular vertical Hall device containing eight contacts - the 8CVHD is then introduced. The characteristics and performances of the device are then discussed. A novel biasing of the 8CVHD facilitated by its geometry is then presented. Its comparison with the standard biasing, as well as its efficiency are discussed at the end of the chapter.

2.1   Hall effect

The Hall effect, discovered by Edwin E. Hall [6], describes behavior of electrical current exposed to magnetic and electric fields.

When an electron is subjected to a magnetic field $\mathbf{B}$ and an electric field $\mathbf{E}$, the Lorentz force $\mathbf{F}$ acts upon it:

$$\boldsymbol{F} = -q\boldsymbol{E} - q(\boldsymbol{v} \times \boldsymbol{B}), \tag{2.1}$$

where q is the elementary charge and v is the electron velocity.

The current density $\mathbf{J}$ in an extrinsic semiconductor exposed to electric and magnetic fields, assuming there are no space charges, is given by:

$$\boldsymbol{J} = \sigma\boldsymbol{E} + \mu_H(\boldsymbol{J} \times \boldsymbol{B}), \tag{2.2}$$

where σ is conductivity and μ_H is the carrier Hall mobility. The Hall mobility, μ_H, is related to the carrier drift mobility, μ, by the Hall factor, r_H:

$$\mu_H = r_H \mu. \tag{2.3}$$

The Hall factor depends on the scattering effects in a semiconductor, as well as on the value of magnetic field for higher magnetic fields.

The vector equation 2.2 can be solved in terms of the current density vector:

$$\boldsymbol{J} = \frac{\sigma}{1 + (\mu_H B)^2} \left[\boldsymbol{E} + \mu_H (\boldsymbol{E} \times \boldsymbol{B}) + \mu_H^2 \boldsymbol{B} (\boldsymbol{E} \cdot \boldsymbol{B}) \right]. \tag{2.4}$$

In many practical applications of the Hall effect, the magnetic and electric fields are perpendicular. In this case, the equation above can be simplified to:

$$\boldsymbol{J} = \sigma_B \left[\boldsymbol{E} + \mu_H (\boldsymbol{E} \times \boldsymbol{B}) \right], \tag{2.5}$$

where

$$\sigma_B = \frac{\sigma}{1 + (\mu_H B)^2}, \tag{2.6}$$

is the effective carrier conductivity. The modification of the carrier's conductivity in a magnetic field is known as the magneto-resistance effect [33]. It becomes important in strong magnetic fields, since $\mu_H B << 1$ in weak magnetic fields.

Eqn 2.5 states that magnetic field causes deflection of the current density vector **J** with respect to the electric field vector **E**. This effect is known as the Hall effect. The deflection angle is referred to as the Hall angle, ϑ_H. It can be seen from Eqn 2.5 that the Hall angle is determined by the carrier mobility and the applied magnetic field:

$$\theta_H = arctg(\mu_H B). \tag{2.7}$$

The conventional discrete Hall plate is shown in Fig. 2.1. It is a conductive layer whose length, width and thickness are denoted by l, w and t, respectively. There are two pairs of contacts: biasing contacts, C1 and C2 , and sensing contacts, S1 and S2. The biasing contacts C1 and C2 are connected to the biasing voltage V which generates the electric field $\mathbf{E}_t$ and current I. The applied magnetic field is perpendicular to the layer's surface, $B_x = B_y = 0$ and $\mathbf{B} = B_z$. The magnetic field is considered homogeneous. The external electric field $\mathbf{E}_t$ gives rise to the current density J_x. The device is considered thin and long, $l/w >> 1$. Consequently, it is assumed that there is no current flow in the z-direction and no current deviation in the vicinity of the biasing contacts. The Lorentz force acts on the free carriers, deviating their path and causing their accumulation on one lateral side of the conductive layer. As a result of carriers accumulation, an electric field is generated - the Hall electric field $\mathbf{E}_H$. The equilibrium state is achieved when the Lorentz force acting on carriers
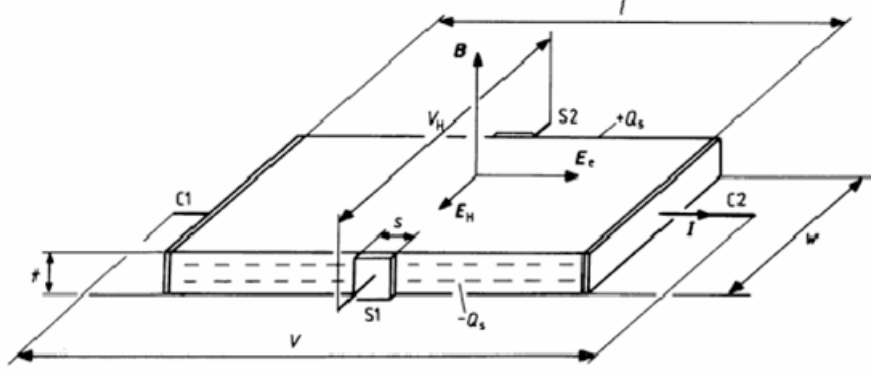
Figure 2.1: Discrete rectangular Hall device. When the current is passed between the contacts C1 and C2, the Hall voltage proportional to biasing current and applied magnetic field arises between the sensing contacts, S1 and S2.

is equal to the force exerted by the Hall field. In the equilibrium, there is no current flow in the y-direction, J_y=0. Eqn 2.4 now becomes:

$$J_x = \sigma_B \left[E_x + \mu_H (E_y B_z - E_z B_y) \right], \tag{2.8}$$

$$J_y = \sigma_B \left[E_y + \mu_H (-E_x B_z + E_z B_x) \right] = 0, \tag{2.9}$$

yielding the Hall field $\mathbf{E}_H = E_y$:

$$E_y = \mu_H B_z E_x, \tag{2.10}$$

$$J_x = \sigma_B (1 + (\mu_H B)^2) E_x = \sigma E_x. \tag{2.11}$$

The Hall voltage V_H can be found by integrating the Hall field between the sensing contacts:

$$V_H^\infty = \int\limits_{S1}^{S2} E_y dy = \int\limits_{S1}^{S2} \mu_H B_z E_x dy = \mu_H V B_z \frac{w}{l}, \tag{2.12}$$

where $E_x = \mathbf{E}_t = V/l$ is the external homogeneous electric field.

If the plate is biased by current I, the previous equation can be rewritten to be:

$$V_H^\infty = r_H \mu \frac{J_x}{\sigma} B_z w = \frac{r_H}{qnt} I B_z, \tag{2.13}$$

where the current density $J_x = I_B/wt$, and the conductivity $\sigma = qnt$, where n is the density of free carriers.

15

The previous relations were obtained under the assumption of a long plate $l/w >> 1$. However, this is not the case in practice. The geometrical correction factor was introduced to compare the Hall voltage of a long plate with that of a real plate:

$$\frac{V_H}{V_H^\infty} = G(\theta_H, \frac{l}{w}).$$ (2.14)

The geometrical correction factor depends on the Hall angle and the ratio l/w, and ranges from 0 for very short samples to 1 for long samples. For the small Hall angles, i.e., small magnetic fields, the geometrical correction factor G for a rectangular Hall plate with point sensing contacts is almost 1 for the ratio $l/w= 3$ [3].

Finally, the Hall voltages for the real Hall device in case of the voltage and current biasing are, respectively:

$$V_H = G\frac{w}{l}\mu_H V B_z = S_V V B_z,$$ (2.15)

$$V_H = G\frac{r_H}{qnt}I B_z = S_I I B_z,$$ (2.16)

where $S_V = G\mu_H w/l$ is the voltage-related sensitivity and $S_I = Gr_H/qnt$ is the current-related sensitivity. The voltage-related sensitivity S_V depends on the geometry and the Hall mobility, which is strongly temperature dependent. The current-related sensitivity S_I is inversely proportional to the carrier concentration n. It is fairly temperature stable for the plate doping density between 10^{15} and 10^{17} cm^{-3} [34] and in the operating temperature range of many applications nowadays.

2.2   Horizontal vs. vertical CMOS Hall devices

The horizontal Hall effect device, also referred to as the Hall plate, measures the component of the magnetic field perpendicular to the active region of the device. The horizontal device integrated in CMOS technology is shown in Fig. 2.2. The active region of the device is compatible with the layers readily available in CMOS technologies. The surface of integrated horizontal Hall devices is on the order of tens of μm^2. Their current-related sensitivities range from 150 V/AT to 400 V/AT. They can be easily cointegrated with signal conditioning electronics in many CMOS Hall effect sensors.

However, a horizontal Hall device, as any Hall device, suffers from offset voltage and low frequency noise. The spinning current method, as a means for offset and low frequency noise reduction, is highly efficient in symmetrical devices. The advantage of horizontal Hall devices is the fact that they possess the four-fold geometric symmetry. The four-fold geometric symmetry translates into galvanomagnetic symmetry. This in turn leads to the efficient application of the spinning current method. The CMOS Hall sensors based on horizontal Hall devices with spinning current method feature high resolution, e.g., the residual offset as low as 2 µT was reported in [20].
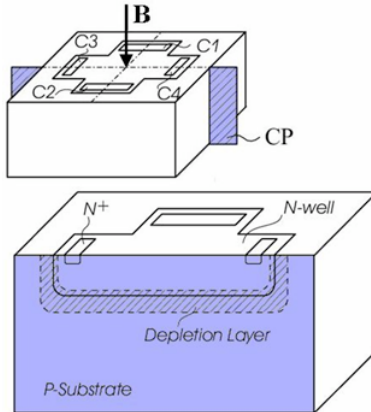
Figure 2.2: Horizontal Hall effect device in CMOS technology. The active layer is the N-well layer in a standard CMOS technology. The biasing and sensing contacts are realized as heavily doped N+ regions (adapted from [3]). The device has the four-fold geometric symmetry.

The vertical Hall device, a Hall effect device sensitive to the in-plane component of magnetic field, was first reported in [35].

In the beginning, vertical Hall devices were fabricated in the so-called vertical Hall technology (VHT) developed by Landis&Gyr. The technology is the N-substrate P-well technology with the open well. The vertical devices developed in this technology exhibited the current-related sensitivity of around 500 V/AT and overall excellent performance characteristics [36, 37]. Nevertheless, the devices manufactured in VHT were not compatible with standard CMOS technology.

The alternative to VHT was the trench-Hall technology only partially compatible with standard CMOS technologies. The trench-Hall technology yields highly sensitive vertical Hall devices, around 300 V/AT, at the expense of costly pre-processing [38]. Another possibility of increasing the sensitivity of vertical Hall devices is by using integrated magneto-concentrators (IMC) [25]. The idea is to combine a horizontal Hall device with an integrated ferromagnetic disc on top of it. The ferromagnetic material changes the direction of the magnetic field from the in-plane to perpendicular. The technology offers both high voltage- and current- related sensitivities, 0.09 V/VT and 360 V/AT, respectively. However, it requires post-processing and has limited measurement range due to the saturation field of the ferromagnetic disc.

The five contact (5C) vertical Hall device in CMOS technology is shown in Fig. 2.3.

In [4] the CMOS vertical Hall devices having characteristics comparable to horizontal CMOS Hall devices were first demonstrated. The limitations of the CMOS technology for fabrication of vertical Hall devices were pointed out and circumvented by novel layout of the device.

The modern CMOS technologies have diffusion layers featuring: 1) shallow junction, 2) higher doping levels to prevent latch-up, and 3) strong doping gradients with high surface concentrations. In [39] it was shown that conformal mapping can be applied to calculate expected sensitivity of vertical Hall devices whose active region is a well of the limited depth. The depth reduction from infinity
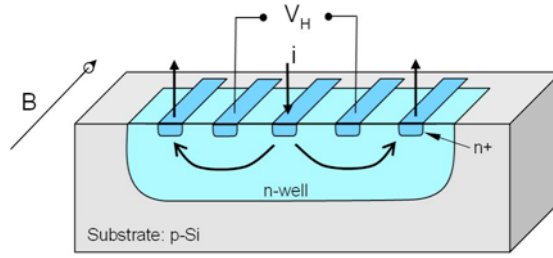
Figure 2.3: Five-contact vertical Hall effect device in CMOS technology. The limited depth of the N-well region reduces sensitivity of the device. The biasing and sensing contacts are heavily doped N+ regions and are located along one strip. The device has two-fold rotational symmetry.

(as is the case with VHT) to the range of lateral dimensions leads to voltage-related sensitivity reduction of at least 50%. This was circumvented in [4] by miniaturizing the device to the lower limits allowed by the design rules of the technology and even further. The miniaturization concerned the contact's width and their distance. The extreme miniaturization yielded high voltage-related sensitivity. This was achieved at the expense of high noise levels and stronger influence of mask-misalignments and doping gradients on the offset voltage. The limitation of high doping levels of the diffusion layers in CMOS technology was circumvented by using lateral diffusion layers of the opposite semiconductor's type. For instance, the lateral p-well (PTUB) can reduce surface doping concentration of the active region n-well (DNTUB). In this way, the current-related sensitivity can be increased. The compatibility of the CMOS vertical Hall devices with spinning current method for offset reduction was also studied for 4-contact (4C) [40], 5-contact (5C) [35] and 6-contact (6C) [4] vertical Hall devices.

Finally, it was shown in [4] that vertical Hall devices integrated in CMOS technology can achieve voltage-related sensitivity 0.04 V/VT and current-related sensitivity 200-400 V/AT. The CMOS process with deep diffusion layers was used (a high voltage technology) and the devices were ultimately miniaturized. By applying the four-phase spinning current method for offset reduction, the residual offset of the 6C device in 5V CMOS AMS 0.8 µm was about 200 µT [41].

The vertical Hall devices in the standard CMOS technology without deep N-well were reported in [42]. They feature low current-related sensitivity, but a good signal-to-noise ratio due to the alternative biasing and sensing of the Hall voltage. A detailed study on the intrinsic limitations of vertical Hall devices, as well as suggestion on Hall voltage sensing from the vertical Hall devices is presented in [43].

2.3 Five contact (5C) vertical Hall devices in 0.35 µm technology

The offset reduction by means of spinning current method is efficient in horizontal Hall devices due to their inherent geometric symmetry, i.e., the four-fold rotational symmetry. This leads to high electrical symmetry of spinning phases in the spinning current method. This geometric symmetry can not be reproduced in satisfying way in vertical Hall devices where the contacts are along one strip of semiconductor active region of limited depth.

It was shown in [4] that the main cause of the residual offset after spinning current method is nonlinearity caused by the interaction of the junction-field effect with fabrication imperfections, such as mask misalignments and doping gradients. The residual offset is a nonlinear function of the biasing current. Therefore reduction of the residual offset requires limiting of current density in the sensor active region. In other words, devices should be biased at low currents. But, the decrease of the biasing current leads to reduction of the Hall voltage. On one hand, the ratio of the Hall voltage and the residual offset is the best for low biasing currents. On the other hand, the ratio of the Hall voltage and the voltage noise is small for low biasing currents. The voltage noise of the Hall device consists of the 1/f noise, which scales down with the biasing current, and thermal noise, which is independent of the biasing current. The bottom line is the decrease of the signal-to-noise ratio at low biasing currents. This in turn limits the resolution of the device.

One way to design around this problem is to boost the Hall voltage level by geometrically increasing sensitivity of the Hall device. The current-related sensitivity of horizontal Hall devices can be increased by scaling up their lateral dimension (see Eqn 2.15 in Section 2.1). However, this can not be reproduced in vertical Hall devices. The increase of lateral dimensions leads to loss of sensitivity since the depth of the N-well is fixed by technology, as discussed above. One way to maintain signal-to-noise levels for vertical Hall devices biased at low currents is to use an array of devices.

There are three basic array topologies, as described by the circuit theory terminology: parallel input – parallel output, series input – series output, and parallel input – series output topologies. The solution based on parallel input – parallel output topology was reported [41] in 0.8 µm 5V technology. It contains a quadruple of orthogonally connected couples of four contact (4C) vertical Hall devices subjected to the four-phase spinning current method. Though offset reduction is efficient, it comes at a price of higher current consumption.

In series input – series output topology, besides using the same current, devices efficiently use voltage headroom that remains after proper biasing of electronics [44]. Nevertheless, the characteristics of a device depend on its position between supply lines due to the uneven influence of junction field effect. The stacked devices are supplied by the same current and share common substrate. Due
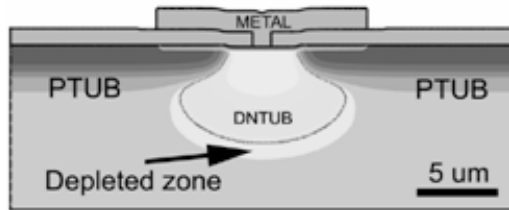
Figure 2.4: FEM simulation of the transversal cross section of a vertical Hall device in high voltage CMOS technology (adapted from [4])

to this, the potential difference between devices' contacts and the substrate increases for devices closer to the positive supply rail. This causes stronger influence of the junction field effect on the active region of these devices, which in turn leads to higher nonlinearities.

2.3.1 Influence of the junction field effect in series connected 5C vertical Hall devices

In order to examine the influence of the junction field effect, we tested several five contact (5C) devices with symmetric and asymmetric contacts. The devices were produced in three separate runs in CMOS AMS 0.35 µm high-voltage technology. A similar study was carried out on the horizontal Hall devices in [45].

The measurement results on the device with higher residual offset, i.e., higher inherent nonlinearities, are shown for illustrative purposes. The outer contacts of the 5C device are on-chip connected to emulate a 4C device. The FEM simulation of the transversal cross-section of the device in high voltage CMOS technology is given in Fig. 2.4.

The active region of the device is the deep n-well, DNTUB in this technology, having the junction depth of 5-6 µm. The deep p-well, DPTUB, serves to both enhance current-related sensitivity and act as a channel stopper. The doping concentrations of DPTUB and DNTUB are on the order of 10^{16} cm^{-3}, while the concentration of the p-substrate is on the order of 10^{14} cm^{-3}. The distribution of doping concentration in a semiconductor is the Gaussian function. It can be seen that there are two distinct pn-junction regions. The first one is highly doped DNTUB – DPTUB junction close to the contacts. It has a smaller surface since the depth of the DPTUB is 1.5-2 µm. The second one is lightly doped DNTUB – p-substrate with a larger surface, denoted in Fig. 2.4 as depleted zone. To illustrate the influence of junction field effect on characteristics of the device, a simple measurement setup, shown in Fig. 2.5a) and 2.5b) was used. The device was biased by a variable voltage source V_{bias} with a maximum value of 2 V. The higher position of the device in a stack, Fig. 2.5b), or equivalently, higher common-mode of a device's output voltage, was simulated by the battery supply $V_c = 1.4$ V. $V_{biascont}$ is the voltage drop on the device. The device was also biased
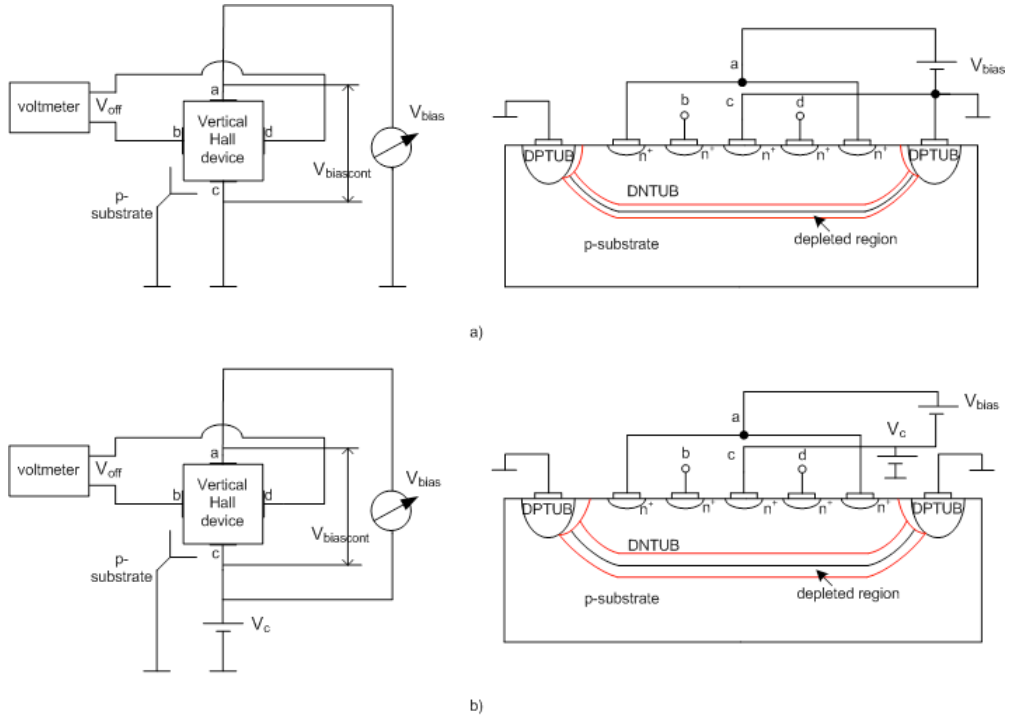
Figure 2.5: Measurement setup to examine influence of the junction field effect on series-connected vertical Hall devices: a) low common mode device, b) high common mode device

by a variable current source of maximum value 0.8 mA. The four-phase spinning current method for offset voltage reduction was performed manually.

The comparison of the voltage- and current-related sensitivities, S_V and S_I, for the low and high common mode devices is shown in Fig. 2.6. It can be seen that the current-related sensitivity, Fig. 2.6a), increases with higher common mode as a result of wider depletion regions and reduction of the effective width of the device, t_{eff}, since $S_I \sim 1/t_{eff}$. It is presumed that widening of DNTUB − DPTUB pn-junction has a more pronounced effect due to higher voltage across it. The relative change of S_I is 5% for the common mode difference of 1.4 V. As for the voltage-related sensitivity, Fig 2.6b), it can be seen that it decreases due to the increase of input resistance, Fig 2.7, since $S_V \sim 1/R_{in}$. The input resistance changes by 6%. It is not clear which pn-junction is dominant in changing the voltage-related sensitivity: DNTUB − DPTUB or DNTUB − p-substrate one.

The two-fold rotational symmetry can be clearly seen in Fig. 2.7: the input resistance and, consequently, the common mode of the device are not constant in all the phases of the four-phase spinning current method. This is due to the fact that the current density at contact a differs from the current densities at contacts b, c and d. In modern technologies, contacts are highly doped n+ regions, Fig. 2.5, and Hall devices are extremely miniaturized. In order to increase signal levels, we apply high currents or voltages over small distances. This is equivalent to high electric fields leading to velocity saturation of carriers at the contacts. In other words, the voltage drop at the contact is
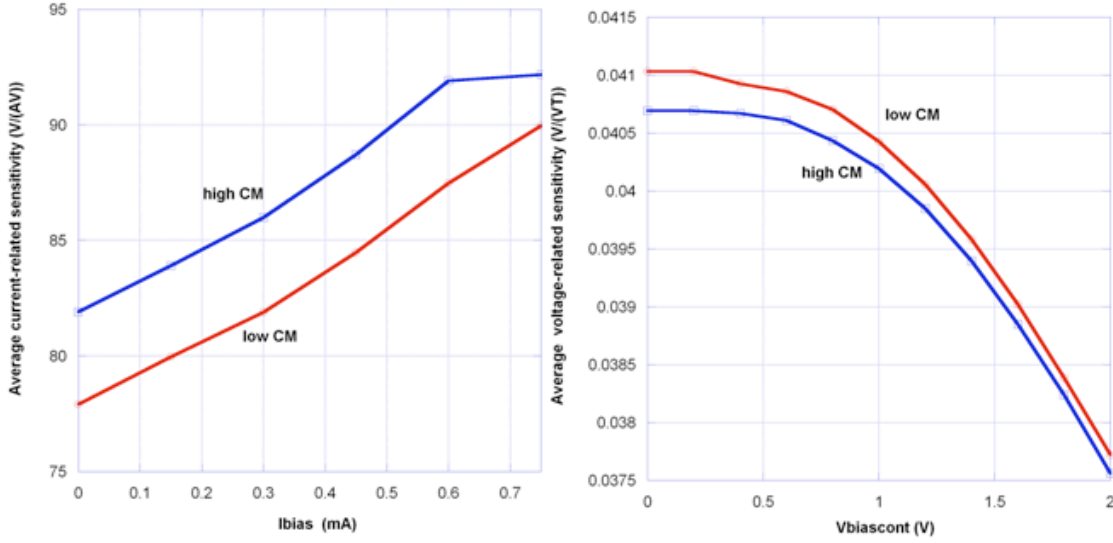
Figure 2.6: Comparison of sensitivities for low and high common modes: a) current-related sensitivity, b) voltage-related sensitivity

no more linearly related to the current through the contact. This is why different current densities cause different resistances at the contact a and contacts b, c, and d. This explains difference of the resistances R_{ac} and R_{bd} . The junction field-effect together with contact resistance causes the unequalitiy of resistances R_{ac} and R_{ca}. The residual offset is not zero even for the ohmic modelling of the offset voltage. This explains why the offset reduction in 5C vertical Hall device is not as efficient as in horizontal Hall devices.

Fig. 2.8 shows the offset voltage for current supplied device in the four phases of the spinning process, as well as the residual offset equivalent magnetic field. It can be seen that the average offset increase for the high common mode of the device is 20%. The offset voltage increase for higher common mode is evident from the ohmic modeling of the offset voltage. For the low common mode, the input resistance and resistance modeling mask misalignments are function of the applied voltage V_{biascont}, while for the high common mode they are function of $V_{\text{biascont}} + V_c$. Fig. 2.8 also shows that the increase of the residual offset due to the increase of the common mode by 1.4 V is lower than the increase of the residual offset due to voltage between the biasing contacts of 1.4 V (or equivalently biasing current $I_{\text{bias}} = 0.7$ mA). This means that the change of cross section of the active region of the device along the current flow affects the offset voltage stronger than the "uniform" reduction of active region due to higher reverse voltage between it and the substrate.

2.3.2 Biasing of series-connected 5C vertical Hall devices

The sketch of the series input – series output topology is given in Fig. 2.9. The pair of sensors can be orthogonally coupled (biasing of ac contacts for the high common mode device, and bd contacts for the low common mode device). The four-phase spinning can be performed by regulating the
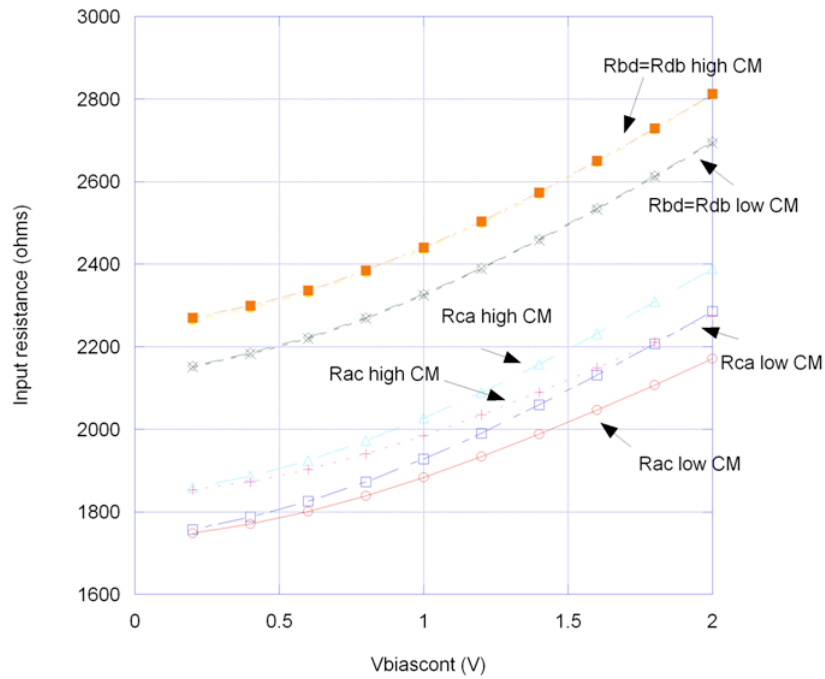
Figure 2.7: Comparison of input resistances for the low and high common modes of the device's output voltage
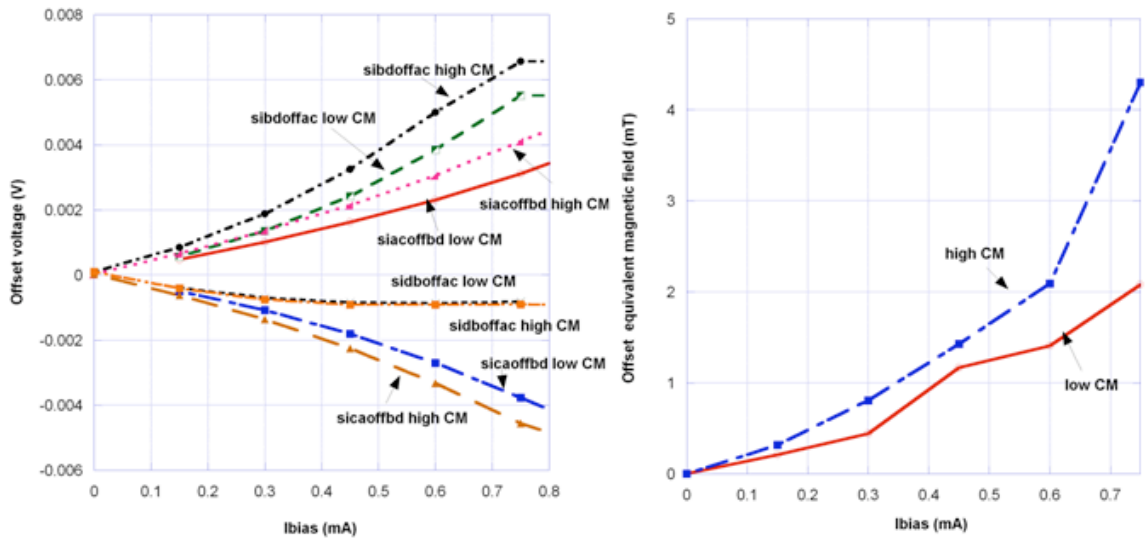
Figure 2.8: Offset voltages in four spinning phases (left), and offset equivalent magnetic fields after the four-phase spinning current method (right) for the low and high common modes
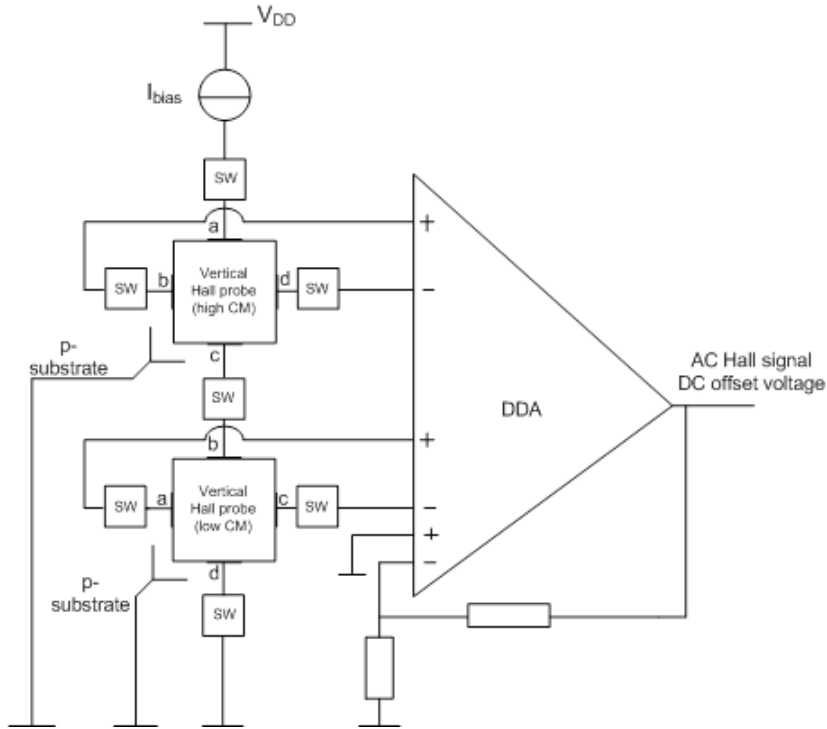
Figure 2.9: Series input – series output array of vertical Hall devices

switches, SW block. The same common mode in parallel input topology enables parallel output, or averaging of output signals by simple connection of sensing contacts. This can not be done in series topology, where the output signals must be summed at the level of electronics, for instance by using a differential difference amplifier [46]. In series input – series output topology, devices are not matched, due to different common modes of output voltage, as was shown above.

The residual offset voltage of the orthogonally coupled stacked Hall devices can be deduced by using a simple mathematical analysis disregarding influence of nonidealities of processing electronics. The residual offset voltage equals the sum of the residual offset voltages of each device. This sum is greater than n times residual offset of the device with the lowest common mode, where n represents number of devices in an array. Since the outputs of the devices are connected in series, the equivalent sensitivity is more than n times larger, due to slight increase of sensitivity caused by the junction-field effect, as shown above. Therefore, the residual offset equivalent magnetic field is slightly larger than the residual offset equivalent magnetic field of the device with the lowest common mode. The residual offset voltage and the residual offset equivalent magnetic field calculated for two series connected 5C vertical Hall devices are shown in Fig. 2.10.

Fig. 2.10 shows that the higher biasing currents lead to the higher absolute difference between residual offsets of the devices. In this view, the optimum biasing of a series input-series output topology is by a small current. Though the Hall voltage may be low, it is more efficient in terms of Hall signal vs. residual offset to have an array of n series connected Hall devices biased at a low
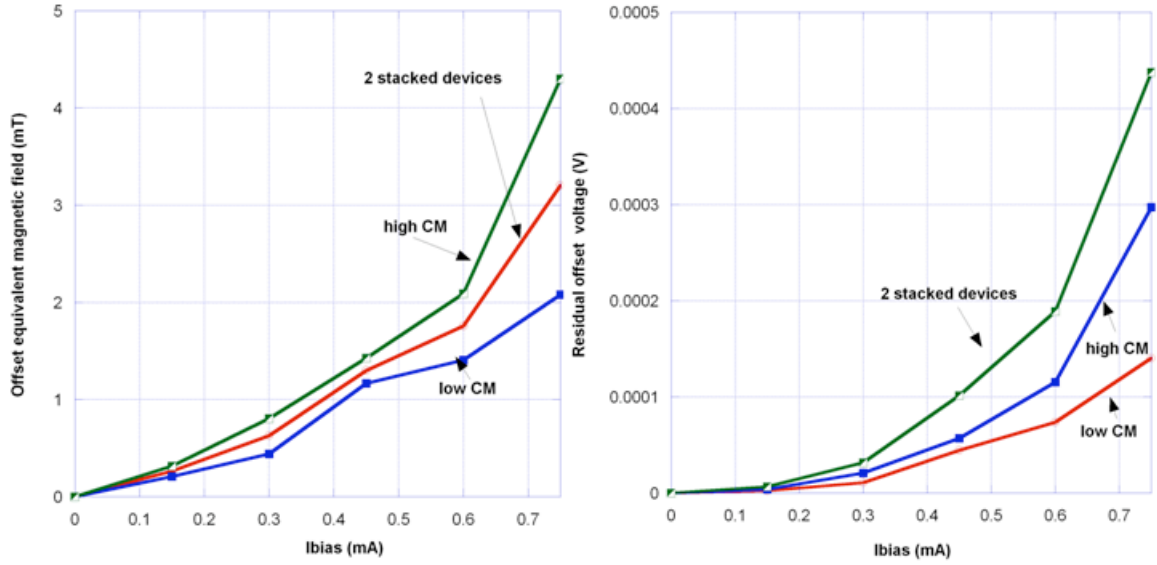
Figure 2.10: Left: the residual offset voltage; right: the residual offset equivalent magnetic field of two series-connected 5C vertical Hall devices

current I, than a single Hall device biased at nI. This is due to the fact that Hall voltage is a linear function of the biasing current, whereas the residual offset voltage is a nonlinear function of the biasing current [45, 47].

The series-connected vertical Hall devices, though requiring more electronics, have better signal-to-noise ratio as compared to their parallel input-parallel output counterparts. The noise of series-connected devices as well as the noise of summing transconductance stages sums up as $\sqrt{n}$, where n is the number of the employed stages. The Hall voltage signal increases n times, thus making signal-to-noise ratio $\sqrt{n}$ times better.

In conclusion, the junction field effect leads to non-ideal matching of series-connected vertical Hall devices. It does not severely affect overall performance of the series connection as long as it is biased at low current. The efficient use of available current and voltage headroom, and high signal-to-noise ratio make of the series-connected devices a good candidate for low power applications.

2.4 Miniaturized Circular Vertical Hall Device

2.4.1 State-of-the-art - Circular Vertical Hall Device (CVHD)

The circular vertical Hall device (CVHD) employed in an angular position sensor was first presented in [48], [5] and [31]. The CVHD is a vertical Hall device (VHD) whose active region is an n-doped ring with N contacts equally distributed along the ring surface, as shown in Fig. 2.11. The device was fabricated in AMS 0.35 μm high voltage (HV) technology. The technology was chosen because it offered deep n-well referred to as the deep N-tub (DNTUB) to enhance the sensitivity of the device.

25
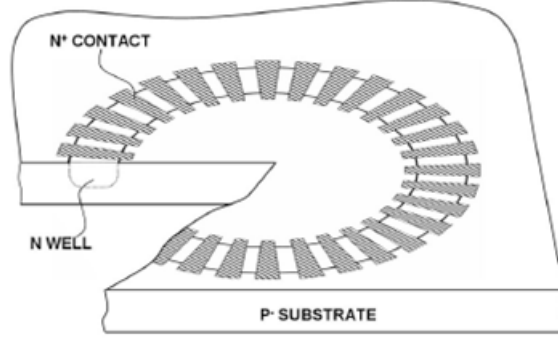
Figure 2.11: Circular vertical Hall device with N contacts (adapted from [5])

The CVHD used in the angular sensor in [31], [5] has 64 contacts. The unit cell is a 5C VHD. This unit 5C cell is biased during a time slot dictated by the clock frequency. The Hall voltage at the sensing contacts of the cell is taken to the signal processing unit on the chip. In the next time slot, the biasing and sensing contacts shift by one contact and the Hall voltage is again retrieved. This is repeated until the full turn around the device has been completed, Fig. 2.12. After a full turn along the ring, the Hall voltage is a step sine wave. This step sine wave is filtered to obtain its first harmonic. The amplitude of the first harmonic is proportional to the in-plane magnetic induction vector, while its phase is proportional to the angle between the vector of magnetic induction and the reference axis of the device, Fig. 2.12. The amplitude of the first harmonic is given by:

$$V_{CVHD} = S_I I_{bias} B \cos(2\pi f_{scan} t - \varphi), \tag{2.17}$$

where S_I is the current-related sensitivity of the 5C unit cell, I_{bias} is the biasing current of the 5C unit cell, B is the magnitude of the in-plane magnetic induction vector, f_{scan} is the frequency corresponding to one full turn around the device and it is 64 times smaller than the clock frequency in the case of 64 CVHD, and the angle φ is the angle included between the magnetic induction vector and the reference axis of the device.

The 5C unit cell is a part of the 64C ring, thus the angle corresponding to its outer contacts, the aperture angle, is 22.5 °. The current-related sensitivity of the 5C unit cell is $S_I = 77$ V/AT. It is somewhat smaller than the current-related sensitivity of the straight 5C VHD possessing the "same" geometry.

The Hall voltage retrieval from the 64CVHD by shifting a 5C cell by one contact substantially decreases 1/f noise and the offset voltage component at the scanning frequency. The input referred-offset equivalent magnetic field of the sensor is 1.5 mT in [5]. The application of the four-phase
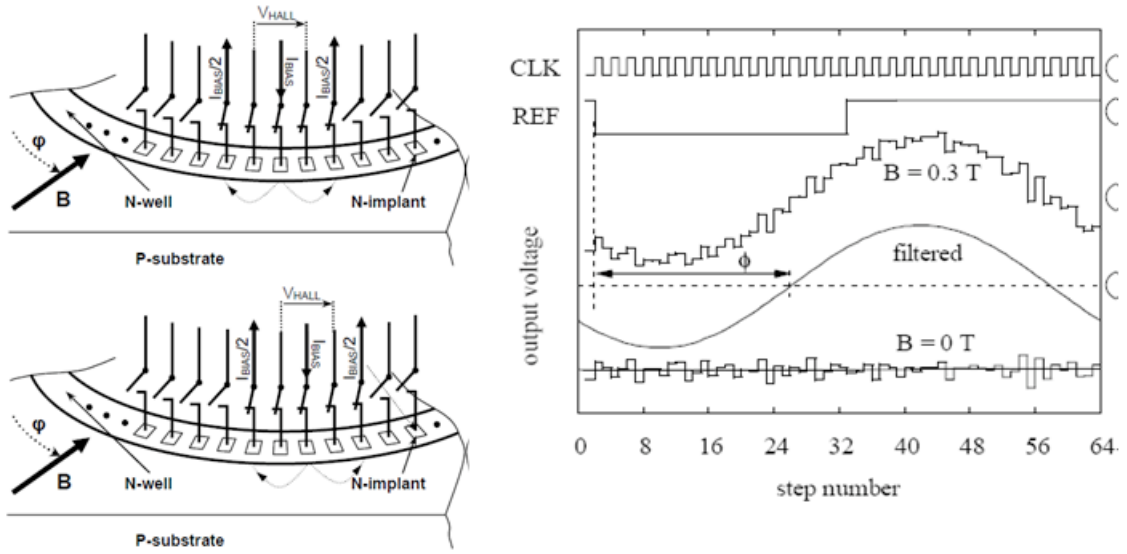
Figure 2.12: Left: Hall voltage retrieval from the 64CVHD by shifting the 5C unit cell by one contact; right: the clock signal, the reference signal to measure the phase, the output voltage, the filtered output voltage, and the offset voltage of the 64CVHD, respectively

spinning current method on the 5C unit cell reduced the offset equivalent magnetic field down to tens of µT.

2.4.2 Sensitivity of the 8-contact circular vertical Hall device (8CVHD)

The large number of contacts efficiently suppresses the offset voltage, as was shown in [5]. However, it limits bandwidth and spatial resolution of the sensor. In order to increase both bandwidth and spatial resolution we designed and studied the 8-contact CVHD (8CVHD), as an ultimate miniaturization of the CVHD [49].

The 8CVHD is shown in Fig. 2.13. The eight contacts is a minimum number of contacts of a CVHD with a unit cell allowing for application of the spinning current method, such as the 5C cell. In addition, for the 5C unit cell, less contacts than eight would result in an aperture angle greater than π. The bigger aperture angle leads to the loss in sensitivity. This is caused by the change in sign of the projection of the magnetic induction vector along the active region of the unit cell.

The 64CVHD was miniaturized such that the width of the n-well, as well as the medium distance between the contacts was maintained. The motivation behind this was to study the influence of the curvature of the active region on the characteristics of the device. The 8CVHD was fabricated in 0.35 µm AMSHV technology. The deep n-well is 3 µm wide, the pitch is 2.8 µm, while the diameter of the device is 16.8 µm.

The angle between the outer contacts of a 5C cell in the 64CVHD is small, π /8, whereas it is π in the 8CVHD. Due to the curvature of the device, the magnitude of the magnetic induction vector varies strongly along the active part of the sensor which leads to drop in sensitivity. The sensitivity
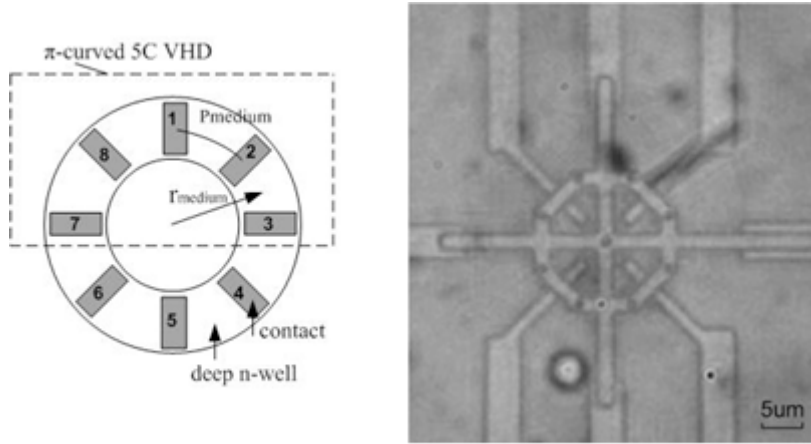
Figure 2.13: The 8CVHD- left: cross-section, right: microphotograph

of one π-curved 5C cell (i.e., contacts 1, 2, 3, 7 and 8 in Fig. 2.14, where 1, 3 and 7 are biasing contacts) can be roughly assessed by noting that sensing contacts 2 and 8 see on average $\sqrt{2}$ smaller magnitude of the in plane magnetic induction vector. Thus the sensitivity of the π-curved 5C cell is $\sqrt{2}$ smaller than that of the straight 5C VHD, or equivalently about 30% less.

The accurate analytical expression for sensitivity of the π-curved device is difficult to obtain. The conformal mapping method used extensively to analytically find sensitivity of a Hall device [3] can not be applied in this case. Neither the active region of the device, nor the vector of magnetic induction satisfy the criteria for application of the conformal mapping method. This is why the finite element calculation was carried out to obtain sensitivity of the π -curved device. The active region of the device was "straighten". It was approximated by the plane whose length is a bit larger than the half circumference of the circle of the medium radius, r_{medium}. The depth was approximated by the junction depth of the n-well − p-substrate, and the distance between the contacts by their medium distance, P_{medium}. The in-plane vector of magnetic induction rotates along the active region of the device and its magnitude is given by a cosine function, Fig. 2.14.

Fig. 2.15 shows the measured sensitivity of the straight 5C cell, and the measured and calculated sensitivities of the π-curved 5C cell. The finite element calculation shows a loss of sensitivity of 33 % compared with the straight 5C device. The maximum sensitivity is 45 V/AT. The measured and calculated sensitivities of the π-curved 5C device differ by 10%.

2.4.3 Device biasing and Hall voltage retrieval

As mentioned above, the 64CVHD is operated by biasing one 5C cell at a time and sensing its Hall voltage. This is repeated until a full turn around the device has been completed. Unlike the CVHDs with greater number of contacts, the 8CVHD can be biased such that the contacts 1 and 5 are at the high biasing potential, while contacts 3 and 7 are at the low biasing potential, Fig. 2.16. This is
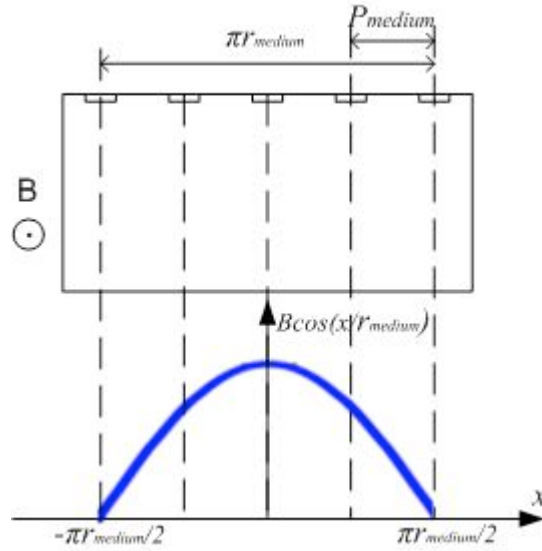
Figure 2.14: Approximate model of the π-curved 5C cell for numerical calculations
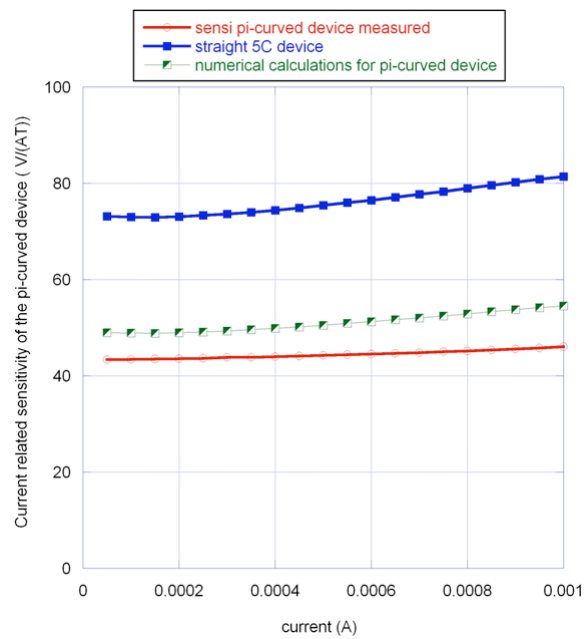
Figure 2.15: Measured sensitivity of the straight 5C cell, and calculated and measured sensitivities of the π-curved 5C

referred to as the first sensing step. In this way, each biasing contact sources or sinks equal current, i.e., the current density at each contact is identical. This is not the case in a standard 5C VHD, as discussed above.

The initial topology, given in Fig. 2.16 top left, is rotated by one contact, Fig. 2.16 top right, until a full turn has been completed. It takes eight sensing steps to obtain the Hall voltage from the 8CVHD. In this way an eight step sine wave is obtained, as shown in Fig. 2.16 bottom. The equality of current densities is kept throughout all biasing and sensing phases. This is why we termed this type of biasing as symmetric.

It should be noted here that the output signal of a CVHD is a step sine wave whose resolution is determined by the number of contacts. The output of a CVHD is filtered out in order to obtain the first harmonic of the step sine wave. The amplitude of the first harmonic is directly related to the number of the CVHD's contacts. Supposing the same sensitivity of the 8CVHD and the 64CVHD, the first harmonic of the 8CVHD is by 9% smaller than that of the 64CVHD.

In addition to the sensing of two orthogonal Hall voltages, as shown in Fig. 2.16, this biasing topology also allows for summing the Hall voltages at the opposite pairs of contacts due to their same polarity. For example, the Hall voltage between the pair of contacts 8 and 2, and 6 and 4 is of the same polarity and can be summed by means of electronics.

2.4.4 Residual offset of the 8CVHD

It was shown in [5] that the two parameters to characterize the offset behavior of a CVHD are:

1) DC offset - the sum of offset voltages in all sensing steps over one full turn. The DC offset cancels out for the ohmic modeling of offset voltage in the ideal case. In the real case, there is a finite DC value that can be filtered out by a high pass filter. after the preamplifier.

2) the first harmonic of the offset voltage hereafter also referred to as the residual offset by analogy with a standard Hall cell. Any discrete function can be decomposed into sum of harmonics. The offset component at the scanning frequency adds to the useful Hall voltage of a CVHD altering its magnitude and phase. It can not be filtered out as the DC offset and it causes an error.

It was also shown in [5] that the first harmonic of offset voltage is inversely proportional to the number of contacts (at the power 3/2) for an ohmic model of the CVHD. Consequently, the reduction in the number of contacts while keeping the same biasing and sensing topology invariably leads to an increase in the residual offset. However, due to its compactness and symmetry, the 8CVHD offers the possibility of symmetric biasing which may compensate for this increase. The 8C devices from two runs in AMS 0.35 µm high voltage technology were tested for DC offset and residual offset for the two biasing topologies. The average offset per one sensing step was about 50 mT. The symmetric biasing topology, where the whole device was biased, was compared with the 5C unit cell shifting, Fig. 2.17. The biasing of the 8CVHD was performed manually.
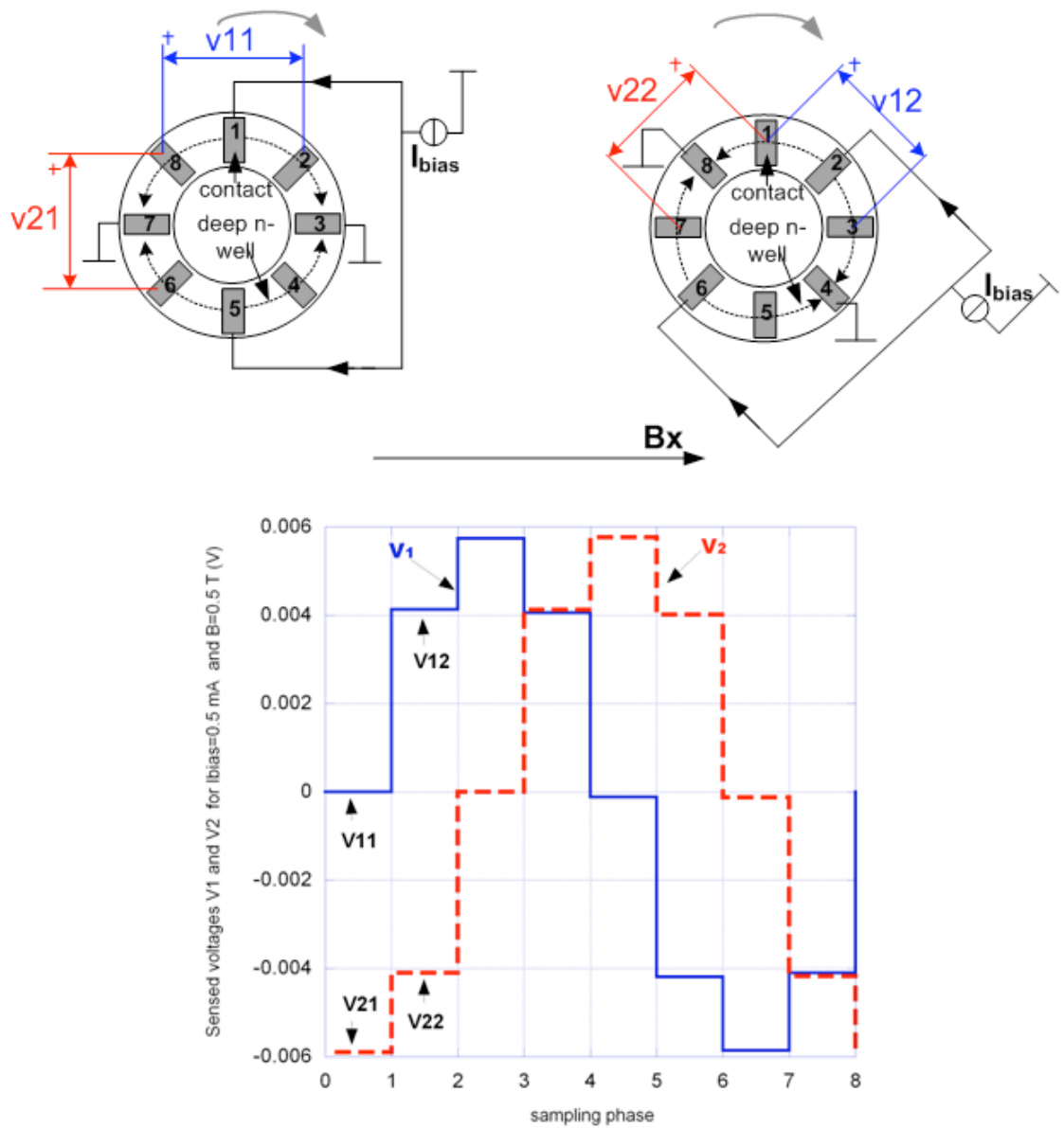
Figure 2.16: Biasing and Hall voltage retrieval from the 8CVHD. There are four biasing contacts each of which sources or sinks equal current. Top left: the initial topology, top right: the initial topology rotated by one contact, bottom: the output Hall voltage of the 8CVHD after one full turn
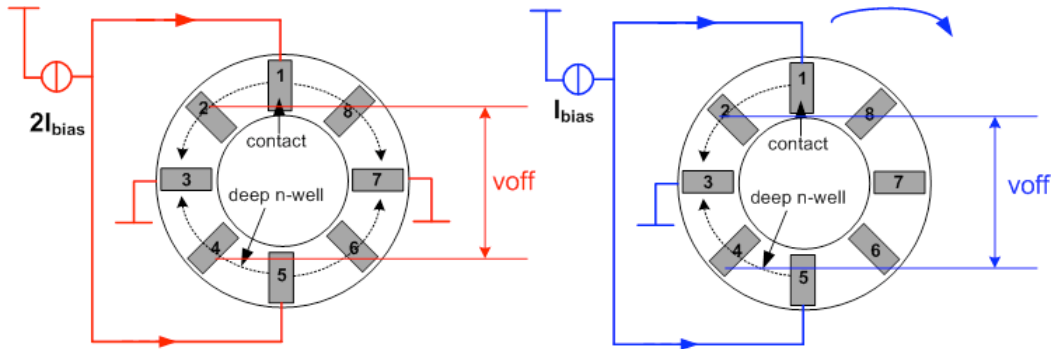
Figure 2.17: Symmetric biasing compared with the 5C unit cell shifting in the 8CVHD
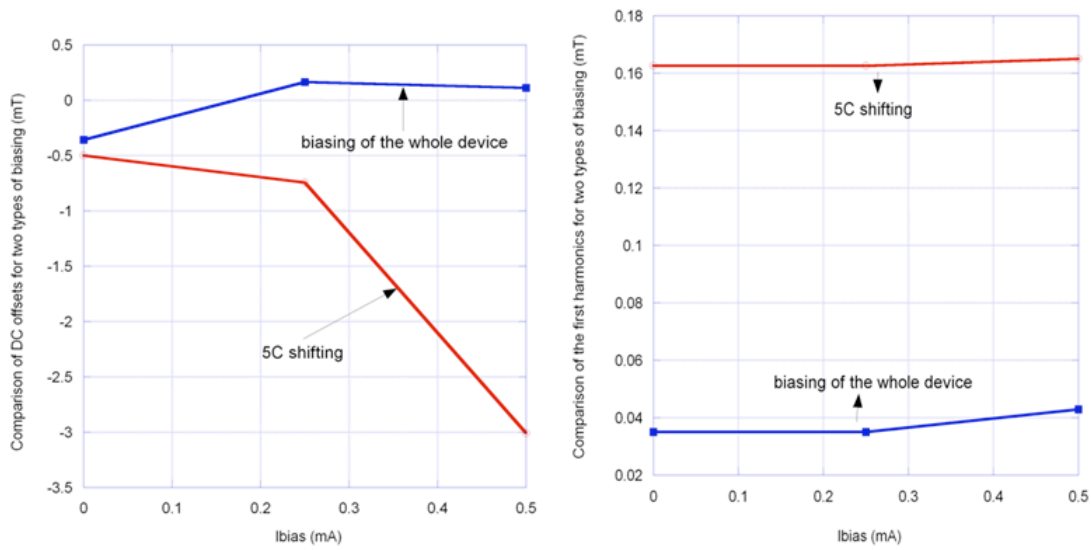
Figure 2.18: Comparison of the DC offset (left) and the first harmonic of the offset (right) between the symmetric biasing of the whole device and the 5C cell shifting

The DC offset is substantially larger for higher biasing currents in the case of the 5C cell shifting. The amplitude of the first harmonic of the offset, or equivalently the residual offset, is about an order of magnitude lower for the symmetric biasing topology, Fig. 2.18.

2.4.5   Device optimization

The 8CVHD analyzed above was extremely miniaturized. We went beyond the safe distances defined in the design rules of the technology. The extreme miniaturization leads to touching of the DNTUB diffusions, as illustrated in the cross section of the 8CVHD in Fig 2.19.

The consequence of the extreme miniaturization is the sensitivity of the 8CVHD to the perpendicular component of the magnetic field. Namely, there is a conductive path between the two diametrically opposed contacts on the N-well ring due to the overlapping DNTUB diffusions. This conductive path is a high resistive one due to a lower doping concentration at the depth where the two diffusions touch. However, the two diametrically opposed contacts are at the same potential
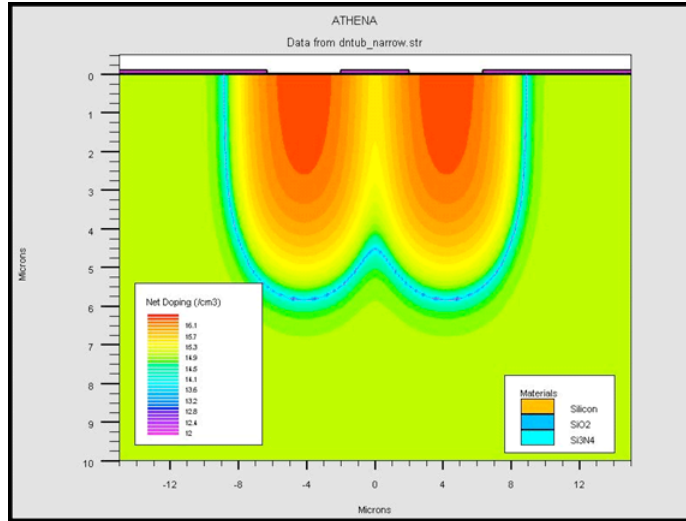
Figure 2.19: FEM simulations of the cross section of the miniaturized 8CVHD where the distance between DNTUB diffusions is smaller than prescribed by the technology design rules. The extreme miniaturization leads to touching of the DNTUB diffusions

when the 8CVHD is biased as shown in Fig. 2.16. Consequently, there is no current path between them. Nevertheless, the current lines between any two contacts (e.g., contacts 1 and 3) are not confined to the drawn width of the DNTUB. There is a current leakage through the inside of the ring connecting the two contacts. This current leakage is small due to a high resistive path. In addition, the current density in the active region is uneven due to the curvature of the active region. These two phenomena lead to a different potential distribution on the two sensing contacts of the π-curved 5C cell. This is why the Hall voltage arises in the presence of the perpendicular magnetic field. Further investigation and modelling of the 8CVHD's sensitivity to the perpendicular component of the magnetic field is left out as the future work.

Nevertheless, the Hall voltage proportional to the in-plane component can be easily distinguished from the Hall voltage proportional to the perpendicular component of the magnetic field. The former has half-circular symmetry, while the later has circular symmetry. In other words, if the Hall voltages from the opposite pairs of contacts are summed, the sum is proportional to the in-plane component of the magnetic field. In contrast, if the Hall voltages from the opposite pairs of contacts are subtracted, the difference is proportional to the perpendicular component of the magnetic field.

The optimization of the 8CVHD can be performed by either altering the process (or choosing another one) and by geometry optimization. The deep N-well (DNTUB) was chosen as the active region of the device because of its high junction depth. The junction depth is crucial to the sensitivity of vertical Hall devices, as discussed in Section 2.2. If we were able to alter the technology process, we would have opted for the increase in the implantation energy of the N-well. The increased implantation energy would push down the junction depth of the DNTUB - p-substrate. This in turn
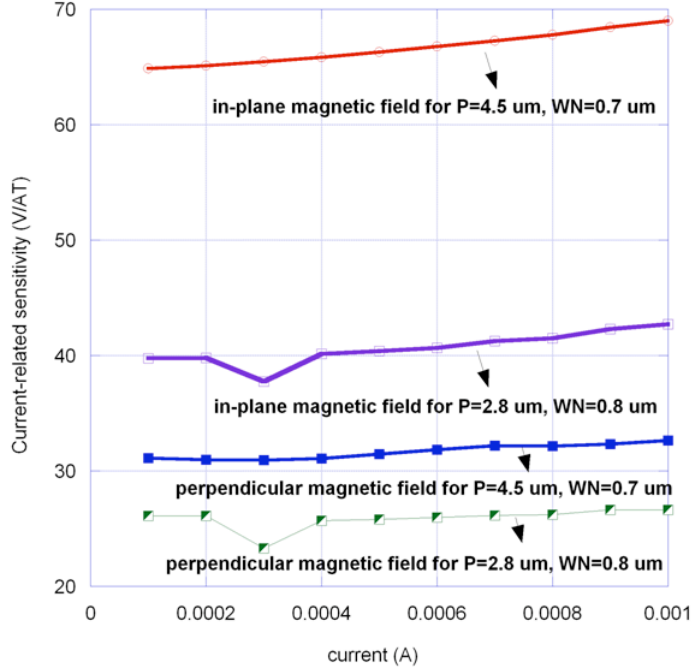
Figure 2.20: Comparison of sensitivities to the perpendicular and the in-plane components of the magnetic field between the miniaturized (P= 2.8 µm, WN= 0.8 µm) and optimized (P= 4.5 µm, WN= 0.7 µm) devices. The DNTUBs diffusions touch in the miniaturized device, which is not the case for the optimized device .

would increase the sensitivity of the device.

Speaking of geometry optimization, it is the medium pitch of the contacts P_{medium} and the width of the DNTUB that can serve as design parameters.

For a given medium pitch, the current-related sensitivity S_I can be increased by reducing the width of the DNTUB region. The thinner the device, the greater is influence of the junction field effect on the active region, or equivalently, nonlinearity is greater. This leads to worse offset voltage suppression by the spinning current method. The voltage-related sensitivity S_V remains more or less the same.

For a given DNTUB width, the increase of pitch leads to higher current-related sensitivity S_I with a slight drop in voltage-related sensitivity S_V. The DNTUB ring of a greater diameter prevents touching of DNTUB diffusions. Fig. 2.20 shows the comparison between the two devices: the extremely miniaturized one (the width of the DNTUB 3 µm, the inner radius of the DNTUB ring 5.4 µm, $P_{\mathrm{medium}}{\approx}\,2.8$ µm, and the contact width WN= 0.8 µm) and the optimized one with a larger radius of the DNTUB ring (the width of DNTUB 3 µm, the inner radius of the DNTUB ring 13 µm, $P_{\mathrm{medium}}{\approx}\,4.5$ µm, and the contact width WN= 0.7 µm). The optimized device features higher ratio of the sensitivity to the in-plane component vs. sensitivity to the perpendicular component.

2.5　Conclusions

This chapter gave an overview of vertical Hall devices, with the emphasis on means to increase voltage-to-residual offset and voltage-to-noise ratios. To this end, the series-input series-output topology of an array of vertical Hall devices was studied.

The chapter then dealt with the circular vertical Hall device (CVHD). We have designed and tested the 8-contact circular vertical Hall device (8CVHD) as an ultimate miniaturization of the 64-contact circular vertical Hall device. We have shown that the sensitivity of a π-curved 5-contact vertical Hall device, which is a unit cell of the 8CVHD, is about 30 % less than the sensitivity of a straight 5-contact vertical Hall device. The offset components, the DC offset and the first harmonics of offset, increase with reduction of the number of contacts. Nevertheless, it was shown that this is not the case for the 8CVHD if the symmetric biasing is employed. The symmetric biasing, where the whole device is biased in all sensing phases, offers better offset reduction as compared with the biasing of one 5-contact cell at a time.

Chapter 3

Bandwidth increase in Hall sensors based on the 8CVHD

This chapter addresses limitations of bandwidth increase while keeping satisfying accuracy in Hall sensors employing spinning current method for offset reduction. It will be shown that in CMOS integrated Hall sensors both the design of a Hall device and the interface electronics determine the contribution of voltage spikes to the overall sensor's accuracy. The model of the ideal Hall device and the interface electronics containing spinning switches and preamplifier is presented. The nonidealities of the device and electronics are then added to the ideal model and discussed. Finally, three solutions to tackling the challenge of increasing the spinning frequency while maintaining the accuracy in the sensors based on the 8CVHD are presented. The first one is a novel solution relying on the high input capacitance of the preamplifier which together with the sensing switch on-resistance filters out the voltage spikes. The second solution examines the partial guard band to remove a part of the spikes' energy without compromising the high spinning frequency. The third solution is based on the cancellation of the voltage spikes by the clockwise and counterclockwise spinning current method on two devices. The novelty with respect to previous solutions lies in the additional pair of the clockwise and counterclockwise devices. The spinning current method is applied with a time shift on the additional pair of devices. The outcome is that due to mismatches, the residual spikes of arbitrary amplitude are distributed over the spinning phase (sensing phase for the 8CVHD) and behave like noise.

3.1 Spinning current method as a limitation to bandwidth increase

The spinning current method leads to parasitic voltage spikes due to commutation of the biasing and sensing contacts, as mentioned in Chapter 1.

It was first pointed out in [11] that each commutation of contacts requires the transient time before the Hall voltage settles on the sense contacts. The transient time is needed for the parasitic

capacitances associated with the device's contacts to change state from one spinning current phase to another. The voltage sensed by the preamplifier during the transient time is transition of voltage from either the biasing high or low levels to the common mode voltage of the sensing contacts. Thus the preamplifier "sees" voltage spikes of positive or negative polarity with respect to the common mode voltage. The voltage spikes are characterized by their polarity, amplitude and settling time.

In [11] the spike settling time was determined by the output resistance and the contact's capacitance of a Hall device. In the same paper, it was noted that the settling time limits the maximum spinning frequency, and consequently the bandwidth of a Hall sensor. The settling time of spikes is a negligible part of the spinning phase for low spinning frequencies. In contrast, when increasing the spinning frequency it can consume the whole spinning phase and severely affect the measurement accuracy.

Several solutions to eliminate or reduce the spinning spikes were reported in literature. The so called guard-band solution was adapted from the chopper-amplifier design [50]. The idea behind the guard band is to delay the demodulation switch control signals with respect to the modulation switch control signals. The delay time equals spikes' settling time. In this way, the output Hall voltage of the traditional spinning current Hall sensor is free of spikes. In [51] was proposed the solution based on the clockwise and counterclockwise spinning. Namely, the spinning on a Hall device is performed alternatively in the clockwise and counterclockwise directions. The sign of the Hall voltage remains the same, while the voltage spikes reverse polarity and can be averaged out. These two solutions remove the spikes but they limit the bandwidth of the sensor. In order to remove the bandwith constraint in[52] was proposed the clockwise and counterclockwise spinning on the two matched Hall devices. The spinning current is performed clockwise for the first device, and counterclockwise for the second one. The output voltages of the two devices with spikes of reversed polarity are brought to a chopper amplifier via a multiplexer.

In all solutions stated above the analysis of voltage spikes took into account only the characteristics of a Hall device: its output resistance and the contacts' capacitances. To our knowledge, the influence of the interface electronics containing the spinning switches and a preamplifier was not analyzed in literature so far. Nevertheless, it is both the design of a Hall device and the interface electronics that determine the contribution of voltage spikes to the overall sensor's accuracy. The focus on the interface electronics is all the more important when trying to push up the limits of the maximum spinning frequency while keeping satisfying accuracy.

3.1.1   Ideal model of the horizontal Hall device and interface electronics

In Fig. 3.1 are sketched two phases of the four-phase spinning current method applied to a horizontal Hall cell. The cell is biased at a constant current I_{bias}. The spinning current method is performed
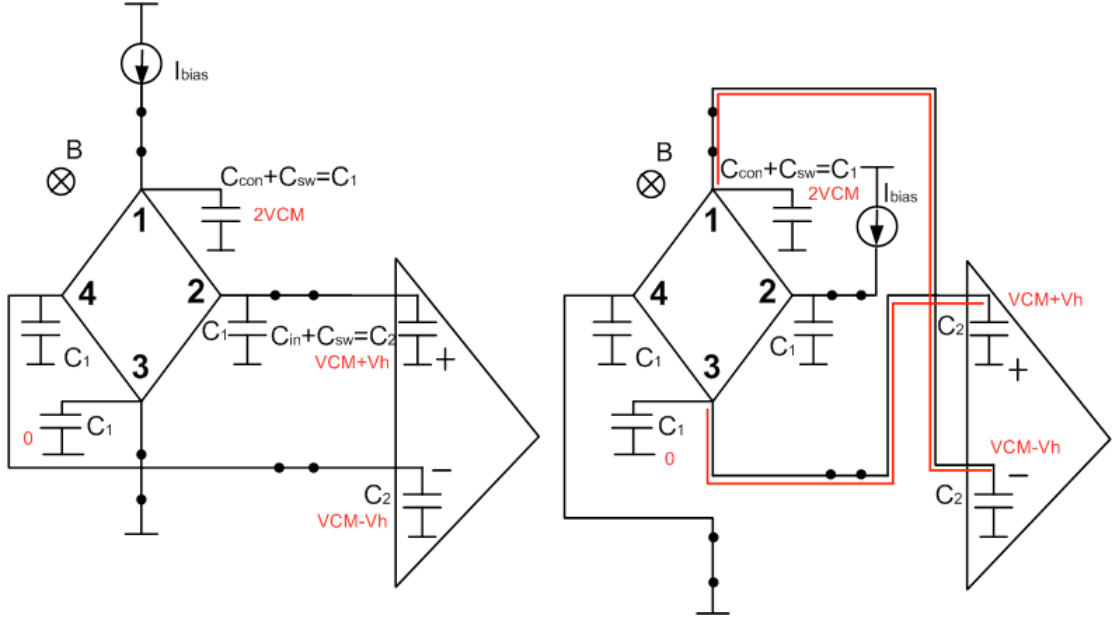
Figure 3.1: First two phases of the four-phase spinning current method applied to a horizontal Hall device: left - the first spinning phase, right - the second spinning phase (the on-resistance of the switches is left out for simplicity)

such that the Hall voltage is taken as a DC signal. For the time being, the offset voltage will be left out. The switching on of the biasing and sensing switches is assumed instantaneous and synchronous.

The simplified equivalent model of the complementary switch in the on-state [18] is given in Fig. 3.2a). Fig. 3.2b) shows the equivalent schematics of the Hall device, switches and the preamplifier at the beginning of the second spinning current phase. The half of the output resistance of the Hall device R_{outHall} is associated with one contact and denoted by R_1. Each contact of a Hall device is connected to the four switches, two biasing and two sensing switches, one of which is in the on-state at any time. The switches in the off-state also contribute to the overall contact capacitance [18]. The sum of the capacitances of the Hall contact and the switches is labeled as C_1. The on-resistance of the switch is labeled as R_2. The sum of the capacitance of the sensing switch and the input capacitance of the preamplifier is denoted by C_2 .

The voltage drop on the Hall device is denoted as $2V_{CM}$. It is determined by the input resistance of the Hall device and the biasing current:

$$2V_{CM} = R_{IN}I_{bias} \tag{3.1}$$

In the case of a symmetric Hall device such as the horizontal Hall device, the input resistance is equal to the output resistance.

The voltage drop on the biasing switch connected to ground is disregarded without the loss of generality.
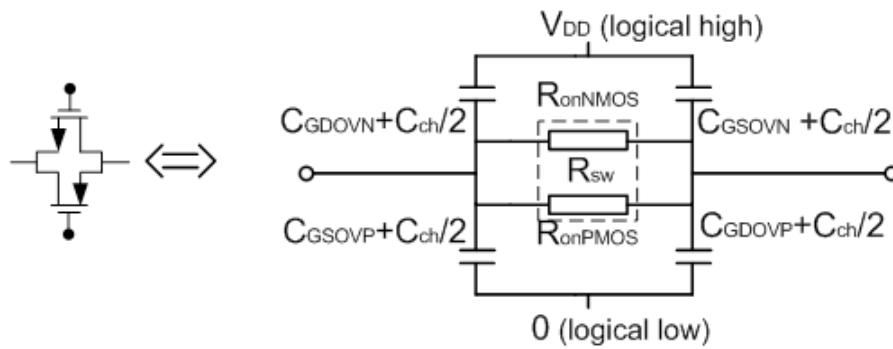
(a) Distributed model for the complementary switch
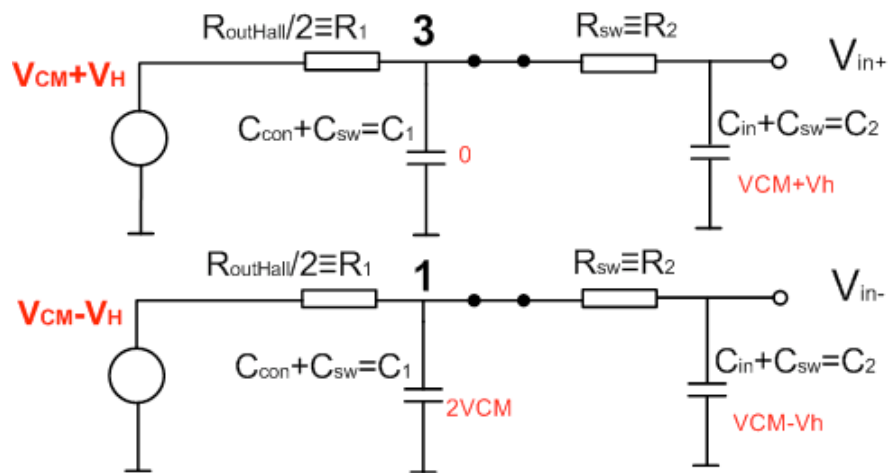
(b) The second spinning current phase

Figure 3.2: Model of the sensing contacts of the horizontal Hall device, switches and preamplifier

According to Fig. 3.2 b) the current charging the input capacitance C_2 is given by:

$$\frac{\partial^2 i_2(t)}{\partial t^2} + k_1 \frac{\partial i_2(t)}{\partial t} + k_2 i_2(t) = 0, \tag{3.2}$$

where

$$k_1 = \frac{(R_1 + R_2)\,C_2 + R_1 C_1}{R_1 C_1 R_2 C_2}, \tag{3.3}$$

and

$$k_2 = \frac{1}{R_1 C_1 R_2 C_2}. \tag{3.4}$$

The Eqn 3.2 is a homogeneous ordinary differential equation whose solution is:

$$i_2(t) = A_1 e^{p_1 t} + A_2 e^{p_2 t}, \tag{3.5}$$

where A_1 and A_2 are constants, p_1 and p_2 are the roots of the characteristic equation and are as follows:

$$p_{1/2} = \frac{-\left[(R_1 + R_2)\,C_2 + R_1 C_1\right] \pm (R_1 + R_2)\,C_2 \sqrt{1 + 2\frac{R_1(R_1 - R_2)}{(R_1 + R_2)^2}\frac{C_1}{C_2} + \frac{R_1{}^2}{(R_1 + R_2)^2}\left(\frac{C_1}{C_2}\right)^2}}{2 R_1 C_1 R_2 C_2}. \tag{3.6}$$

The initial conditions for the current at the positive and negative preamplifier's inputs are given by, respectively:

$$i_2^+(0) = -\frac{V_{CM} + V_H}{R_2}, \tag{3.7}$$

$$i_2^-(0) = \frac{V_{CM} + V_H}{R_2}. \tag{3.8}$$

The voltage at the inputs of the preamplifier is as follows:

$$v_2^+(t) = V_{CM} + V_H + \frac{1}{C_2}\left(\frac{A_1}{p_1}e^{p_1 t} + \frac{A_2}{p_2}e^{p_2 t}\right), \tag{3.9}$$

$$v_2^-(t) = V_{CM} - V_H + \frac{1}{C_2}\left(\frac{A_1}{p_1}e^{p_1 t} + \frac{A_2}{p_2}e^{p_2 t}\right), \tag{3.10}$$

with the conditions:

$$v_2^+(\infty) = V_{CM} + V_H, \tag{3.11}$$

$$v_2^-(\infty) = V_{CM} - V_H. \tag{3.12}$$

Due to its complexity, Eqn 3.6 will be solved for the three distinct realistic cases:

1) the capacitance associated with the preamplifier's input is much greater (at least one order of magnitude) than the capacitance associated with a Hall contact: $C_2 >> C_1$. The surface of the transistors in the differential pair of the preamplifier can be significant in order to increase their transconductance to design for low input-referred noise [18]. Another motivation for large input transistors is low input-referred offset by device matching. On the other hand, miniaturization of Hall devices in the last decade has led to decrease in the contact's capacitance;

2) the capacitance associated with the preamplifier's input is about the same as the capacitance associated with a Hall contact: $C_2 \approx C_1$;

3) the capacitance associated with a Hall contact is much greater than the capacitance associated with the preamplifier's input $C_1 >> C_2$.

In the first case, assuming $C_2 >> C_1$, from Eqn 3.6 to Eqn 3.12 one obtains for the voltage at the inputs of the preamplifier:

$$v_2^+(t) = V_{CM} + V_H - \frac{C_1}{C_2}\frac{R_1}{R_1 + R_2}\left(V_{CM} + V_H\right)\left(e^{-\frac{1}{(R_1+R_2)C_2}t} - e^{-\frac{R_1+R_2}{R_1 R_2 C_1}t}\right),\qquad(3.13)$$

$$v_2^-(t) = V_{CM} - V_H + \frac{C_1}{C_2}\frac{R_1}{R_1 + R_2}\left(V_{CM} + V_H\right)\left(e^{-\frac{1}{(R_1+R_2)C_2}t} - e^{-\frac{R_1+R_2}{R_1 R_2 C_1}t}\right).\qquad(3.14)$$

The differential voltage at the preamplifier's input is given by:

$$v_2^+(t) - v_2^-(t) \approx 2V_H - 2\frac{C_1}{C_2}\frac{R_1}{R_1 + R_2}\left(V_{CM} + V_H\right)\left(e^{-\frac{1}{(R_1+R_2)C_2}t} - e^{-\frac{R_1+R_2}{R_1 R_2 C_1}t}\right).\qquad(3.15)$$

In the second case, assuming $C_2 \approx C_1$, from Eqn 3.6 to Eqn 3.12 one obtains the differential voltage at the preamplifier's input:

$$v_2^+(t) - v_2^-(t) \approx 2V_H + \left(V_{CM} + V_H\right)\left(e^{-\frac{2}{R_2 C_1}t} - e^{-\frac{1}{2R_1 C_1}t}\right).\qquad(3.16)$$

In the third case, assuming $C_1 >> C_2$, Eqn 3.6 to Eqn 3.12 yield the differential voltage at the preamplifier's input:

$$v_2^+(t) - v_2^-(t) \approx 2V_H + 2\left(V_{CM} + V_H\right)\left(e^{-\frac{1}{R_1 C_1}t} - e^{-\frac{1}{R_2 C_2}t}\right).\qquad(3.17)$$

The voltage spikes due to the spinning current method are characterized by their polarity, amplitude and settling time, as mentioned above. The voltage spike given by Eqn 3.15 is sketched in Fig. 3.3.

The differential amplitude of the voltage spike, assuming $C_2 >> C_1$, is:

$$A\mid_{C_2 \gg C_1} \approx 2\frac{C_1}{C_2}\frac{R_1}{R_1 + R_2}\left(V_{CM} + V_H\right)e^{-\frac{R_1 R_2 C_1}{(R_1+R_2)^2 C_2}} \approx 2\frac{C_1}{C_2}\frac{R_1}{R_1 + R_2}\left(V_{CM} + V_H\right),\qquad(3.18)$$
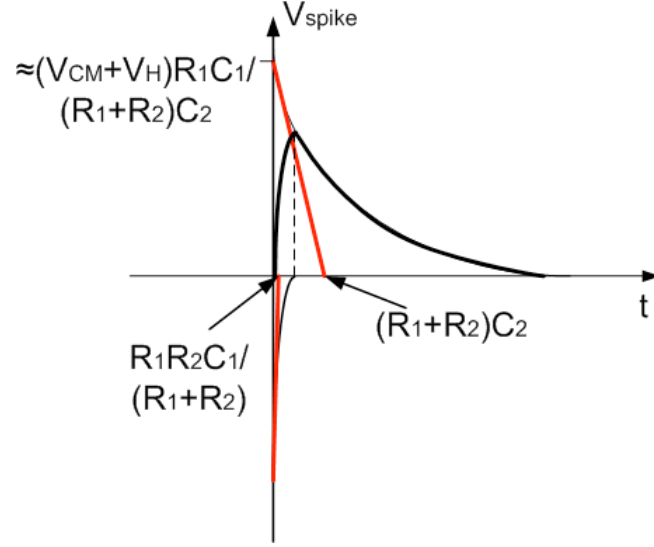
Figure 3.3: Voltage spike in the case of $C_2 >> C_1$

whereas its settling time is approximated by the greater time constant, and equals seven time constants for 0.1 % accuracy [17]:

$$t_{settling}\mid_{C_2\gg C_1} = 7\tau_1 = 7\left(R_1 + R_2\right)C_2. \tag{3.19}$$

In the second case, $C_2 \approx C_1$, the greater time constant is defined by the Hall output resistance. The switch on-resistance should be designed smaller than the Hall output resistance in order to avoid adding the noise at the input (see Chapter 4). In the case $R_2 << R_1$, the differential amplitude of the voltage spike can be approximated by:

$$A\mid_{C_2\approx C_1} \approx \left(V_{CM} + V_H\right)e^{-\frac{R_2}{4R_1}} \approx V_{CM} + V_H, \tag{3.20}$$

while its settling time is given by:

$$t_{settling}\mid_{C_2\approx C_1} = 7\tau_2 = 7(2R_1C_1). \tag{3.21}$$

For the third case $C_1 >> C_2$, the differential amplitude of the spike and its settling time are as follows:

$$A\mid_{C_2\gg C_1} = 2\left(V_{CM} + V_H\right)e^{-\frac{R_2C_2}{R_1C_1}} \approx 2\left(V_{CM} + V_H\right), \tag{3.22}$$

$$t_{settling}\mid_{C_2\gg C_1} = 7\tau_3 = 7R_1C_1. \tag{3.23}$$

The evolution of the spike's time constant and amplitude with respect to the ratio of the capacitances C_2 and C_1, according to Eqn 3.15, Eqn 3.16 and Eqn 3.17, is given in Fig. 3.4.

43
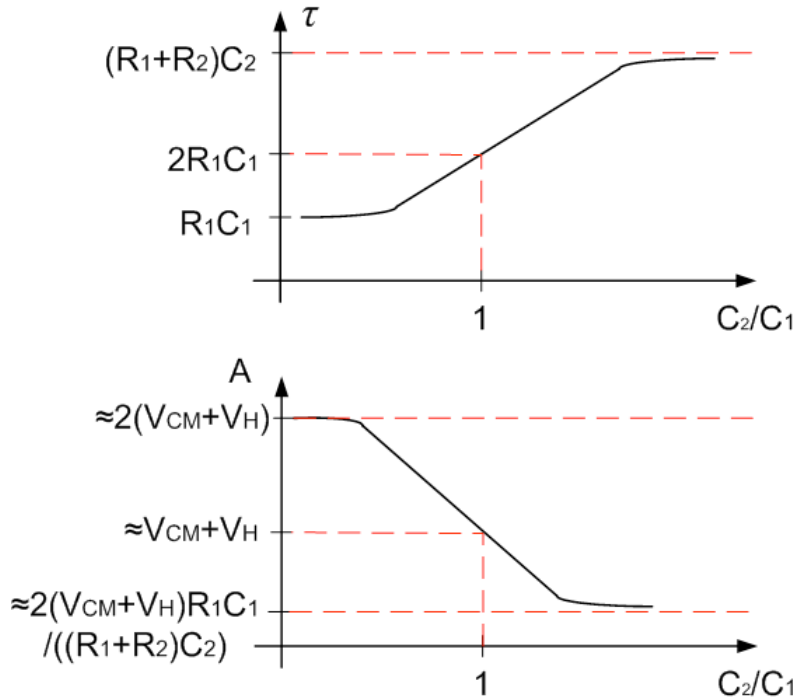
Figure 3.4: Voltage spike's time constant (top) and amplitude (bottom) as a function of C_2/C_1

The greater the ratio C_2/C_1, the smaller is the voltage spike's amplitude. In this case, the resistance R_2 together with the capacitance C_2 behaves as a low pass filter that greatly attenuates the amplitude of the spikes. These two design parameters can be increased by reducing aspect ratio of the transistors in the complementary switch, and increasing that of the input stage's transistors. Nevertheless, the settling time of the spikes is increased in this case. This requires longer spinning phases, or, equivalently, a lower spinning frequency.

For example, for $C_2 = 10$ pF, $R_2 = 1$ kΩ, $R_1 = R_{IN} = 1$ kΩ, $C_1 = 0.5$ pF, and $I_{bias} = 0.1$ mA, the voltage drop on the Hall device is $2V_{CM} = 200$ mV, according to Eqn. 3.1. According to Eqn 3.18 the spike's differential amplitude is 5 mV, or only 2.5 % of the voltage drop on the Hall device.

According to Eqn 3.19 the settling time is 140 ns, which is equivalent to the maximum spinning frequency of about 7 MHz. This is more than enough for a four-contact horizontal Hall device but not enough for a high bandwidth sensor based on the 8CVHD (see also 3.1.2).

The expected amplitude of the spikes sets design specifications for the gain of the preamplifier. The gain of the preamplifier should be low in order to avoid saturation of the output stage. The saturation of the output stage of the preamplifier introduces nonlinearity, i.e., unwanted spectral components in the signal.

The influence of the spikes on the measurement accuracy is best illustrated in the frequency domain. The spikes were approximated by their greater time constant, or equivalently, their discharge
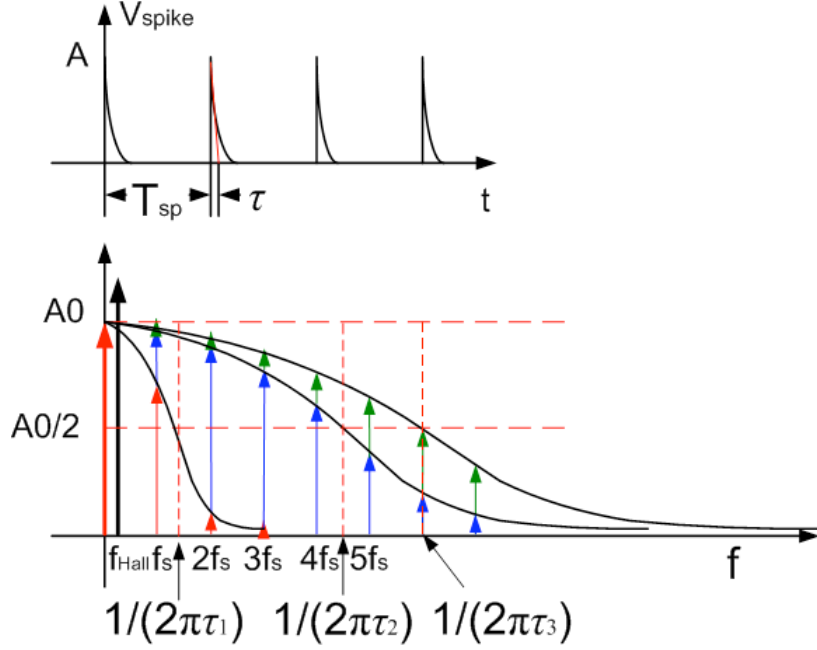
Figure 3.5: The sketch of the amplitude-frequency spectrum of the spikes waveform for the three cases analyzed above. The DC component is approximately equal in all three cases, under the assumptions on the ratio of capacitances.

time. The frequency spectrum of the spikes waveform having the same polarity and amplitude, Fig. 3.5 top, is sketched in Fig. 3.5 bottom.

The frequency spectrum consists of the components at the multiples of the spinning frequency under the low pass filter envelope:

$$A_0 \approx A\tau f_s, \tag{3.24}$$

$$\mid A_n \mid \approx A\tau f_s \frac{1}{\sqrt{1 + (2n\pi f_s \tau)^2}}, \tag{3.25}$$

where A is the amplitude of spikes, τ is the time constant and f_s is the spinning frequency.

The voltage spike's DC component is proportional to the spinning frequency. The upper harmonics are also proportional to the spinning frequency, but they are attenuated by the low pass filter transfer function. The larger the time constant of the low pass filter formed by R_2 and C_2, the lower are the spike's spectral components. The maximum frequency of the Hall signal, denoted in Fig. 3.5 by f_{Hall}, should be at least an order of magnitude smaller than the 3dB frequency of the low pass filter formed by R_2 and C_2 . This must be ensured in order to avoid the attenuation of the Hall signal, as well as the unwanted phase shift!

The DC component for the three cases above is approximately the same under the assumptions concerning the ratio of the capacitances C_1 and C_2, and the resistances R_1 and R_2:

45
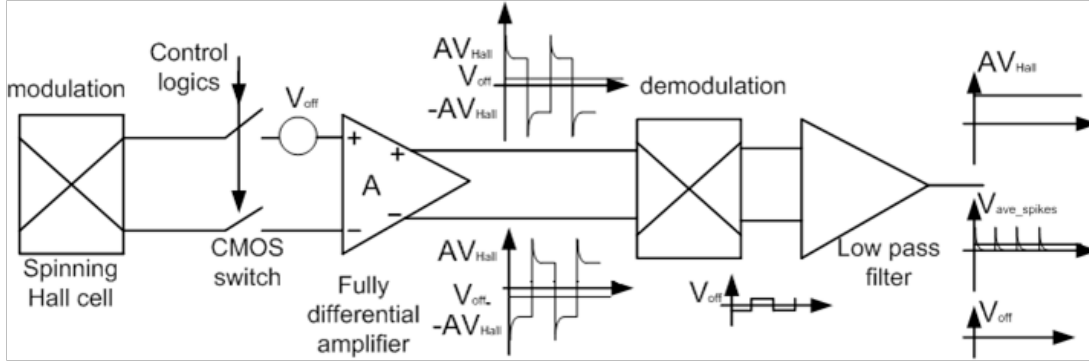
Figure 3.6: Low-pass filtered spikes add up to the useful Hall voltage in the traditional spinning current-demodulation Hall sensor

$$A_0 = C_1 R_1 R_{IN} I_{bias}. \tag{3.26}$$

In order to better filter out the spike's spectral components, it is recommended to choose the spinning frequency at least several times higher than the highest frequency of interest in the measured signal. However, there is a trade-off between this frequency separation and the increase of the spike's DC component. In Hall sensors topologies employing low pass filter this DC component can not be filtered out.

The above analysis was performed for the spinning current method where Hall voltage is taken as a DC signal. In the traditional topology shown in Fig. 3.6 the chopper principle is employed. The Hall voltage is taken as an AC signal in order to remove the offset voltage of the preamplifier. The voltage spikes are of reverse polarity in the two subsequent spinning phases. Their spectral content is similar to the one shown in Fig 3.5, except that the spectral components are at the odd multiples of the spinning frequency. For the DC magnetic field, the spectral components of the spikes add to the spectral components of the modulated Hall signal. They can not be distinguished from the useful Hall voltage. After demodulation, the spikes waveform contains spikes of the same polarity. Thus the analysis shown above can be applied to estimate the error caused by the spikes after low-pass filtering, Fig. 3.6.

3.1.2 Realistic model of the horizontal Hall device and preamplifier

The equations in the section 3.1.1 were obtained under the ideal conditions: a symmetric Hall device without offset, instantaneous switching on/off of the switches, matched switches with synchronous control signals, constant on-resistance of the switch and no charge-injection [2], and symmetric inputs of the preamplifier. The Hall voltage was also considered equal in all spinning current phases.

The offset voltage in one phase of the spinning current method can be modelled by the different output resistance R_1, and the different common mode voltage V_{CM} due to different input resistance

R_{IN}. This is in agreement with the ohmic modelling of the offset voltage [3]. In this way, the offset voltage in one spinning phase affects the amplitude and the settling time of the spike.

The switching on/off of the switches was considered synchronous. This implies synchronous control signals for the sensing switches. If this is not the case, the shifted switching leads to the different amplitudes of the spikes. This is due to the partial discharging/charging of the capacitance C_1 through the output resistance R_1 while "waiting" for the sensing switch to close.

The on-resistance of the complementary switch depends on the aspect ratio of the transistors in the switch, as well as on the input voltage to the switch. Assuming the quadratic model of the transistor, the on-resistance of the switch is given by [2]:

$$R_{on} = R_{onPMOS} \parallel R_{onNMOS} = \frac{1}{\beta_N \left(V_{DD} - V_{THN}\right) - \left(\beta_N - \beta_P\right) V_{IN} - \beta_P \mid V_{THP} \mid}, \quad (3.27)$$

where the gain factors of the transistors are:

$$\beta_{N,P} = \mu_{N,P} C_{ox} \left(\frac{W}{L}\right)_{N,P}, \quad (3.28)$$

where $\mu_{\text{N,P}}$ is the electron/hole mobility, C_{ox} is the oxide capacitance, $(W/L)_{\text{N,P}}$ is the aspect ratio of the transistors, V_{DD} is the supply voltage, V_{IN} is the input voltage to the switch, V_{THN} and V_{THP} are the threshold voltages of the NMOS and PMOS transistor, respectively. Thus, the on-resistance depends on the input voltage to the switch, or equivalently on the common mode voltage V_{CM}. This in turn, leads to different settling times of the spikes if the common mode is different in the spinning phases.

Each input of the preamplifier "sees" one switch switching on and one switch switching off at the transitions between the spinning phases. The voltage spikes of the input modulator due to charge-injection were extensively studied in chopper-amplifers [17]. The switching off of the switches leads to charge-injection of the accumulated charge in the switch. The complementary switch with the p- and n- transistors having the same surface reduces the charge injection to a certain extent. This is why the complementary switch is a preferred choice for the sensing switches.

We focus here on the steady-state error due to charge injection. Namely, the steady-state error due to the charge injection of the complementary switch leads to the change in the voltage gain and additional offset voltage [2]. The charge accumulated in the complementary switch exits the channel during switching off on the source and drain sides. The ratio of the two is a complex function of the source and drain impedances [53]. If the ideal case is assumed, where all the uncompensated charge of the complementary switch is deposited on the input preamplifier's capacitance, the inputs to the preamplifier after switching off can be written as [2]:

$$v^+(t) = (V_{CM} + V_H) \left(1 + \frac{2C_{ox} \left(WL\right)_{N,P}}{C_L}\right) - \frac{C_{ox} \left(WL\right)_{N,P}}{C_L} \left(V_{DD} - V_{THN} + \mid V_{THP} \mid\right), \quad (3.29)$$

47

$$v^-(t) = (V_{CM} - V_H) \left(1 + \frac{2C_{ox}(WL)_{N,P}}{C_L} \right) - \frac{C_{ox}(WL)_{N,P}}{C_L} (V_{DD} - V_{THN} + |V_{THP}|), \quad (3.30)$$

where $V_{\mathrm{CM}} + V_H$ and $V_{\mathrm{CM}} - V_H$ are the input voltages to the switches, $v^+(t)$ and $v^-(t)$ are the output voltages of the switches, C_{ox} is the oxide capacitance, C_{L} is the load capacitance, $(WL)_{\mathrm{N,P}}$ is the surface of the transistors, V_{DD} is the supply voltage, V_{THN} and V_{THP} are threshold voltages of the NMOS and PMOS transistors, respectively. In a rigorous model these values should be taken as an initial condition for the second spinning phase in the calculations in 3.1.1.

However, the voltage spikes at the preamplifier's inputs and the steady-state error due to the charge injection have the same polarity and almost equal amplitudes (except for the difference in the Hall voltage). Thus, they behave as the common mode disturbance and are almost cancelled out. The residual term of the steady-state error is proportional to the Hall voltage. It behaves as the offset voltage and can be filtered out:

$$v^+(t) - v^-(t) = 2V_H \left(1 + \frac{2C_{ox}(WL)_{N,P}}{C_L} \right) \qquad (3.31)$$

In the real case, the charge is not distributed equally between source and drain. In the case of a Hall device, this means that if both sensing switches see the same source impedance then the charge deposited on the input capacitance will be the same. In the ideal case, this is satisfied for the symmetric 4C horizontal Hall device. Nevertheless, the same does not hold even in the ideal case for the 5C vertical Hall device due to its two-fold symmetry, as discussed in Chapter 2.

The input stage of the preamplifier should be implemented either as a differential pair with symmetric active load or the folded-cascode topology in order to ensure equal input capacitances.

The different Hall voltages in the spinning phases also lead to different amplitude of the spikes. This is the case for the spinning current method where the Hall voltage is modulated to be an AC signal (traditional topology). This is also the case in 8CVHD where the Hall voltage amplitude is different in each main sensing step (see Chapter 2). The influence of the different Hall voltages is small, since the common mode voltage is much larger.

The nonidealities described above act simultaneously and give rise to the spikes waveform containing spikes of different amplitudes and settling times. Consequently, there are more spectral components than sketched in Fig. 3.5 for the ideal spikes waveform.

3.2 Design for high bandwidth in the Hall sensors based on the 8CVHD

Three solutions to spikes cancellation will be illustrated on three CMOS Hall sensors based on the 8CVHD. The sensors discussed are: the 2 dimensional (2D) magnetometer, the high speed angular

sensor and the open-loop current transducer. The limitations to the sensor's bandwidth imposed by the device and the preamplifier will be discussed. The limitations to the sensor's bandwidth stemming from the system topology will be discued in the respective chapters: Chapter 4 for the 2D magnetometer, Chapter 5 for the high speed angular sensor, and Chapter 6 for the open-loop current transducer.

3.2.1   Lumped model of the 8CVHD

The lumped model of the 8CVHD was developed for CAD simulators. The model relies on the lumped model of the horizontal Hall device presented in [3] and[54], as well as on the extension of this model for the vertical Hall devices [55] The capacitance between two contacts of the 8CVHD was calculated based on its dimensions and the characteristics of the technology. This capacitance was associated to a contact of the 8CVHD. The active region between the contacts of the 8CVHD was approximated by the measured resistance of the miniaturized 8CVHD. A more refined model would contain a junction-field effect transistor instead of a resistor. The purpose of the model was to estimate the amplitude and polarity of the voltage spikes and their influence on accuracy. To this end a simple resistance was sufficient. The simulated results based on this model were found to be in good agreement with the measurement results.

3.2.2   Hall voltage retrieval from the 8CVHD

The Hall voltage retrieval described below was used in all sensors based on the 8CVHD.

The retrieval of the Hall voltage from the 8CVHD is done in the eight main sensing steps, as discussed in Chapter 2. The geometry of the device and small number of contacts offer the possibility of the symmetric biasing, as discussed in Chapter 2.

The device is biased by the biasing current I_{bias}. In the first main sensing step, Fig. 3.7 left, the 8C device is biased such that the contacts 1 and 5 are at the high biasing potential, while the contacts 3 and 7 are at the low biasing potential. The remaining four contacts are used as the sensing contacts and the retrieved voltages $v_{86}=v_{24}$ are equal for the in-plane magnetic field. These two Hall voltages, being of the same polarity, can be summed on the electronics level, as shown below. In this way, for a given Hall voltage level we can bias the device at half the current, thus reducing nonlinearities of the 5C unit cell, and consequently its residual offset. The Hall voltage is obtained by rotating the biasing topology given in Fig. 3.7 by one contact clockwise until a full turn has been completed.

The Hall voltage retrieval in the eight main sensing steps proved efficient with the off-chip spinning. However, once implemented with the CMOS integrated signal retrieval and conditioning electronics it yielded a rather high value for the first harmonic (residual offset), on the order of several mTs. In order to reduce the residual offset, the four-phase spinning current method was
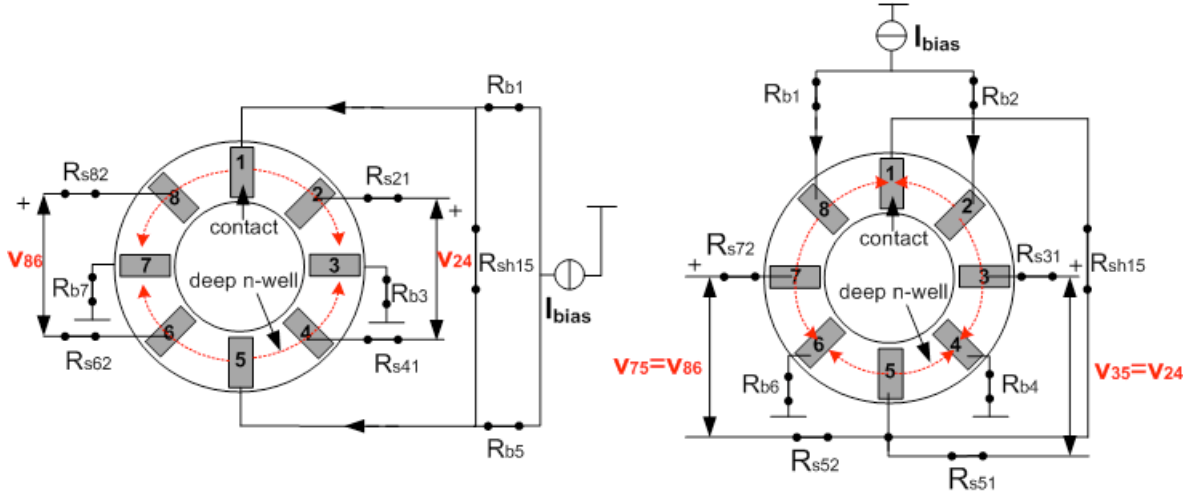
Figure 3.7: Hall voltage retrieval from the 8CVHD: left - the first main sensing step, right - the second sensing phase of the first main sensing step

added within each main sensing step [5]. Now each main sensing step contains four sensing phases that correspond to the four-phase spinning phases. The four-phase spinning current method is applied synchronously to the two π-curved 5C vertical Hall devices. The pair of the diametrically opposite contacts is connected through a low resistance switch, i.e., contacts 1 and 5 for the first and fifth main sensing steps, and so forth.

The addition of the low resistance shunt switch reduces the symmetry of the 8CVHD. Nevertheless, the symmetry of the spinning phases is much better for the π-curved 5C vertical Hall device than for any 5C vertical Hall device within an N-contact circular vertical Hall device. Namely, the difference in input (output) resistances between the spinning phases is smaller. The reason for this is again the biasing of the whole 8CVHD in all sensing phases. In an N-contact device there is an unwanted low current leakage in the two of the four phases of spinning. The shunt switch also increases the capacitances associated with the contacts it connects.

The second sensing phase of the first sensing step is shown in Fig. 3.7 right. The other two phases of the four-phase spinning current method are obtained by reversing the polarity of the biasing current as well as the polarity of the sensed voltages. The four-phase spinning is performed such that the Hall voltage is taken as a DC signal in subsequent sensing phases of the main sensing step. The offset consequently alternates sign and is an AC signal.

In total, there are 32 sensing phases whose duration is dictated by the clock frequency. The clock frequency is referred to as the sensing frequency. The frequency of one full turn around the device is referred to as the scanning frequency. The scanning frequency is 32 times smaller than the sensing frequency.

The scanning frequency of the CVHDs is equivalent to the spinning frequency in terms of its relation to the maximum sensor's bandwidth.

50

3.2.3 Solution 1: high capacitance of the input amplifier in the 2D Hall magnetometer

The first case $C_2 >> C_1$, depicted in 3.1, was implemented in the 2D magnetometer. The 8CVHD utilized in the 2D magnetometer has output resistance $R_1 = 1.8$ kΩ and an estimated capacitance $C_1 = 0.5$ pF. The complementary switches were designed small in order to minimize charge injection with W/L= 2/0.35 μm/μm. This in turn leads to a rather high switch on-resistance of $R_2 = 0.8$ kΩ that increases the input referred noise, as described in Chapter 4. The input capacitance of the preamplifier is $C_2 = 15$ pF. According to Eqn 3.18 the spikes' differential amplitude is reduced to about 4.6 % of the voltage drop on the Hall device. According to Eqn 3.19 the settling time of the spikes limits the maximum sensing frequency to 3.66 MHz, which in turn means that the maximum scanning frequency is 114 kHz. This allows the sensor's bandwidth up to around 60 kHz.

In Fig. 3.8 is given the simulated comparison of the spike's amplitude at the contacts of the 8CVHD and the preamplifier's inputs. Simulation results show reduction of the differential amplitude down to about 3 %. The small difference with respect to the calculations is due to slightly overestimated capacitance C_1.

In Fig. 3.9 is shown the simulated output of the 8CVHD amplified by the preamplifier. The polarity of the Hall voltage is reversed after half a period, while the polarity of the spikes remains unchanged over the scanning period. The spikes have the same polarity because the biasing of the device from the first half of the scanning period is repeated in the second half. The retrieval of the sensed Hall voltage is reversed. After demodulation of the 8CVHD's output voltage, the spike waveform is an odd function with zero DC value. In this way, there is ideally no contribution of the spinning spikes to the residual offset of the magnetometer even for a DC magnetic field. In addition, the spikes are at the sensing frequency while the useful Hall voltage is at the scanning frequency. Thus, there is frequency separation of the spectral components of the useful Hall signal and the spikes for both DC and AC magnetic fields (see also Fig. 3.11). This is the main distinguishing feature of the 8CVHD as compared to the Hall device and the traditional topology, as Fig. 3.6 shows. It is precisely this feature that allowed us to increase bandwidth while keeping satisfying accuracy.

However, due to the nonidealities discussed in 3.1.2, the DC value of the spikes waveform is nonzero. In Fig. 3.9 the spike's different amplitudes are attributed to the non-synchronized control clock signals. No care was taken either during the digital electronics design or on the layout level to synchronize the control signals for the switches.

3.2.4 Solution 2: partial guard band in the high speed angular sensor

The second solution to spikes cancellation relying on the partial guard band was implemented in the high speed angular sensor. The control signals for the sensing switches are delayed with respect
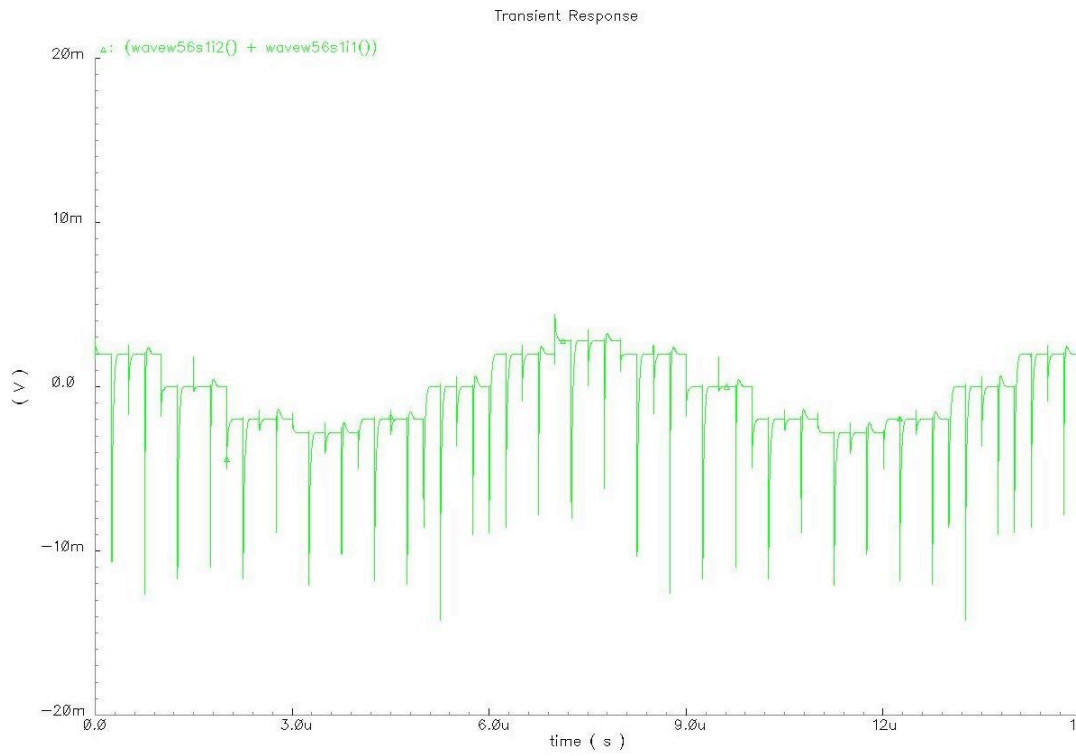
(a) Voltage spikes at the preamplifier's input
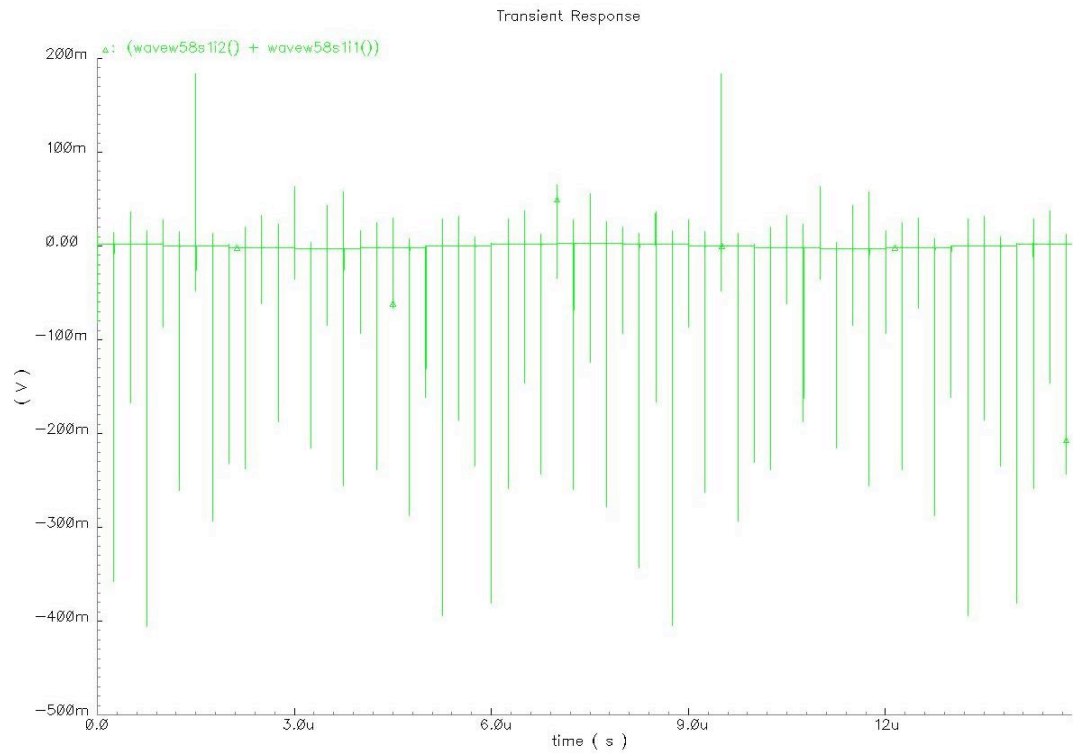
(b) Voltage spikes at the 8CVHD's contacts

Figure 3.8: Simulated voltage spikes for $I_{\mathrm{bias}}= 0.5$ mA , $f_{\mathrm{scan}}= 125$ kHz and the input capacitance $C_2 = 15$ pF $>> C_1 = 0.5$ pF
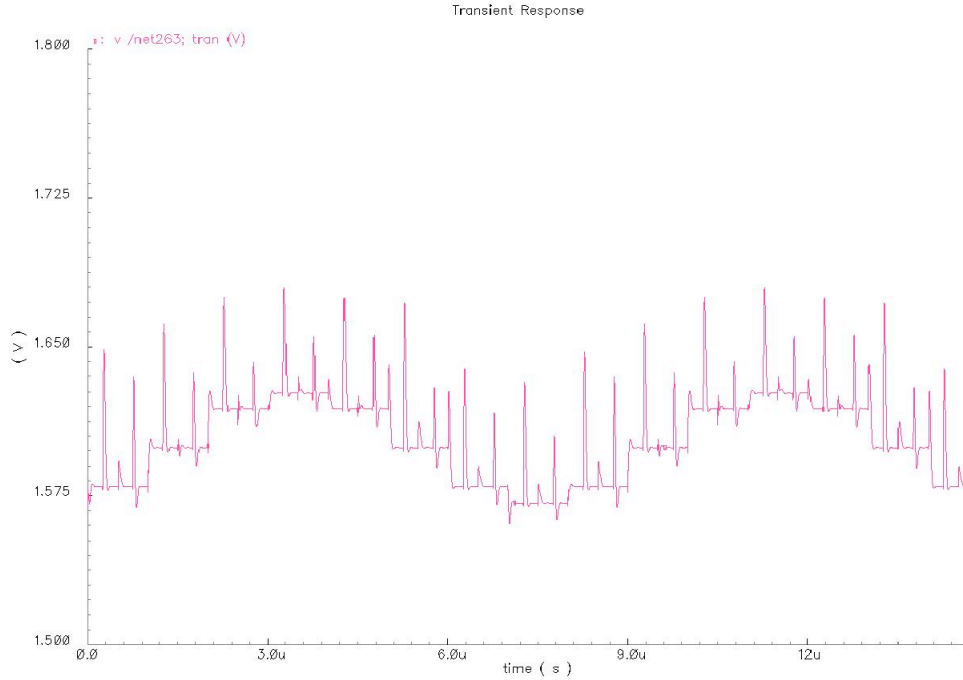
Figure 3.9: Simulated output of the preamplifier (gain 10) for I_bias= 0.5 mA , f_scan= 125 kHz and the offsetless 8CVHD. The spikes have the same polarity over one period. Their amplitudes vary due to non-synchronized switch control signals

to the biasing switches. In this way, the sensing contacts of the 8CVHD are connected to the preamplifier only after some time has elapsed from the beginning of the transient processes. During this time the accumulated charge is discharged through the Hall impedance, as discussed in 3.1.2. The end result is that the spikes in the output voltage of the 8CVHD "seen" by the input of the preamplifier have smaller amplitude.

During the delay time the inputs of the preamplifiers are left floating. In the ideal case, during this delay time the voltage at the preamplifier's inputs remains the same as in the previous phase. Nevertheless, there is an error voltage due to charge injection, as shown in Eqn 3.31. In addition to the offset voltage given by Eqn 3.31, there is an additional offset voltage due to the mild asymmetry of the contact capacitances of the π-curved 5C vertical Hall device.

The input capacitance of the preamplifier in this sensor is C_2=0.5 pF. According to Eqn 3.21 the approximate settling time of the spikes is about 13 ns. The delay time was chosen about a half of the settling time t_delay = 6 ns. The maximum sensing frequency set only by the front end is about 64 MHz. This would correspond to the scanning frequency of 2 MHz. It will be shown in Chapter 5 that the scanning frequency is limited to 1 MHz by the signal conditioning electronics. This is equivalent to about 500 kHz sensor's bandwidth.

The delay digital blocks were placed in front of each battery of switches as an additional digital module. This digital module was distributed around the device next to the sensing switches in the
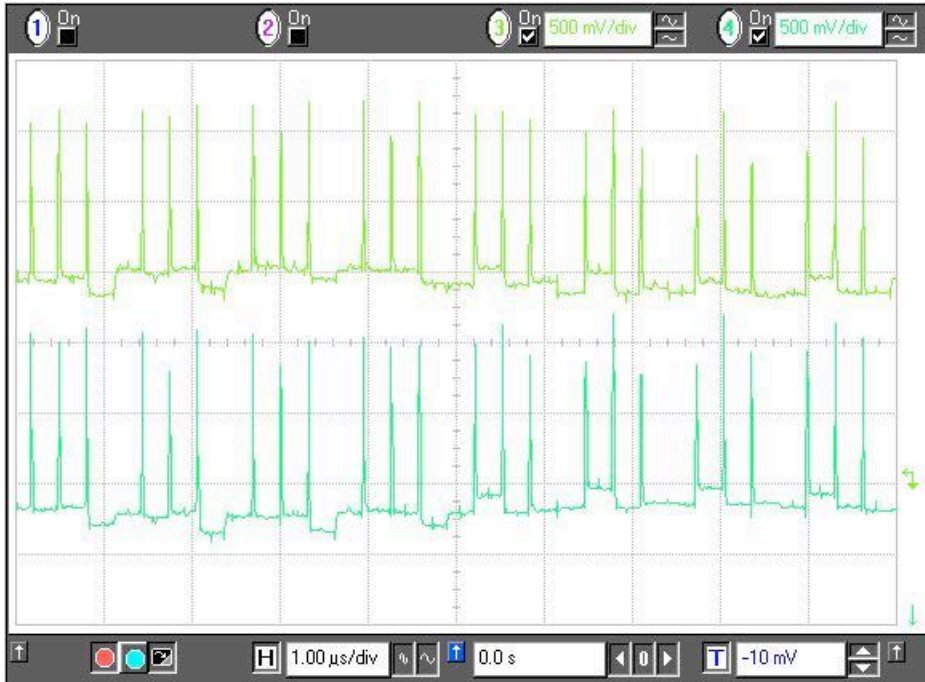
Figure 3.10: Measured voltage spikes waveform at the output of the preamplifier for two 8CVHDs. The scanning frequency is 100 kHz (sensing frequency 3.2 MHz), the magnetic field 50 mT and the biasing current 0.6 mA. The voltage spikes have the same polarity over the scanning period and their amplitudes are greatly reduced due to the partial guard band.

layout of the sensor. In this way the switch control signals are synchronized next to the sensing switches.

The measured spikes waveform at the output of the preamplifier is given in Fig. 3.10. Since the digital electronics was synchronized, the amplitudes of the spikes are more uniform as compared to those in Solution 1. The preamplifer was overdesign to allow for amplification of the spikes and their fast settling times. The average amplitude of spikes is 1.2 V at the output of the preamplifier. This is equivalent to about 30 mV amplitude of the voltage spike at one differential input of the preamplifier. The voltage drop on the device for R_{in}=0.9 kΩ and I_{bias}=0.6 mA is 540 mV. The expected voltage spike's amplitude at the input without the partial guard band is 270 mV according to Eqn 3.20. The partial guard band allowed for an order of magnitude reduction of the spike's amplitudes.

It can be seen in Fig. 3.10 that there is no voltage spike at the transitions from one main sensing phase to the next one. This is due to the fact that the sensing contacts remain unchanged for the last spinning phase of the *n-1*-th main sensing step and the first spinning phase of the *n*-th spinning phase. This leads to the spikes spectral components at the frequency eight times lower than the sensing frequency. The sketch of the frequency spectrum of the 8CVHD's signal and the voltage spikes is given in Fig. 3.11.
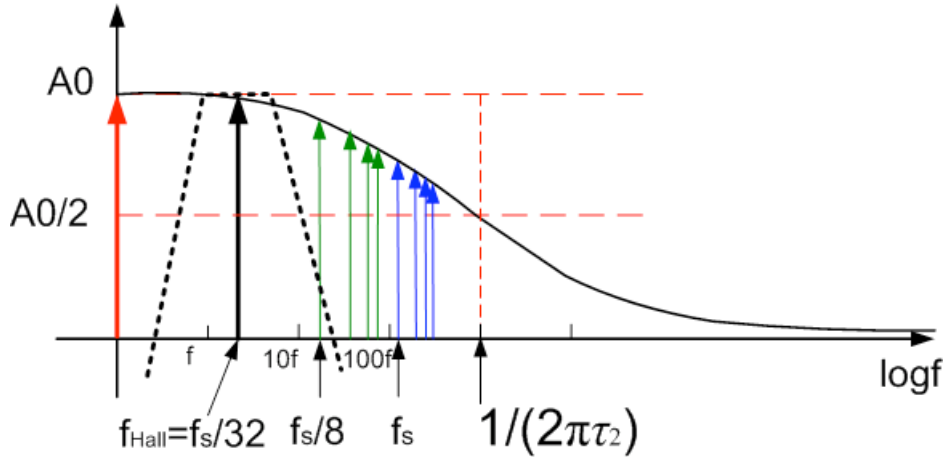
Figure 3.11: Sketch of the frequency spectrum of the voltage spikes and the 8CVHD's signal in the high speed magnetometer. The band pass filter is used to extract the first harmonic of the 8CVHD's signal

The first harmonic of the 8CVHD's signal at the scanning frequency and the voltage spikes at the sensing frequency are separated in the frequency domain. This enables good filtering of the spikes by the third or higher order bandpass filters, as sketched in Fig. 3.11. The high order filters should be used in order to ensure that the filtered amplitude of the voltage spikes is not greater than the useful Hall voltage. This is especially critical for low magnetic fields when the amplitude of the voltage spikes can be an order of magnitude greater than that of the Hall voltage.

3.2.5 Solution 3: two time shifted pairs of a clockwise and a counter-clockwise spun devices in the current transducer

The clockwise spinning is performed such that the biasing current is consecutively supplied to the contacts 1, 2, 3 and 4 in Fig. 3.1. The "plus" Hall voltage is taken from 2, 3, 4 and 1 contacts, respectively. The counterclockwise spinning is performed by supplying the biasing current to the contacts 1, 4, 3 and 2 in Fig. 3.1. The "plus" Hall voltage is taken from 2, 1, 4 and 3 contacts. The two voltages feature the Hall voltage of the same polarity but the spikes of the reversed polarity. The sum of these two voltages is free of spikes in the ideal case. In reality, the spikes cancellation with clockwise and counterclockwise spinning current method on the two devices is limited by the nonidealities described in 3.1.2.

The summing of the Hall voltages from the clockwise and counterclockwise devices can be done passively as in [52]. Another possibility is to use a differential difference amplifier [46]. The DDA has at least one differential signal input and one feedback input to define the gain. The main concern when designing a DDA is to ensure that the spike's amplitude is smaller than the linear input range of differential pairs. This concern applies to all cases treated in this chapter. This is important

in order to avoid saturation of the differential pairs. The saturation of the differential pair causes additional low frequency components and affects accuracy.

The front end of the current transducer consists of an array of four 8CVHDs divided in two pairs. Each pair consists of two 8CVHDs. The spinning current method is performed clockwise on the first device and counterclockwise on the second device. The novelty with respect to the previous solutions lies in time shifted spinning current on the two pairs. Namely, the first main sensing phase of the second pair is shifted by half the main sensing step with respect to the first main sensing step of the first pair. The cancellation by clockwise and counterclockwise spinning always yields a residual spike due to the nonidealities discussed above. These residual spikes are at least one order of magnitude smaller than the voltage spikes of one device. More importantly, their polarity is arbitrary. By the addition of the second pair, there are two residual spikes of the arbitrary polarity per one sensing phase. Thus, the influence on the useful signal becomes similar to that of noise. In the frequency domain these residual spikes can be approximated by the white noise.

On the other hand, the additional pair allows for lower biasing current of the 8CVHD. This in turn leads to higher signal-to-residual offset ratio for the array of the four devices. The outputs of the two pairs are summed by means of an eight-input DDA serving as a preamplifier. The preamplifier's input capacitance is $C_2 = 0.1$ pF. According to Eqn 3.22 the approximate settling time is about 6 ns, which poses the theoretical limit to the maximum sensing frequency of around 160 MHz. This would correspond to 5 MHz scanning frequency of the 8CVHD, or the maximum bandwidth of 2.5 MHz.

The so-called cross-spinning was performed on the 8CVHDs instead of the standard spinning described above. The cross-spinning keeps the same sensing contacts in the two spinning phases, i.e., the biasing current is consecutively supplied to the contacts 1, 3, 2 and 4 in Fig. 3.1. The "plus" Hall voltage is taken from 2, 4, 3, and 1 contacts, respectively. In this way, the number of voltage spikes is reduced from four to two per period. The clockwise and counterclockwise cross-spinning for the two main sensing steps of the 8CVHD are illustrated in Fig. 3.12. Similarly to the Solution 2, the switch control signals were synchronized in the additional digital block placed next to the switches in the layout.

The simulated output of the eight-input DDA is shown in Fig 3.13.

3.3   Conclusions

In this chapter was given the general study of the voltage spikes for the horizontal Hall device due to the spinning current method. Three solutions to tackling the challenge of increasing the spinning frequency while maintaining the accuracy in the sensors based on the 8CVHD were presented.

The first one is a novel solution relying on the high input capacitance of the preamplifier which together with the sensing switch on-resistance filters out the voltage spikes. It is based on only
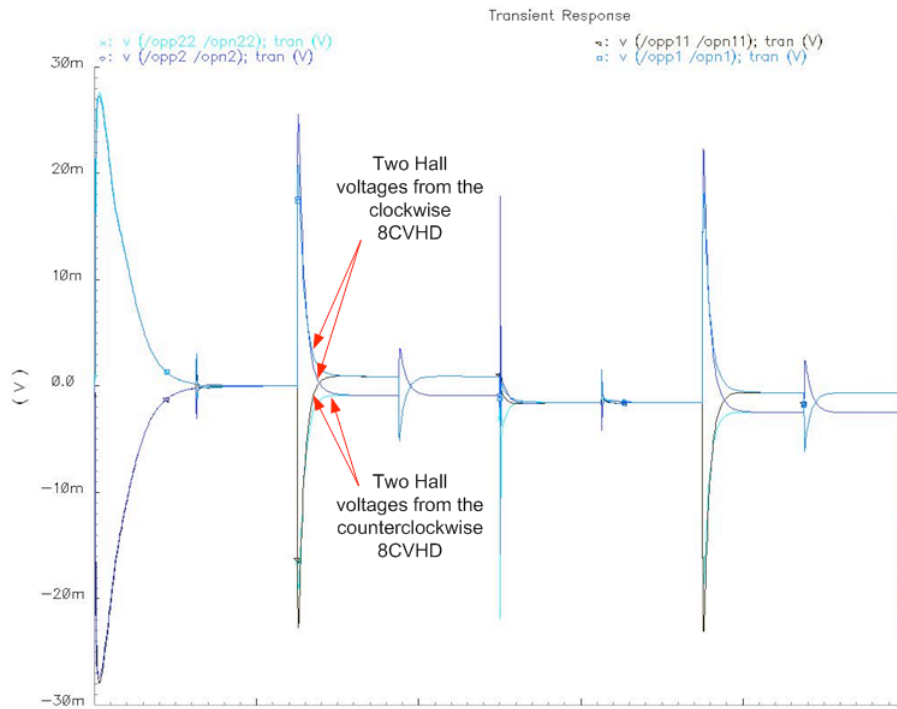
Figure 3.12: Illustration of the first two main sensing steps of the clockwise and counterclockwise spinning on the two 8CVHDs
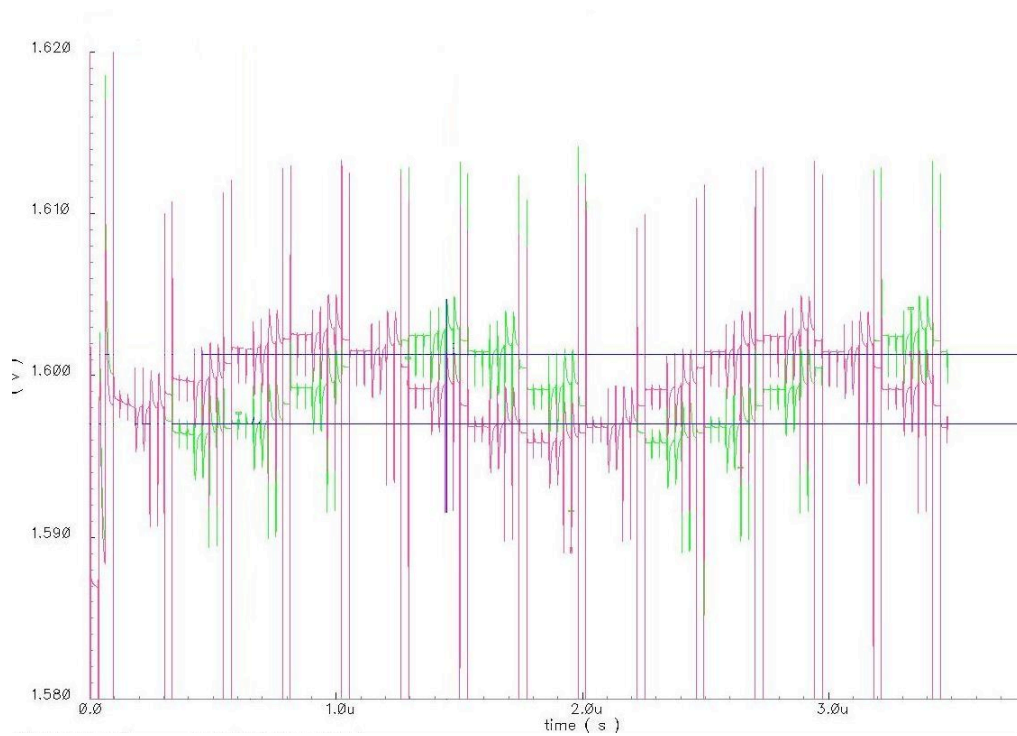
Figure 3.13: Simulated output of the DDA (gain 10) for the clockwise and counterclockwise 8CVHDs (I_{bias}= 0.5 mA, f_{scan}= 500 kHz and B= 10 mT in the ideal case of the offsetless 8CVHD and synchronized control signals). The maximum amplitude of the amplified spikes is 10 mV.

one Hall device. It does not require either device matching or big chip surface. However, it limits the scanning frequency to several hundreds of kHz at best, supposing the input capacitance were reduced to about ten times less than the capacitance of a Hall device. This enables the sensor's bandwidth of about 100 kHz, which is the state-of-the-art of majority of Hall effect sensors available on the market today.

The second solution examines the partial guard band to remove a part of the spike's energy without compromising a high spinning frequency. This solution allows for the bandwidth increase while still utilizing only one device. The achievable bandwidth determined only by the front end is about 500 kHz. The frequency separation of the useful Hall voltage and the spectral components of the voltage spikes allows for efficient filtering of the voltage spikes. Nevertheless, it requires at least 3rd order bandpass filtering to remove the voltage spikes.

In both the first and second solutions the voltage spike's waveform shows strong temperature cross sensitivity. This is due to the drift of the Hall and switch on-resistance.

The third solution is based on the cancellation of the voltage spikes by the clockwise and counterclockwise spinning current method on two devices. The novelty with respect to previous solutions lies in the additional pair of the clockwise and counterclockwise devices. The spinning current method is applied with a time shift on the second pair of the devices. The outcome is that the residual spikes are of arbitrary amplitude due to mismatches. They are distributed over the sensing phase and behave like noise. The theoretical limit for the maximum sensor's bandwidth set only by the characteristics of the front end is 2.5 MHz.

This solution, like all differential solutions, offers immunity against temperature cross sensitivity and other disturbances providing the devices are matched. It consumes more chip surface and requires careful layout to match the devices. More importantly, as any array, it offers the best signal-to-residual offset ratio of all the three solutions for the same power consumed.

The ratio of the Hall signal-voltage spikes stays the same for the first two solutions when increasing the biasing current of the 8CVHD. This is due to the linear dependence of the Hall signal and the voltage spikes on the biasing current. This is not the case for the third solution where the ratio of the Hall voltage and the residual spikes increases with the increase of the biasing current.

Chapter 4

Two-dimensional magnetometer based on the 8CVHD

This chapter depicts a two-dimensional (2D) CMOS magnetometer based on the 8CVHD. The 8CVHD's features enable a novel system level topology for a 2D magnetometer. The novel system level concept allows for the common biasing, Hall voltage retrieval, offset cancellation, and front end signal conditioning electronics for the two in-plane components of the magnetic field. This leads to good matching of the output signals proportional to two dimensions of the magnetic field. The explanation of the novel concept is followed by the measured characteristics of the CMOS implementation.

4.1   Principle of operation

Two-axis magnetometers for measuring in-plane magnetic field in CMOS technology usually have two vertical Hall devices placed orthogonally, with or without a common central contact [56], [23]. The retrieval of the Hall voltages together with dynamic offset cancellation techniques is done independently for the two devices. The same holds for the subsequent signal conditioning electronics. This approach poses stringent requirements on matching of both signal retrieval and conditioning electronics for the two axes. There is a possibility to have only one signal conditioning chain but this requires time multiplexing of the two signals, which reduces system's bandwidth.

The use of the 8CVHD as a sensing device opens up the way to an alternative system level topology for the 2D magnetometer [57]. The output voltage of the 8CVHD is an eight step sine wave whose period is determined by the scanning time and number of contacts, and the amplitude is proportional to the magnitude of the applied in-plane magnetic field. The output of the 8CVHD can be bandpass filtered to obtain a smooth sinusoid whose phase is proportional to the angle of the magnetic field with respect to a reference axis. An alternative to bandpass filtering would be signal conditioning so as to obtain the orthogonal components of the applied magnetic field. This can be
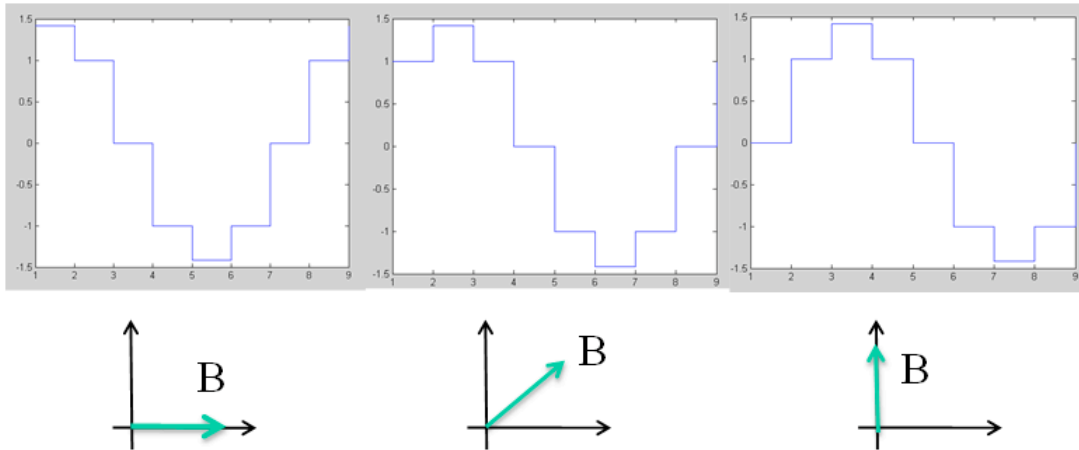
Figure 4.1: 8CVHD output for the in-plane magnetic field vector. The 8CVHD's output can be seen as the sampled cosine wave (left) and sine wave (right) in eight time intervals

done by applying the 8CVHD's output to two phase sensitive detectors controlled by orthogonal clock signals, or equivalently to a quadrature demodulator.

It should be noted that in this system topology the two magnetic field components have in common: 1) biasing, 2) signal retrieval, 3) application of spinning current method for dynamic cancellation of the offset and low frequency noise of the Hall device, and 4) front-end signal conditioning electronics. The separation of the two channels is postponed to the point where signal levels are high and less susceptible to nonidealities and mismatches of signal conditioning electronics.

4.1.1   8CVHD in the 2D magnetometer

The magnetic field sensing device is the miniaturized 8CVHD depicted in Chapter 2. The retrieval of the Hall voltage was described in Chapter 3. The first case where the input capacitance of the preamplifier is much larger than the input capacitance of the Hall device, $C_2 >> C_1$, was utilized in the 2D magnetometer. The 8CVHD has the output resistance R_1= 1.8 kΩ and an estimated capacitance C_1= 0.5 pF. The complementary switches were designed small in order to minimize charge injection (W/L= 2/0.35 μm/μm). This in turn leads to a rather high switch on-resistance of R_2= 0.8 kΩ that increases the input referred noise. The input capacitance of the preamplifier is C_2= 15 pF. According to Eqn 3.18 the spike's differential amplitude is reduced to about 4.6 % of the voltage drop on the Hall device. According to Eqn 3.19 the settling time of the spikes limits the maximum sensing frequency to 3.66 MHz, which in turn means that the maximum scanning frequency is 114 kHz. This allows the sensor's bandwidth up to around 60 kHz.

The output of the 8CVHD for the magnetic field rotating in the chip plane is a step cosine wave shown in Fig. 4.1.

As can be seen in Fig. 4.1, the response of the device to the applied magnetic field in the direction of the x-axis is a step cosine wave. Similarly, the response of the device to an applied

magnetic field in the direction of the y-axis is a step sine wave. Finally, the response of the device to an in-plane magnetic field vector is a linear combination of a step sine and a step cosine wave containing information on respective orthogonal components. In the case of an infinite number of contacts the output of a CVHD is given by:

$$V_{CVHD} = S_I I_{bias} B \cos(2\pi f_{scan} t - \alpha) =$$

$$= S_I I_{bias} B \cos\alpha \cos(2\pi f_{scan} t) + S_I I_{bias} B \sin\alpha \sin(2\pi f_{scan} t) =$$

$$= S_I I_{bias} B_x \cos(2\pi f_{scan} t) + S_I I_{bias} B_y \sin(2\pi f_{scan} t). \tag{4.1}$$

where S_I is the current-related sensitivity of the 5C unit cell, I_{bias} is the biasing current of the 5C unit cell, B is the magnitude of the in-plane magnetic induction vector, $B_x = B\cos\alpha$ and $B_y = B\sin\alpha$ are orthogonal projections of the magnetic induction vector, f_{scan} is the scanning frequency, and the angle α is the angle included between the magnetic induction vector and the reference axis of the device.

To measure the angle between an in-plane magnetic field and a reference axis, we would band-pass filter the output of the 8CVHD to obtain a smooth sine wave with a precisely defined phase. However, we are interested in the magnitude of the orthogonal components. To this end, the step sine wave contains the necessary and sufficient information. As Eqn 4.1 shows, the components of the magnetic field, B_x and B_y, can be obtained by the phase-sensitive detection, or equivalently quadrature demodulation, of the CVHD's output voltage V_{CVHD}, respectively:

$$V_x = V_{CVHD} \cos(2\pi f_{scan} t), \tag{4.2}$$

$$V_y = V_{CVHD} \sin(2\pi f_{scan} t). \tag{4.3}$$

After low pass filtering, the outputs of the magnetometer are given by:

$$V_x = 0.5 S_I I_{bias} B_x, \tag{4.4}$$

$$V_y = 0.5 S_I I_{bias} B_y. \tag{4.5}$$
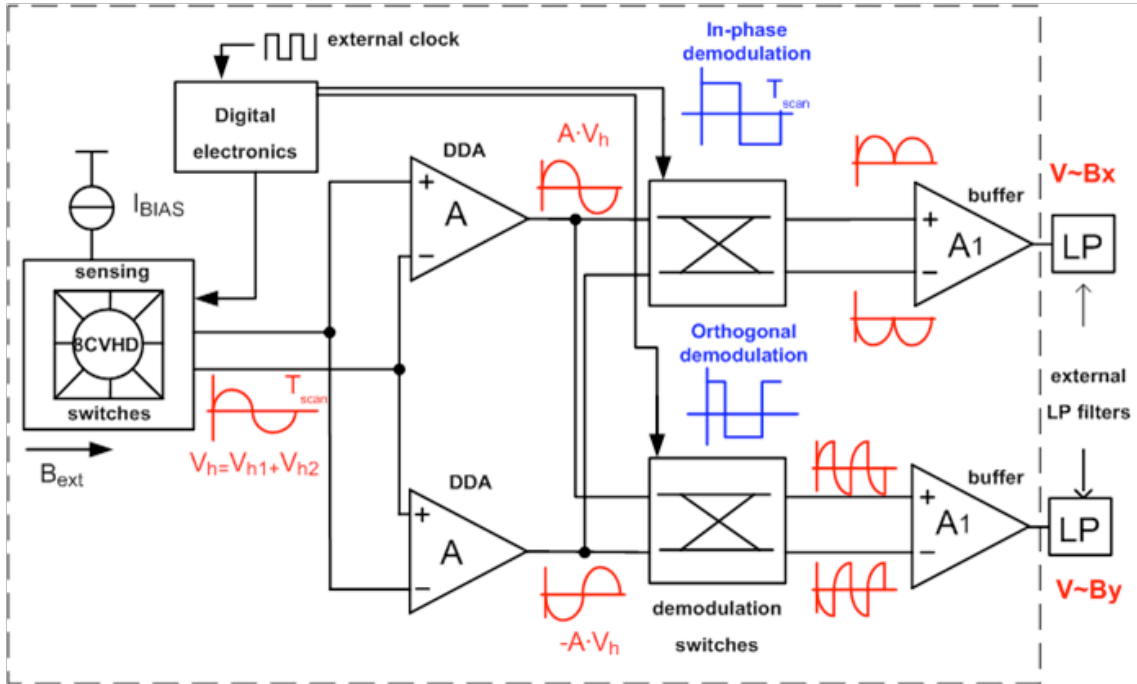
Figure 4.2: Block diagram of the 2D magnetometer

4.1.2 Block-diagram of the 2D magnetometer

The block-diagram of the 2D magnetometer is shown in Fig. 4.2. The two Hall voltages from the opposite sides of the device have the same polarity. They are summed by means of the two-input differential difference amplifier (DDA) serving as the preamplifier of the system. Special care was taken to optimize the DDA for low offset voltage and input referred noise. The integrated digital electronics module, with off-chip clock signal, delivers control signals for switches for Hall voltage retrieval. Each contact of the 8CVHD is through switches connected to a biasing current source, ground or one of the two inputs of the DDA. The two preamplifiers deliver a differential signal to the input of the demodulation blocks. The demodulation blocks together with the buffers and low pass filters form simple phase detectors. The demodulation blocks are realized as simple switches.

Due to the limited resolution of the Hall voltage sensing, or equivalently to a finite number of contacts, there is an intrinsic phase shift of the output signal with respect to the beginning of the first main sensing step. This intrinsic phase shift should not be mistaken for the phase shift that corresponds to the angle between the in-plane field and the reference coordinate axis. The intrinsic phase shift was found to be π/N for the contact topologies including contacts aligned with the coordinate axes, as is the case with the miniaturized CVHD. For the 8CVHD, the intrinsic phase shift is $\pi/8$, or equivalently half of the main sensing step. This is why the "in-phase" signal for phase detection is shifted by half of the main sensing step.

The demodulation switches are controlled by the "in phase" signal shifted by half the main sensing

Input CM range	0.6 V – 1.7 V
DC gain	60 dB
Common-mode rejection ratio (CMRR)	60 dB
Feedback resistors	R1= 500 Ω, R2= 4500 Ω
Closed-loop gain	9.9
GBW (two differential inputs)	50 MHz
Input-referred white noise	7.6 nV/$\sqrt{\text{Hz}}$
Input referred offset ($\pm$ 3σ)	$\pm$ 1.5 mV
Current consumption	1.38 mA

Table 4.1: Simulated characteristics of the preamplifier

step with respect to the 8CVHD's output signal, and the signal orthogonal to the "in-phase" signal. The two control signals are also supplied by the integrated digital electronics module. The channel controlled by the "in-phase" (orthogonal) control signal delivers the component in the direction of the x-axis (y-axis).

The outputs of the demodulation blocks are brought to the buffers which transform the differential signal into a single ended one. Low-pass filtering of the demodulated signals was done by off-chip filters.

4.2 Signal conditioning electronics

The biasing current of the Hall device was set by a variable resistor connected in series with a diode connected PMOS of an on-chip current mirror. The contacts of the 8CVHD are through a battery of six complementary switches connected to: biasing current source, ground (two biasing switches), and to positive or negative inputs of the two signal inputs of the DDA (four sensing switches). The diametrically opposite contacts are connected through a low resistance switch to perform the four-phase spinning current method, as described in Chapter 3.

The digital electronics module with off-chip clock generator controls switches. Both schematics and layout of the digital module were automatically synthesized after a VHDL code in the commercially available software. No care was taken during the design to synchronize the switch control signals at the output of the digital module. This is reflected in the different height of the spikes as was shown in Fig. 3.9 for a high biasing current.

The two Hall voltages taken from the 8CVHD in each sensing phase are summed by means of the two-input DDA. It contains two signal inputs and one feedback input. The schematics of the two-input DDA is given in Fig. 4.3 a).

The block diagram of the DDA in the closed loop is given in Fig. 4.3 b). Its output is given by:

$$V_{pre} = V_{REF} + (V_{h1} + V_{h2})\frac{R_1 + R_2}{R_1} \tag{4.6}$$

The simulated characteristics of the preamplifier are given in Table 4.1.

The buffer was realized as one-input DDA. Its simulated characteristics are given in Table 4.2.

63
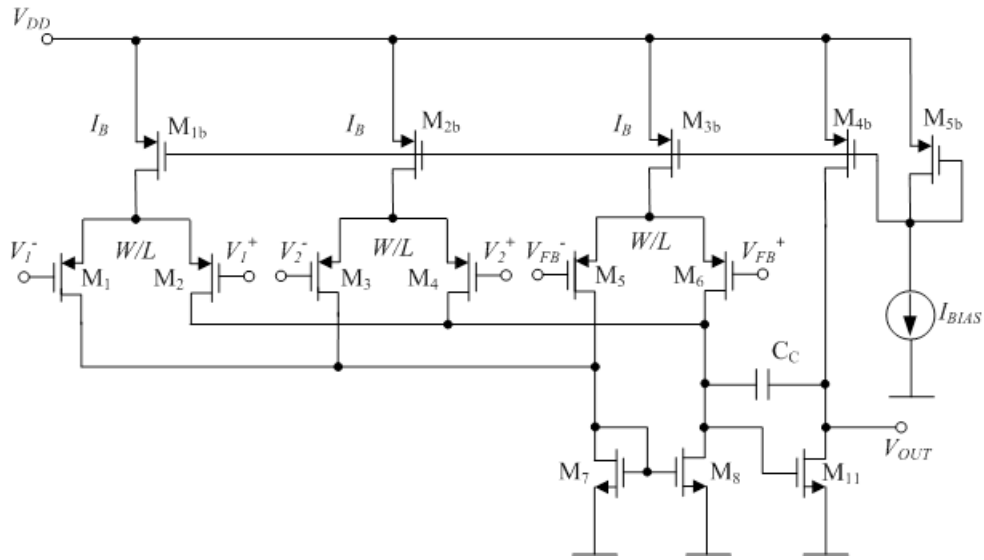
(a) Schematics of two-input DDA
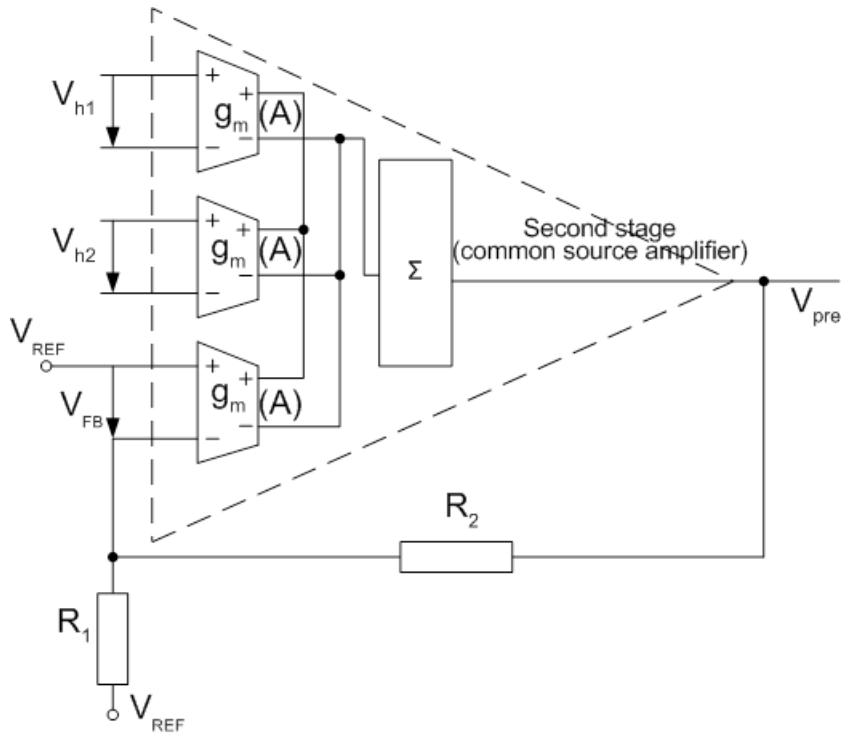
(b) Block-diagram of the DDA in the closed-loop configuration

Figure 4.3: Preamplifier of the 2D magnetometer

Output swing (V_{REF}= 1.2-1.3 V)	± 0.8 V
DC gain	77 dB
Feedback resistors	R1= 4500 Ω, R2= 4500 Ω
Closed loop gain	1.99
GBW	16 MHz
Phase margin for 100 kΩ in parallel to 25 pF	52 º
Input-referred white noise	19 nV/$\sqrt{\text{Hz}}$
Input referred offset (± 3σ)	± 5 mV
Current consumption	1.58 mA

Table 4.2: Simulated characteristics of the buffer
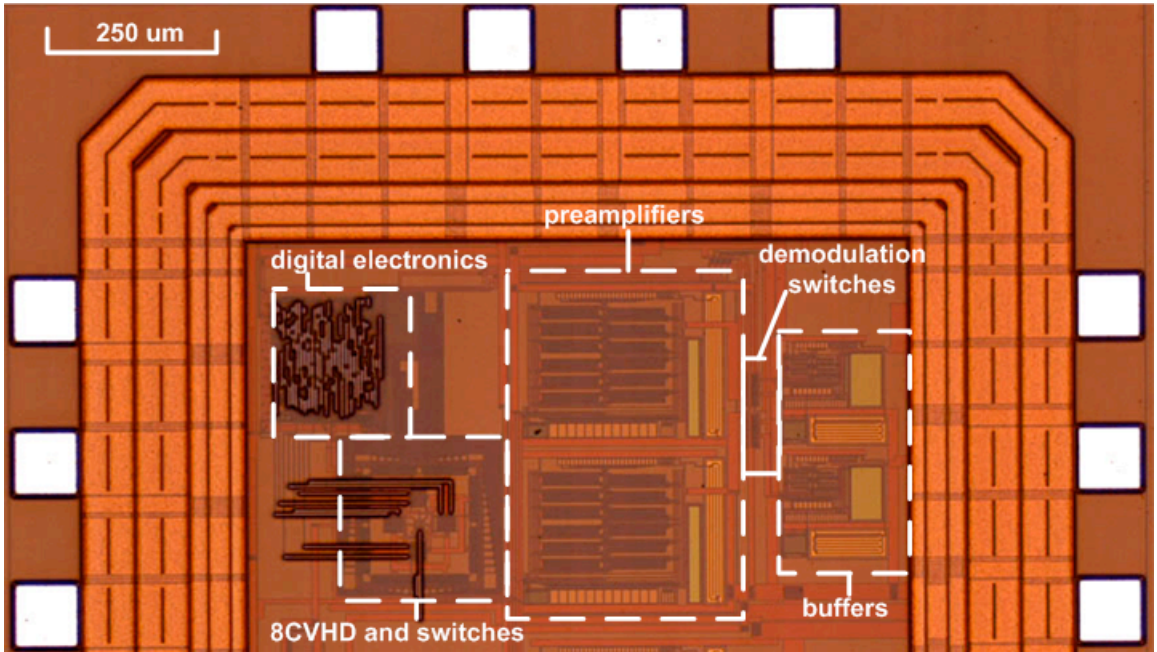
Figure 4.4: Microphotograph of the 2D magnetometer

4.3 Measurement results

The 2D magnetometer was realized in 0.35 μm high voltage CMOS technology. The high voltage technology was chosen because of the deep N-well that used as an active region enhances performance of the 8CVHD. The microphotograph is given in Fig. 4.4.

In Fig. 4.5 are given demodulated signals at the output of the buffers before low pass filtering by the off-chip filters. The cut off frequency of the off-chip low pass filters used in measurements was 3 Hz, except for the noise measurements where it was 50 kHz.

The average magnetic sensitivity of the 8CVHD is 30 V/(AT) (the average of the waveform shown in Fig. 3), while the amplification of the preamplifiers and buffers is about 40. The current-related sensitivity of the magnetometer is 1100 V/(AT). The average absolute sensitivity of the magnetometer is 0.22 V/T for the Hall biasing current I_{bias}= 0.2 mA. The sensitivities of the
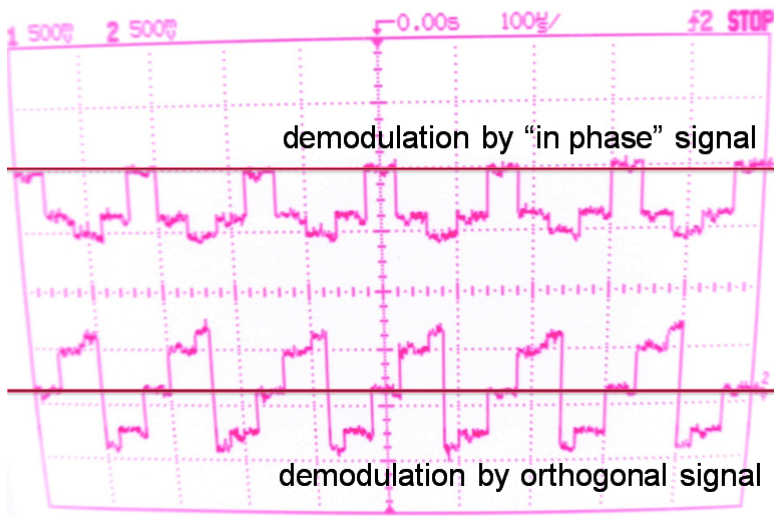
Figure 4.5: Demodulated signals at outputs of the 2D magnetometer (I_{bias}= 0.5 mA, B_{x}= 400 mT, and f_{scan}= 3.125 kHz). Front end design discussed above yields the measured signal without voltage spikes

channels are almost identical. The channels' linearity was recorded for the magnetic field swept in the range 0-1.5 T. It was found to be 1.3 % full scale (FS) on average.

The offset voltage of the preamplifiers is removed on the system level by the chopper principle as explained in Chapter 1. This does not hold for the offset voltage of the buffers. Consequently, the offset voltage of the buffers dominates in the offset voltage of the magnetometer. In order to examine the influence of the 8CVHD's residual offset voltage, the buffer's offset was externally compensated.

The residual offset of the channels was measured for Hall biasing currents in the range 0.1-0.3 mA and f_{scan} = 33 kHz. The average value of the input referred residual offset was found to be 200 μT.

Similarly to the offset of the 8CVHD, 1/f noise is averaged out both over one main sensing step and over the period of the output waveform. The measured input referred noise of the magnetometer is 23 nV/√Hz at 10 Hz, 18 nV/√Hz at 100 Hz, and 15 nV/√Hz in the white noise region. The calculated white noise of the 8CVHD's output resistance is about 7 nV/√Hz. The input referred noise of the preamplifier is 7.6 nV/√Hz, while the noise of the two sensing switches is about 5.6 nV/√Hz. The input referred noise voltage spectral density for f_{scan} = 33 kHz and I_{bias}= 0.2 mA is given in Fig. 4.7.

The input referred magnetic field equivalent noise was obtained by dividing the input referred noise by the biasing current and sensitivity of the Hall device. The spectral density of this noise is 2.6 μT /√Hz. The RMS integrated noise, which is a figure of merit for measuring AC magnetic fields, is about 300 μT in the frequency range 1 Hz−30 kHz.

In Fig. 4.8 are given the magnetometer's outputs, $B_{\text{x}} = B \cos \alpha$ and $B_{\text{y}} = B \sin \alpha$, after low-pass filtering as a function of the angle between the magnetic field and the reference axis.

66
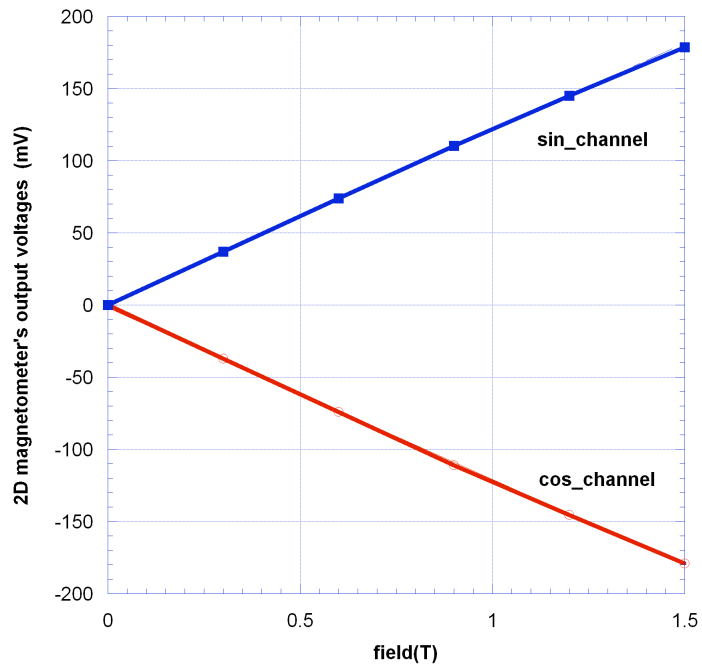
Figure 4.6: Channels linearity for I_{bias}= 0.1 mA and f_{scan}= 31.25 kHz
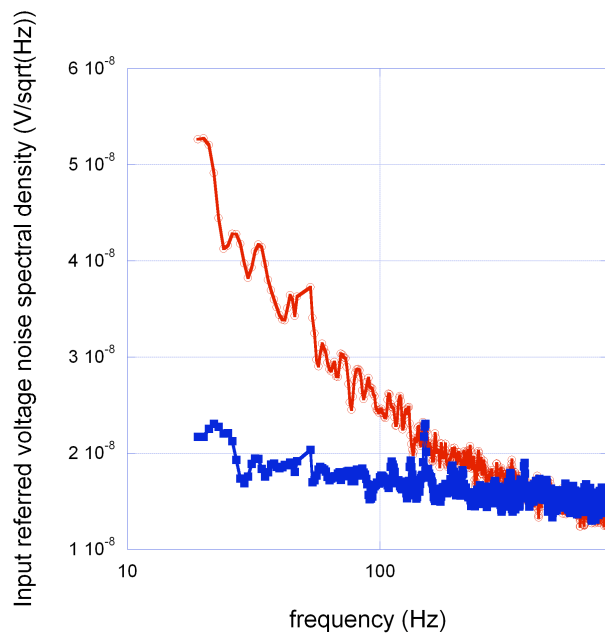
Figure 4.7: Input referred noise voltage spectral density of the magnetometer: top curve - after preamplifier, bottom curve - at the output of the magnetometer after phase sensitive detection. 1/f noise of both Hall device and preamplifier is suppressed on the system level.
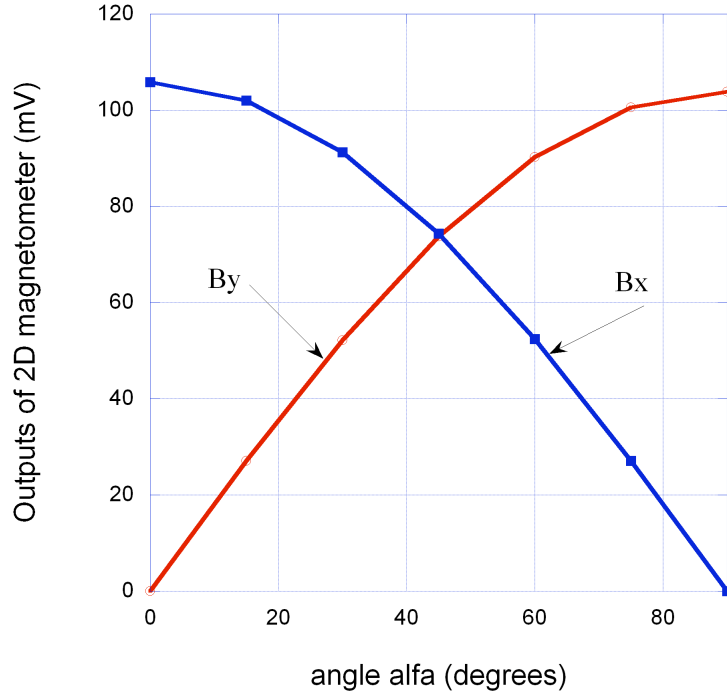
Figure 4.8: B_x and B_y after low pass filtering as a function of the angle between the magnetic field and the reference axis ($\mathbf{B}$= 400 mT, I_{bias}= 0.2 mA, the angle span 0-90º, and f_{scan} = 31.25 kHz)

The temperature coefficient of the magnetometer's offset drift in the temperature range -20 − 85 °C is 27 µV/°C for f_{scan} = 31.25 kHz and I_{bias}= 0.2 mA. The offset drift of the buffers dominates in the offset drift of the magnetometer. The characteristics of the 2D magnetometer are summarized in Table 4.3.

4.4 Conclusions

The novel system level concept for the 2D CMOS integrated magnetometer based on the 8CVHD enables common biasing, signal retrieval, dynamic cancellation of offset and low frequency noise, and front-end signal conditioning electronics for both components of the measured in-plane magnetic field

Technology	AMS 0.35 µm
Current related sensitivity	1100 V/(AT)
Average channels nonlinearity 0-1.5 T	1.3 %
Input referred noise (I_{bias}= 0.2 mA, f_{scan} = 33 kHz)	(15 nV/√Hz) 2.6 µT/√Hz
Average residual offset I_{bias}= 0.1 − 0.3 mA buffer's offset compensated buffer's offset noncompensated	200 µT 10 mV
Offset drift (-20 − 85 ºC, I_{bias}= 0.2 mA)	27 µV/ºC
Bandwidth	60 kHz
Power consumption	20 mW

Table 4.3: Summary of characteristics of 2D magnetometer

vector. The separation of two channels is postponed to the point where signal levels are high and less susceptible to nonidealities and mismatches of signal conditioning electronics. The Hall voltage retrieval from the 8CVHD and the design of the front end allowed efficient removal of the voltage spikes. The magnetometer features bandwidth of around 60 kHz, wide dynamic range 0-1.5 T, high spatial resolution, and a high measurement resolution of 300 µT over wide frequency range 0-30 kHz. The 2D magnetometer can also be used as an angular sensor with full measurement range.

Chapter 5

High speed magnetic angle sensor based on the 8CVHD

In this chapter we describe a CMOS integrated magnetic angle sensor based on the 8CVHD. The novel concept of the sensor is based on two eight contact circular vertical Hall devices (8CVHD). The small number of contacts allows for faster Hall voltage retrieval from the device. The outputs of the 8CVHDs are separately processed in two channels and act as mutual references. The Hall voltage retrieval is done in the clockwise direction for the first device, and in the counterclockwise direction for the second one. In this way there is no need for the reference signal as in [31, 32]. The output of the sensor is a pulse width modulated (PWM) signal whose width is proportional to twice the angle enclosed between the in-plane magnetic induction vector and the reference axis. The information on the angle is directly present in the pulse width modulated signal. The use of two devices doubles the angular sensitivity of the sensor. The devices, the interface electronics, and the signal conditioning electronics were designed and optimized to allow detection of high speed in-plane rotating vectors. Due to the system level concept of the sensor, the angle measurement is insensitive to temperature drift of the sensitivity of the 8CVHDs to the first approximation. The system level concept of the sensor also greatly reduces the influence of the temperature drift of the signal conditioning electronics on the measured angle.

5.1   State-of-the-art in magnetic angular sensors

Existing angular position sensors were developed for use in mechanical systems for angular position sensing. A magnetic angular position sensor consists of a magnetic direction sensor integrated on a chip and a rotating magnet mounted on a shaft. The magnetic sensors applied in magnetic angular sensors can be Hall devices: horizontal Hall devices [58], combination of horizontal Hall devices with integrated magnetic concentrators (IMCs) [25, 59] or vertical Hall devices [56, 60, 61, 62]. Beside Hall devices, ferromagnetic magneto-resistors, i.e., anisotropic magneto-resistors (AMRs) [63] and giant magneto-resistors (GMRs) [64] are used in magnetic angular sensors. The magnetic angular

sensors based on magnetic field effect transistors (MAGFETs) [65, 66] and recently investigated magnetic tunnel junctions [67] were also reported. Hall devices and MAGFETs are compatible with low cost CMOS technologies. In all above mentioned angular sensors based on Hall devices, the angle is determined by measuring the orthogonal components of the magnetic induction vector and then computing the arctg function. In [31] was first reported a magnetic angular position sensor based on the novel circular vertical Hall device (CVHD). The output of the sensor contains the information on the angle without either need for the arctg function or complicated detection algorithms. The above mentioned sensors feature a full measurement range. The best performances have the sensors based on the combination of horizontal Hall devices and IMC, though IMC requires a post- CMOS fabrication step, as well as the sensors based on vertical Hall devices. They provide absolute accuracy 0.1° over the full measurement range. The magnetic angular position sensors based on ferromagnetic resistors [63, 64] are very accurate but they cannot be fully integrated in low cost CMOS technologies. Magnetic angular position sensors based on MAGFETs are great candidates for low power magnetic angular position sensors in sub-micron CMOS technologies [65]. The MAGFETs are sensitive to perpendicular component of the rotating magnet's field. The extraction of the measured angle requires dedicated algorithms as in [66]. Typical applications of angular position sensors are: contactless potentiometer, valve position sensor, single- and two-axis joysticks, motor shaft encoder, etc. The maximum rotation speeds in these applications do not exceed a few thousands rad/s. As a consequence, the required sensor's bandwidth is low. However, there are applications where a high sensor's bandwidth is or will be required such as: high performance hard disc drives rotate at 15 000 rpm, the fastest gas turbine engines reach 165 000 rpm, electromechanical batteries can reach 200 000 rpm [68], to mention but a few. Furthermore, a need for high-speed angular position sensors has arisen in current transducers [69]. Recently, high speed angular position sensing was needed in micro-rheometers dedicated to glucose sensing applications [70]. A low power CMOS angular position sensor based on sixty-four contact CVHD was developed for this purpose [32]. The maximum rotation speed for 8-bit accuracy tracked by the sensor is around 11 000 rpm. The highest bandwidth of the magnetic angle sensors mentioned above was reported in [61]. However, the sensor is not fully CMOS integrated.

5.2 High speed magnetic angle sensor with one 8CVHD per channel

5.2.1 Sensor's concept

The sensing device employed in the sensor is the miniaturized 8CVHD described in Chapter 2. The Hall voltage retrieval described in Chapters 2 and 3 involves rotation of the sensing and biasing contacts by one contact in the clockwise direction. It can be interpreted as the rotation of the sensitivity axis of the device by the angle between the contacts, as illustrated in Fig. 5.1.
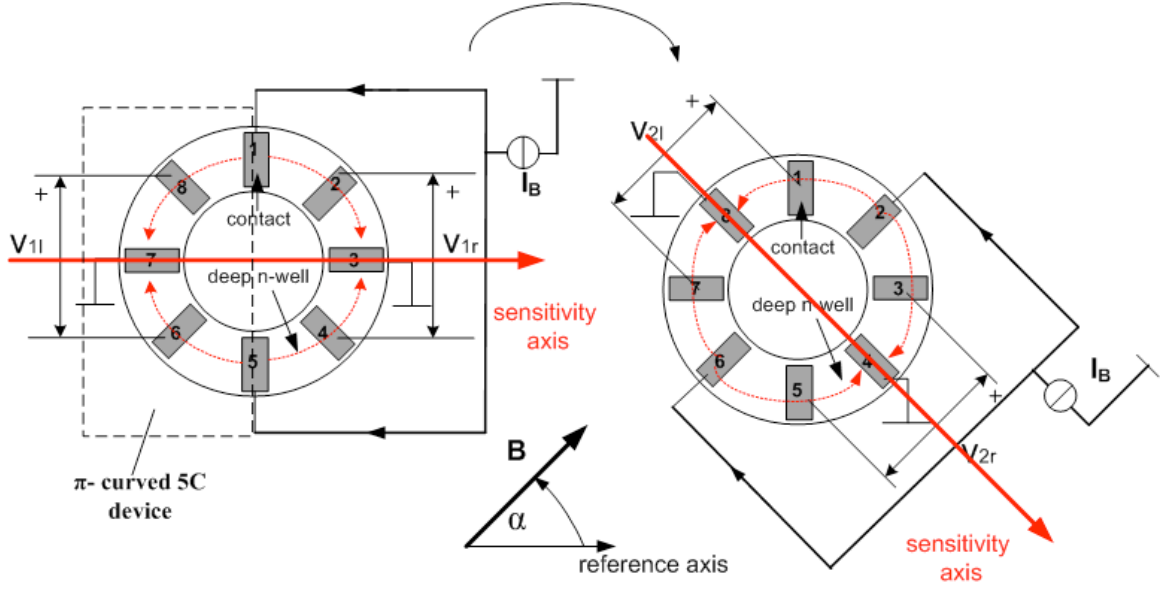
Figure 5.1: Sensitivity axis of the device rotates in main sensing steps: left - first main sensing step, right - second main sensing step

The angular velocity of the sensitivity axis is proportional to the scanning frequency. In the case of large number of contacts the sensitivity vector of the CVHD (with respect to the reference axis in Fig. 5.1) can be approximated by:

$$S_c = S_0 e^{-j2\pi f_{scan}t}, \tag{5.1}$$

where S_0 is the maximum sensitivity of the device when the sensitivity axis and the magnetic field B are aligned, and f_{scan} is the scanning frequency. If the vector of the magnetic field is expressed in polar coordinates with respect to the reference axis, the CVHD's output voltage is as follows:

$$V_{CVHDc} = Re\left(I_{bias}Be^{j\alpha}S_0 e^{-j2\pi f_{scan}t}\right) = S_0 I_{bias}B\cos\left(2\pi f_{scan}t - \alpha\right), \tag{5.2}$$

where S_0 is the maximum sensitivity of the device, f_{scan} is the scanning frequency, B is the magnitude of the total in-plane magnetic field, α is the angle enclosed between the reference axis and the total in-plane magnetic field, and I_{bias} is the biasing current of the Hall device.

If the rotation of the biasing and sensing contacts is done in the counterclockwise direction, Fig. 5.2, then the sensitivity vector of the CVHD can be approximated by:

$$S_{cc} = S_0 e^{j2\pi f_{scan}t}. \tag{5.3}$$

The CVHD's output voltage is in this case:

$$V_{CVHDcc} = Re\left(I_{bias}Be^{j\alpha}S_0 e^{j2\pi f_{scan}t}\right) = S_0 I_{bias}B\cos\left(2\pi f_{scan}t + \alpha\right). \tag{5.4}$$

73
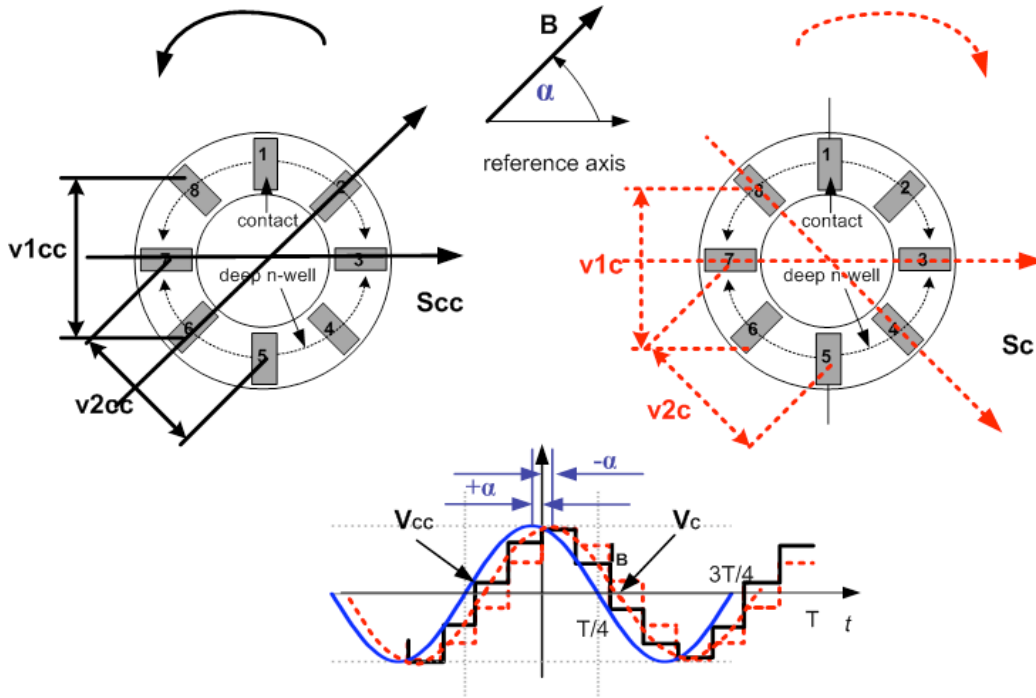
Figure 5.2: Biasing and sensing of Hall voltage from the 8CVHDs: clockwise (dashed line), counter-clockwise (full line) and the band-pass filtered signals for the in-plane DC magnetic field enclosing the angle α with the reference axis (biasing and the second Hall voltage of Fig. 5.1 are omitted for simplicity)

In other words, the sensitivity axis is rotated by the positive angular velocity in the clockwise case. In the counterclockwise case, the sensitivity vector is rotated by negative angular velocity. For the 8CVHD biased in the clockwise direction, the phase shift corresponding to the angle of the magnetic induction vector is positive, the waveform in full line in Fig. 5.2. In contrast, if the 8CVHD is biased and the Hall voltage sensed in the counterclockwise direction, then the phase shift corresponding to the angle of the magnetic induction vector is negative, the waveform in dashed line in Fig. 5.2.

In this way, two signals of the same amplitude but with opposite phase shifts can be obtained.

The block-diagram of the sensor is shown in Fig. 5.3, while the corresponding waveforms are shown in Fig. 5.2 right. There are two Hall devices and two identical signal processing channels, respectively. In the first channel the Hall voltage is sensed clockwise from the first 8CVHD. In the second channel the Hall voltage is sensed counterclockwise from the second device.

When biasing the device as shown in Fig. 5.2 all contacts are used and there are two Hall voltages. These two Hall voltages, being of the same polarity, are summed by means of the two-input differential difference amplifier (DDA) serving as the preamplifier of the system. The integrated digital electronics module, with off-chip clock generator, delivers control signals for switches for biasing the 8CVHDs and sensing the Hall voltage from them. Each contact of the 8CVHD is

74
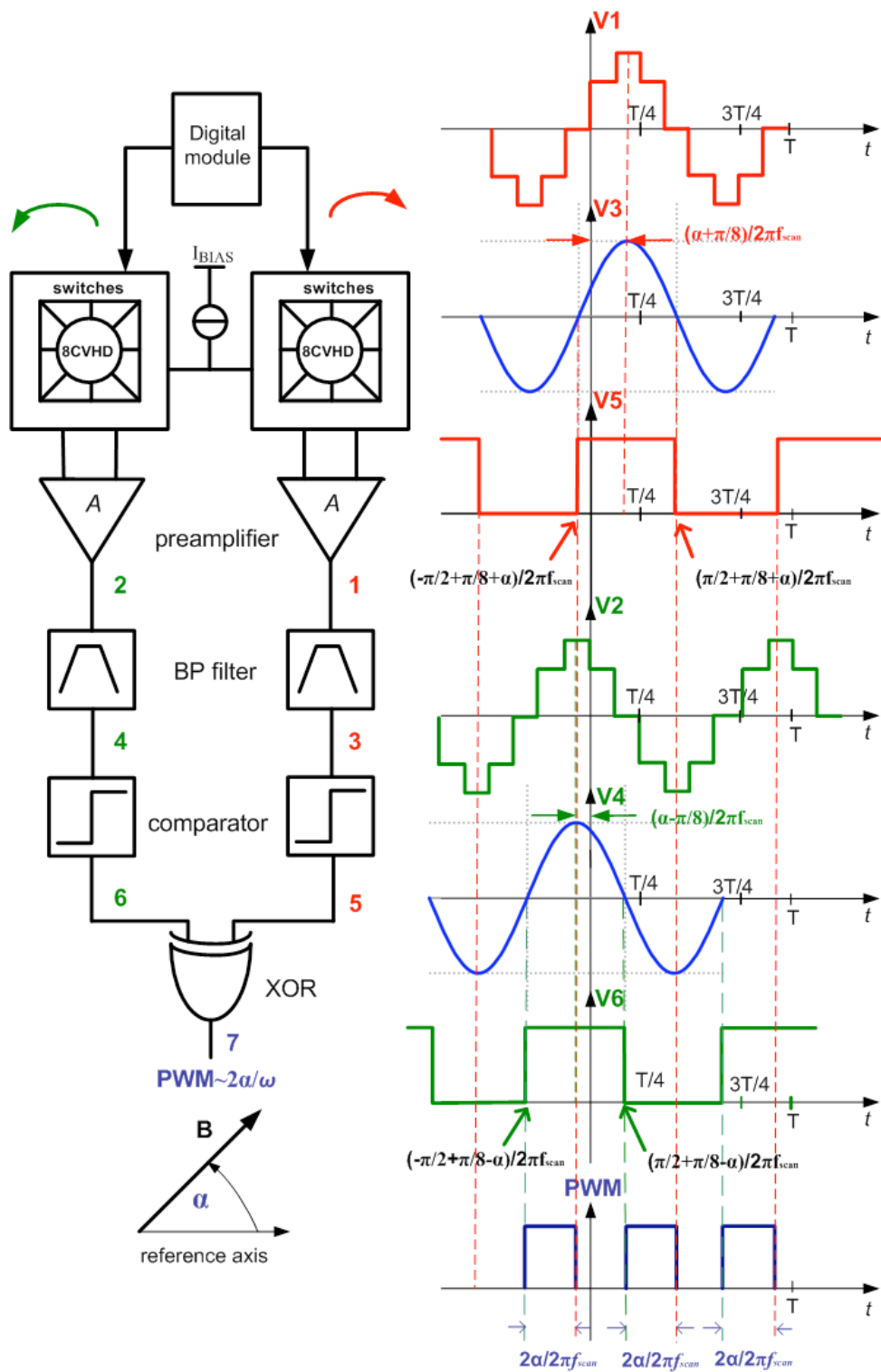
Figure 5.3: a) Block diagram of the sensor, b) signal waveforms along the channels for the in-plane DC magnetic field including the angle $\alpha = 45^{\underline{o}}$ with the reference axis. Due to the finite number of contacts, there is an intrinsic phase shift $\pi/8$ after bandpass filtering, as discussed in Chapter 4

through switches connected to biasing current source, ground or one of the two inputs of the DDA. In total, each contact has a battery of six switches. The outputs of the preamplifiers are taken to the band pass filter. The purpose of the band pass filter is to extract the fundamental harmonic out of the eight-step sine wave. The filter also reduces noise, eliminates out-of-band spectral components of offset, and strongly attenuates the voltage spikes (see Chapter 3).

As mentioned in Chapter 4, due to the finite number of contacts there is an intrinsic phase shift in the bandpass filtered signal. For the eight contacts, the intrinsic phase shift is $\pi/8$ with respect to the beginning of the first main sensing step. Nevertheless, since both channels are affected in the same way, the relative phase shift is proportional only to the measured angle, as will be shown below. The outputs of the band pass filters for the clockwise and counterclockwise devices in the ideal case are given by, respectively:

$$V_{cBP} = A S_0 I_{bias} B \cos\left(2\pi f_{scan} t - \alpha - \pi/8\right), \tag{5.5}$$

$$V_{ccBP} = A S_0 I_{bias} B \cos\left(2\pi f_{scan} t + \alpha - \pi/8\right), \tag{5.6}$$

where A is amplification of the preamplifier and band pass filter, S_0 is sensitivity of the 8CVHD, I_{bias} is the biasing current of the device, B is the magnitude of the total in-plane magnetic field sensed by the device, f_{scan} is the scanning frequency and α is the angle between the in-plane magnetic field and the reference axis of the device. The outputs of the band pass filters are fed into the comparators serving as zero-crossing detectors. Finally, the phase difference between the sine waves in two channels is measured by the simplest phase detector - an exclusive OR (XOR) gate. The outputs of the comparators can be modeled by the modified signum function as shown below:

$$V_{cCOMP} = sgn\left[A S_0 I_{bias} B \cos\left(2\pi f_{scan} t - \alpha - \pi/8\right)\right] = $$
$$= \begin{array}{ll} V_{DD} & \frac{-3+8k}{16 f_{scan}} + \frac{\alpha}{2\pi f_{scan}} < t < \frac{5+8k}{16 f_{scan}} + \frac{\alpha}{2\pi f_{scan}} \\ 0 & \frac{5+8k}{16 f_{scan}} + \frac{\alpha}{2\pi f_{scan}} < t < \frac{-3+8k}{16 f_{scan}} + \frac{\alpha}{2\pi f_{scan}} \end{array}, \tag{5.7}$$

$$V_{ccCOMP} = sgn\left[A S_0 I_{bias} B \cos\left(2\pi f_{scan} t + \alpha - \pi/8\right)\right] = $$
$$= \begin{array}{ll} V_{DD} & \frac{-3+8k}{16 f_{scan}} - \frac{\alpha}{2\pi f_{scan}} < t < \frac{5+8k}{16 f_{scan}} - \frac{\alpha}{2\pi f_{scan}} \\ 0 & \frac{5+8k}{16 f_{scan}} - \frac{\alpha}{2\pi f_{scan}} < t < \frac{-3+8k}{16 f_{scan}} - \frac{\alpha}{2\pi f_{scan}} \end{array}, \tag{5.8}$$

where k=0, 1... , n, and n is an integer.

The exclusive OR gate (XOR) gives a pulse at its output whenever the two inputs have opposite logic levels. There are two pulses per one period of the scanning frequency because the XOR gate reacts both on falling and rising edges. The output of the XOR is given by:

$$V_{XOR} = \begin{array}{ll} V_{DD} & \frac{-3+8k}{16 f_{scan}} - \frac{\alpha}{2\pi f_{scan}} < t < \frac{-3+8k}{16 f_{scan}} + \frac{\alpha}{2\pi f_{scan}} \wedge \frac{5+8k}{16 f_{scan}} - \frac{\alpha}{2\pi f_{scan}} < t < \frac{5+8k}{16 f_{scan}} + \frac{\alpha}{2\pi f_{scan}} \\ 0 & \frac{-3+8k}{16 f_{scan}} + \frac{\alpha}{2\pi f_{scan}} < t < \frac{5+8k}{16 f_{scan}} - \frac{\alpha}{2\pi f_{scan}} \wedge \frac{5+8k}{16 f_{scan}} + \frac{\alpha}{2\pi f_{scan}} < t < \frac{-3+8k}{16 f_{scan}} - \frac{\alpha}{2\pi f_{scan}} \end{array}. \tag{5.9}$$

The above expression shows that the output of the XOR gate is a PWM signal whose pulse width is equal to $2\alpha/2\pi f_{scan}$. The pulses are centered around $(-3+8k)/(16f_{scan})$ and $(5+8k)/(16f_{scan})$. This type of PWM signal is known as the double edge symmetrical PWM [71].

In the following analysis we assume perfect matching of the channels. Then the phase shifts introduced by the signal processing electronics in the two channels are equal. If the phase shift of the signal processing electronics is denoted by φ, then the outputs of the band pass filters for the clockwise and the counterclockwise devices are, respectively:

$$V_{cBP} = AS_0 I_{bias} B \cos\left(2\pi f_{scan}t - \alpha - \pi/8 + \varphi\right), \tag{5.10}$$

$$V_{ccBP} = AS_0 I_{bias} B \cos\left(2\pi f_{scan}t + \alpha - \pi/8 + \varphi\right). \tag{5.11}$$

The absolute phase shift of the signals in the channels is affected by the phase shift φ. However, the relative phase shift remains constant. The output of the XOR is again proportional to 2α irrespective of the phase shift φ. The sensor's system level concept allows for insensitivity of the PWM signal to temperature drift. The sensitivity drift of the 8CVHDs with temperature affects only the amplitude of the sine waves and not the phase shift. The same is true for the drift with temperature of the gains of preamplifiers and band pass filters. The signal processing electronics phase shift φ is affected by temperature dependence of the preamplifier, band pass filter and comparator. But due to the matched channels the phase shift φ is cancelled out on the system level.

5.2.2 Error analysis

The dominant sources of angular error stemming from the 8CVHD are: the offset voltage spectral component at the scanning frequency, or the first harmonic of offset (Chapter 2) and the spectral component of the voltage spikes at the scanning frequency. In the ideal offsetless case the second harmonic of the 8CVHD's voltage is zero and it won't be considered here.

The spectrum of the offset voltage is distributed, with spectral components at DC, the scanning frequency and stretching up to the sensing frequency. The offset spectral component at the scanning frequency is greatly reduced due to the four-phase spinning in main sensing steps, as discussed in Chapter 2. In the case of the 8CVHD, the four-phase spinning enabled its reduction down to 200 µT [57]. Similarly to the offset voltage, the low frequency 1/f noise of the 8CVHD is greatly reduced by the four-phase spinning within one main sensing step. A band pass filter with center frequency at the scanning frequency filters out signal conditioning's 1/f noise, DC spectral component of the offset and its higher harmonics. The offset spectral component at the scanning frequency cannot be filtered out. Neither can be filtered out the 1/f noise remaining after the four-phase spinning. The sketch of the offset voltage, for the Hall voltage retrieval described in Chapter 3, is given in Fig 5.4.
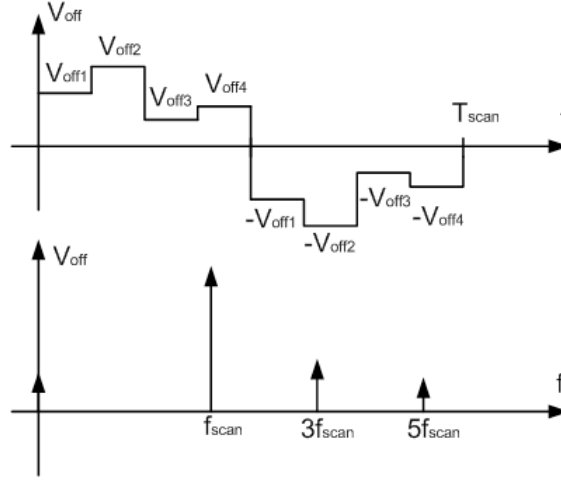
Figure 5.4: Sketch of the magnitudes of the spectral components of the 8CVHD's offset voltage. The offset voltage is an odd function due to the repeated biasing scheme in the second half period and reversed sensing of the Hall voltage

The influence of the amplitude and polarity of the voltage spikes due to the spinning current method is given in Chapter 3. The second solution to spikes cancellation relying on the partial guard band was implemented here. The control signals for the sensing switches are delayed with respect to the biasing switches. In this way, the sensing contacts of the 8CVHD are connected to the preamplifier only after some time has elapsed from the beginning of the transient processes. During this time the accumulated charge is discharged through the Hall impedance, as discussed in 3.1.2. The end result is that the spikes in the output voltage of the 8CVHD "seen" by the input of the preamplifier have smaller amplitude.

The Hall voltage retrieval features the same polarity of the voltage spikes in all sensing phases, as illustrated in Fig. 5.5. This means that in the ideal case the spectral component of the spikes at the scanning frequency is zero. In the real case, the amplitude of spikes depends also on the offset and Hall voltages in a given sensing phase, as discussed in Chapter 2. The remaining of the spikes after filtering adds to the unfiltered offset spectral component at the scanning frequency. Together they give rise to the first harmonic that superimposes on the useful signal. This first harmonic cannot be filtered out and it causes an error. This error is angle dependent. The output of the bandpass filters is in the real case:

$$V_{cBP} = AS_0 I_{bias} B \cos\left(2\pi f_{scan} t - \alpha - \pi/8\right) + AV_{offc} \cos\left(2\pi f_{scan} t + \alpha_{offc}\right), \qquad (5.12)$$

$$V_{ccBP} = AS_0 I_{bias} B \cos\left(2\pi f_{scan} t + \alpha - \pi/8\right) + AV_{offcc} \cos\left(2\pi f_{scan} t + \alpha_{offcc}\right), \qquad (5.13)$$

where V_{offc} and V_{offcc} denote the amplitude, while α_{offc} and α_{offcc} denote the phase of the residual offset voltage and voltage spikes at the scanning frequency, in the clockwise and counterclockwise
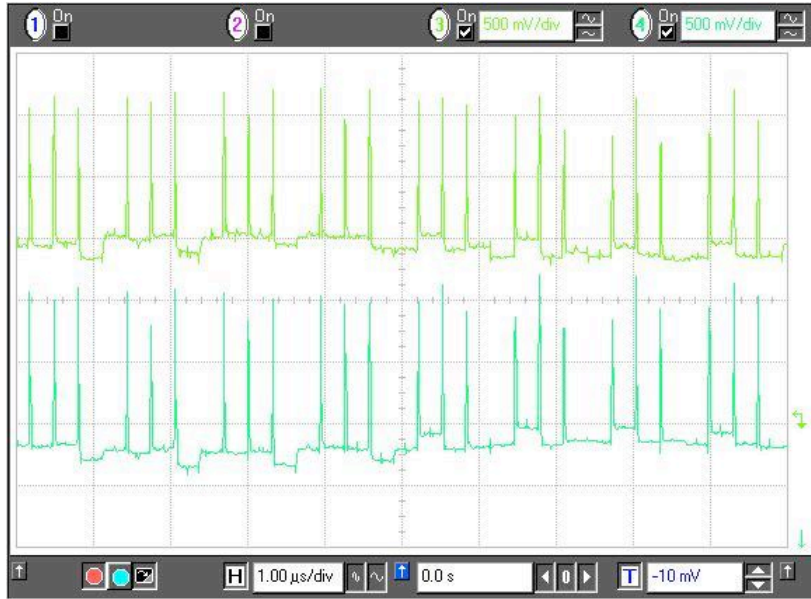
Figure 5.5: Measured signal at the outputs of the preamplifiers in the clockwise and counterclockwise channels for 100 kHz scanning frequency, 50 mT magnetic field and f_{clock}= 3.2 MHz. The polarity of the voltage spikes remains constant over the scanning period. Due to the same biasing sequence in the clockwise and counterclockwise channels the voltage spikes waveforms are almost identical

channels, respectively. The residual offset voltage can be represented as a stationary vector superimposing on the vector of the magnetic field and causing an error. The smaller the ratio of the amplitudes of the offset and magnetic field vectors, the smaller is the angular error.

It should be noted here that the sensor's system level concept eliminates nonlinearities caused by higher harmonics of the voltage spikes. Namely, the sequence of the potential changes of the contacts for the clockwise and counterclockwise devices is the same. Then the spikes waveform can be seen as identical for both channels to the first approximation, Fig. 5.5. The 3rd order filter greatly attenuates the higher harmonics of the voltage spikes, but does not eliminate them completely. The magnitudes of higher harmonics are equal in two channels to the first approximation. They affect the useful signal similarly to the phase shifts introduced by the signal processing electronics, as shown above. The absolute phase shifts of the signals in two channels are affected, but the relative phase shift remains invariant.

The mismatches in the signal conditioning electronics in two channels also lead to an error. This error is much smaller than the error caused by the nonidealities of the 8CVHD.

5.2.3 Signal conditioning electronics

The biasing current of the Hall device was set by a variable resistor connected in series with the diode-connected PMOS of an on-chip current mirror.

The contacts of the 8CVHD are through a battery of six complementary switches connected to:

Input CM range	0.5-2 V
DC open loop gain	56 dB
Closed loop gain (R1= 500 Ω, R2= 4500 Ω)	20
GBW (capacitive load 2 pF, capacitive load 15pF)	360 MHz, 180 MHz
Input-referred noise	11.8 nV/√Hz @ 100 kHz; 7.7 nV/√Hz @ 1 MHz
Input referred offset ($\pm 3\sigma$)	$\pm$ 4.1 mV
Current consumption	8.5 mA

Table 5.1: Simulated characteristics of the preamplifier

biasing current source, ground (two biasing switches), and to positive or negative inputs of the two signal inputs of the DDA (four sensing switches). The two opposite contacts are connected through a low resistance switch in order to perform the four-phase spinning current method for offset reduction as shown in Chapter 3.

The digital electronics module with off-chip clock generator controls switches. Both schematics and layout of the digital module were automatically synthesized after a VHDL code in the commercially available software. No care was taken during design to synchronize switch control signals at the output of the digital module. This was done in order to avoid stringent routing requirements. Instead, a D-flip flop was placed next to the switches in the layout to synchronize the control signals. An additional simple logic was placed next to the sensing switches to realize guard band.

The two Hall voltages taken from the 8CVHD in each sensing phase are summed by means of the two-input DDA (see Chapter 4). It contains two signal inputs and one feedback output. Its simulated characteristics are given in Table 5.1. The low gain and high bandwidth of the DDA were chosen in order to prevent saturation and nonlinear distortion due to spikes in the Hall voltage. The outputs of the DDA were connected to pads and served as probe points to study spikes. The bandwidth of the DDA was overdesigned and current consumption increased to accommodate for large capacitive loads of the probing instrument while still allowing for settling of the voltage spikes.

The band-pass filter was designed as a cascade consisting of linear RC filters, two low gain classical two-stage amplifiers (gain 10 and 20, respectively) and a buffer, as shown in Fig. 5.6 . The distributed configuration was chosen to prevent saturation due to spikes, optimize filtering of the spectral components of spikes and offset, and avoid nonlinearities. The band-pass filter is a 3rd order filter and its bandwidth is about 1 MHz (low and high 3dB points are, respectively, 10 kHz and 1.1 MHz). The bandwidth was intentionally designed high in order to accommodate for large span of scanning frequencies. The downside of the high bandwidth is increased integrated noise and reduced angular resolution.

The comparators were realized as open loop two-stage amplifiers. The comparator's delay times for the rising and falling edges of the 20 mV pulsed wave are 122ns and 88 ns, respectively.
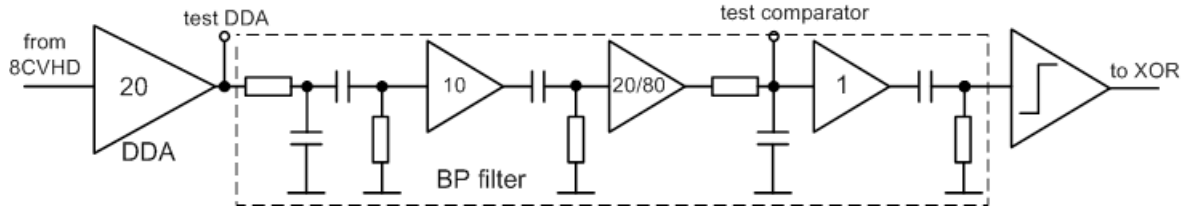
Figure 5.6: Distributed filtering and amplification stages in one channel

The total power consumption is 90 mW at the scanning frequency 750 kHz. No effort was made to optimize the sensor for low power consumption.

5.2.4 Measurement results: DC characterization

The chip was fabricated in 3.3 V AMS high voltage 0.35 μm technology. The high voltage technology was chosen because of the availability of the deep N-well which enhances CVHD's sensitivity. The chip microphotograph is shown in Fig. 5.7. The sensor's characteristics were measured in two measurement settings: 1) response to a low speed rotating vector, 2) response to a high speed oscillating vector.

The sensor's output for in-plane magnetic induction vector is shown in Fig. 5.8. Due to the non-ideal matching of the channels, the spacing and widths of the two pulses within one period are not equal. But, the average of the two subsequent pulses corresponds to the correct value of the measured angle.

The transfer curve of the sensor for the magnetic induction vector rotated over 360° is shown in Fig. 5.9. A Newport rotary encoder with 0.01° accuracy was used to rotate a diametrically magnetized permanent magnet. The magnetic induction vector at the position of the sensor was 43.2 mT. The PWM signal was averaged and recorded by a high resolution programmable timer/counter/analyzer (Fluke PM6681). This reading was then multiplied by the scanning frequency to obtain the angle. The triangular shape of the transfer characteristic is caused by the phase detection properties of the XOR gate and the fact that the sensor measures twice the angle. The unambiguous measurement range is from 0 to 90°.

The absolute angular error for two scanning frequencies for one sample is shown in Fig. 5.10. The dominant cause of the error for small angles is the mismatch in the first harmonics caused by both residual offset and spikes, and the channels' mismatch. The error around 90° is dominantly caused by the offset voltage and different rise and fall times of the comparators. Several samples of the magnetic sensor were tested with magnetic fields up to 100 mT at the scanning frequency 750 kHz. Their best angular error was $\pm 3^{\circ}$.

The angle resolution was found by measuring the width of the PWM by a time-to-digital converter (TDC) and calculating its standard deviation [72]. The resolution is limited by jitter in the PWM signal which is caused by the signal's amplitude noise at the comparator's input. The histogram of
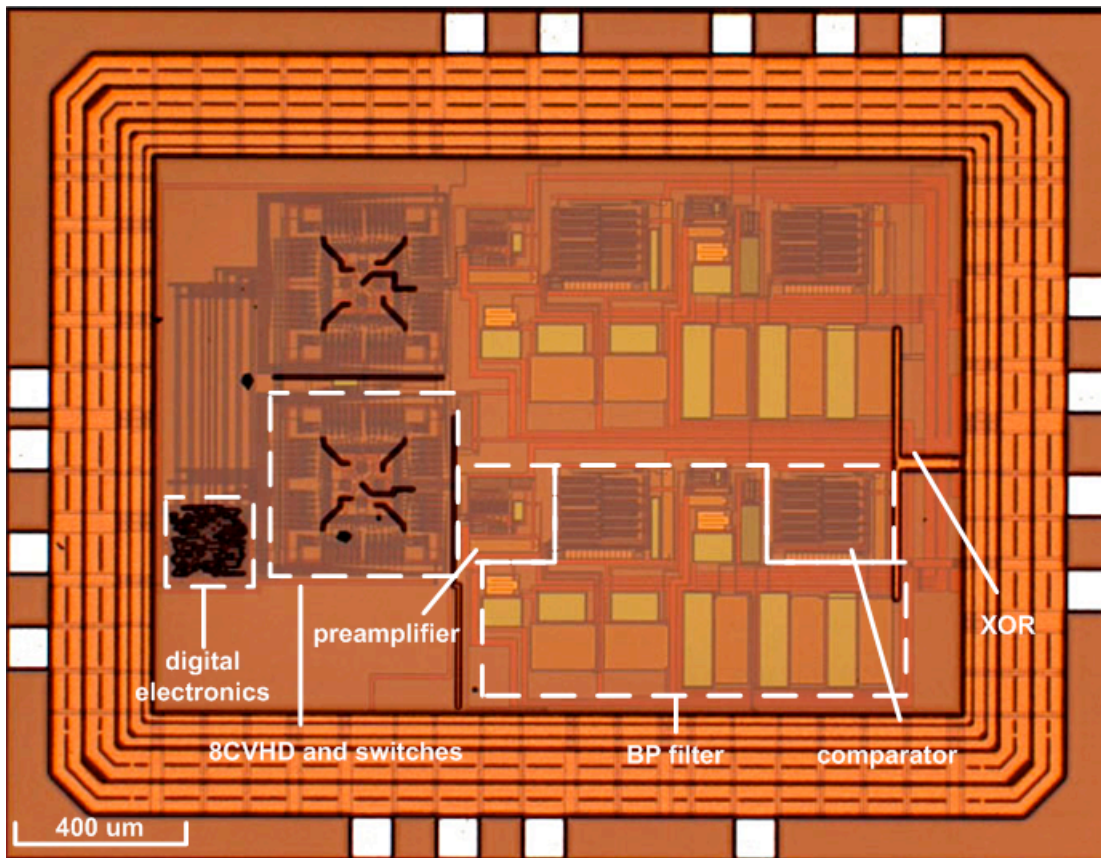
Figure 5.7: Microphotograph of the high speed angular sensor with one 8CVHD per channel
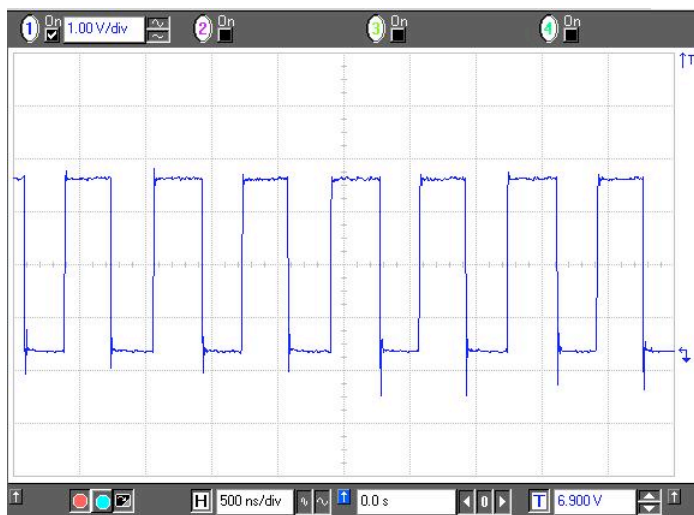
Figure 5.8: Measured sensor's output for 60 mT in-plane DC magnetic field including 50° with the reference axis. The scanning frequency is 750 kHz (the frequency of the PWM signal is twice the scanning frequency)
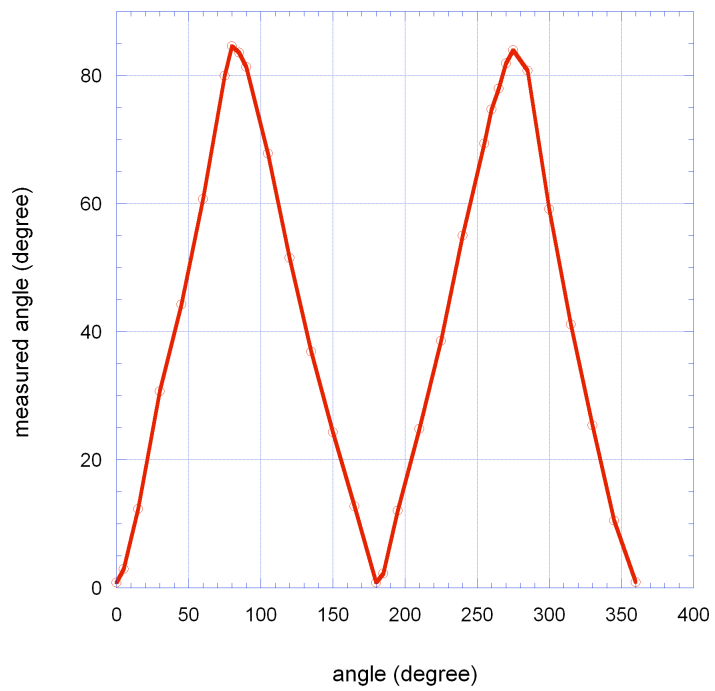
Figure 5.9: Transfer characteristic of the sensor for the scanning frequency 1 MHz, Hall biasing current 300 µA and the rotating 43.2 mT DC magnetic field
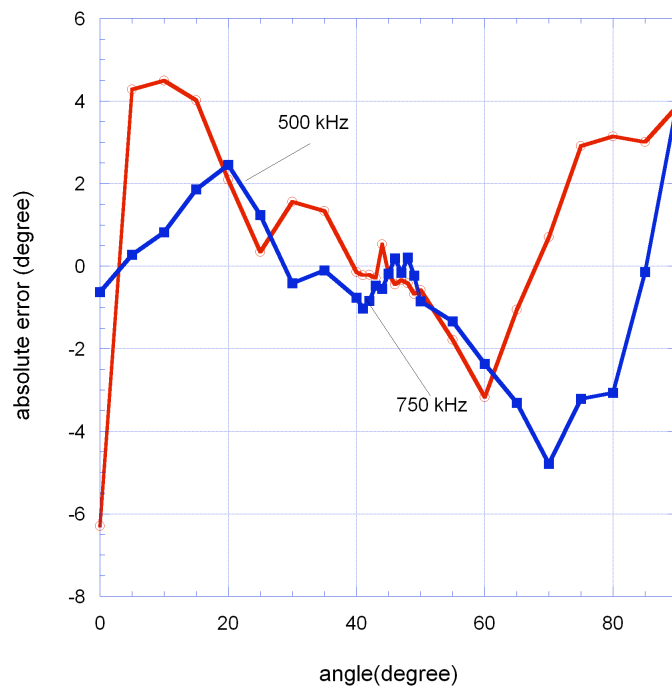
Figure 5.10: Absolute angular error for the Hall biasing current 600 µA, 43.2 mT rotating DC magnetic field and the scanning frequencies 500 kHz and 750 kHz
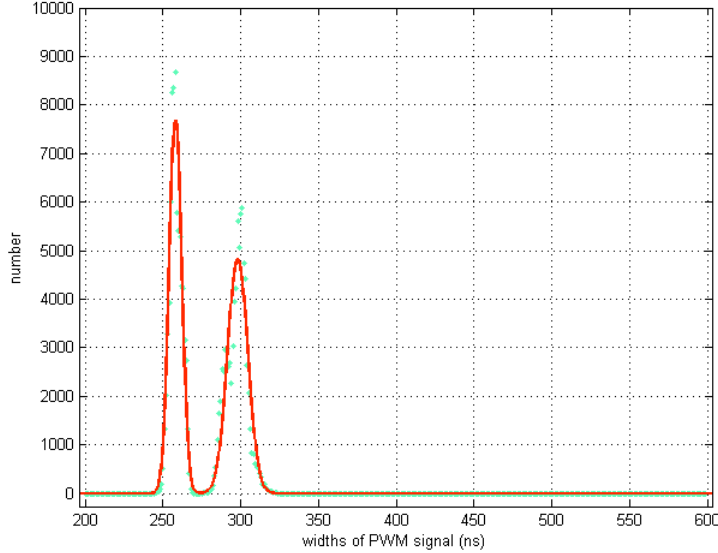
Figure 5.11: Histogram of the PWM signal for the scanning frequency 1 MHz, arbitrary angle and 50 mT magnetic field (dashed line denotes measured values, whereas the full line denotes the fitted curve)

the PWM is given in Fig. 5.11. The histogram has two peaks due to different pulse widths caused by non-ideal matching of the channels, as explained above. When changing the scanning frequency from 500 kHz to 1 MHz, the resolution changes from 0.5º for 500 kHz to 1.3º for 1 MHz. The angle resolution can be increased by reducing the bandwidth of the band pass filter due to decrease of the integrated noise at the input of the comparators. For larger magnetic fields the signal to noise ratio at the input of comparator is higher and resolution is better.

In the ideal case, temperature drift of the 8CVHDs and the signal conditioning electronics is cancelled up to the XOR gate due to the differential system topology. However, the measured angle drifts with temperature due to the 8CVHD's offset voltage drift, channels mismatches and temperature dependence of the XOR gate and the chip's output pad. The angle change per degree ºC for the scanning frequencies changed from 500 kHz to 1 MHz changes from 0.030º/ ºC to 0.0276º/ ºC.

5.2.5 Measurement results: AC characterization

An ideal experiment for characterization of the sensor's bandwidth would be to expose it to a high speed rotating motor with a diametrical magnet attached to it. The angular speeds of motors available to us were modest and much below the sensor's bandwidth. This is why we generated a high speed oscillating magnetic vector by superposition of a DC and an AC magnetic fields. The
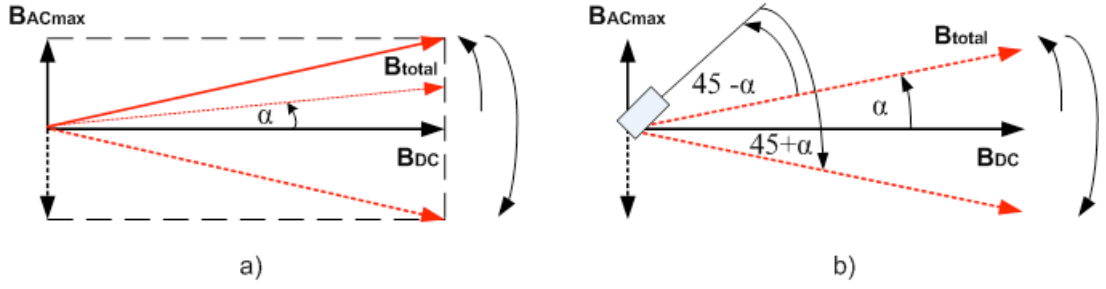
Figure 5.12: a) Generation of high speed oscillating magnetic vector, b) sensor rotated by 45⁰ to distinguish positive from negative angles, where α is the instantaneous angle enclosed between the total vector and the DC field (right)
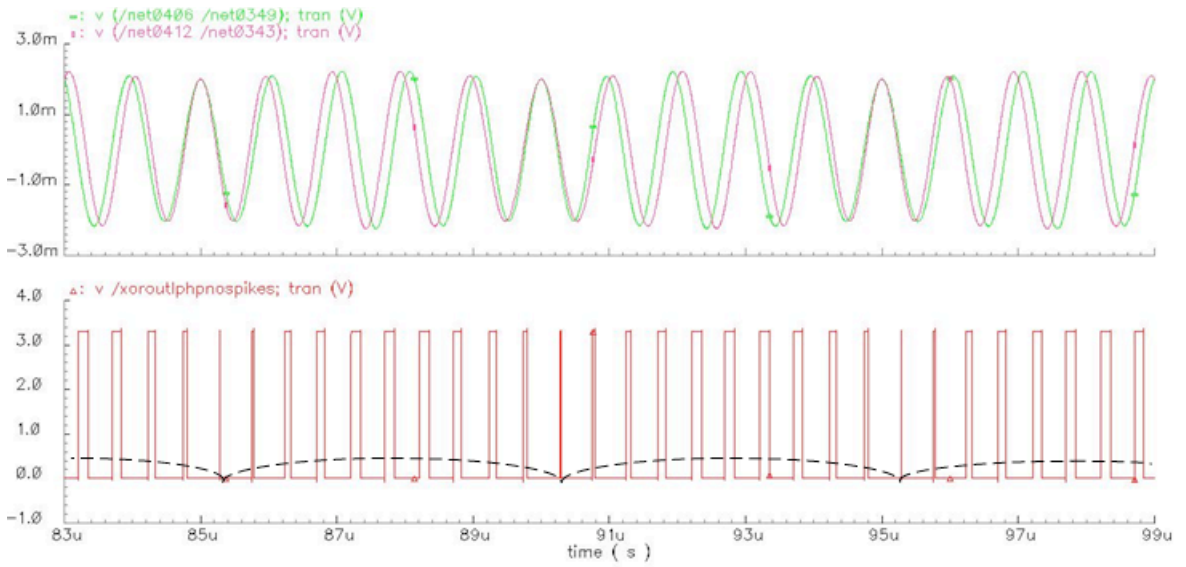
Figure 5.13: Simulated waveforms of the sensor for the magnetic field vector rotating at $2\pi*100$ kHz and 1 MHz scanning frequency: top - inputs to the comparators, bottom - XOR output (full line), and low pass filtered XOR output is demodulated sine function (dashed line)

sensor was exposed to a DC magnetic field, aligned with the reference axis, and an AC magnetic field perpendicular to the reference axis. The fluctuations of the AC field cause change in direction and magnitude of the total field vector. In this way an in-plane oscillating magnetic vector was created. Its angular frequency is proportional to the frequency of the AC field, Fig 5.12a).

The response of the 8CVHD to the high speed oscillating vector after band-pass filtering is shown in Fig. 5.13. It is the amplitude and phase modulated signal.

After the bandpass filtering, the signal in the clockwise channel is given by:

$$V_{cBP} = AS_0 B_{res} I_{bias} \cos\left(2\pi f_{scan} t - \alpha\right), \tag{5.14}$$

where the intrinsic phase shift is omitted for simplicity. The resultant magnetic field $\mathbf{B_{res}}$, and the angle α it encloses with the reference axis are as follows, respectively:

$$B_{res} = \sqrt{B_{DC}^2 + B_{AC}^2(t)}, \tag{5.15}$$

$$\alpha = \arctan \frac{B_{AC}(t)}{B_{DC}}, \tag{5.16}$$

and the AC magnetic field is given by:

$$B_{AC}(t) = B_{ACmax} \sin(2\pi f_{AC} t), \tag{5.17}$$

where S_0 is the maximum sensitivity of the device, I_{bias} is the biasing current of the Hall device, f_{scan} is the scanning frequency, B_{DC} is the magnitude of the DC field, and $B_{AC}(t)$ is the instantaneous value of the AC field. If the following condition is satisfied:

$$B_{ACmax} \ll B_{DC}, \tag{5.18}$$

then Eqn 5.14 can be rewritten to be:

$$V_{cBP} = AS_0 B_{res} I_{bias} \cos\left(2\pi f_{scan} t - \frac{B_{ACmax}}{B_{DC}} \sin(2\pi f_{AC} t)\right), \tag{5.19}$$

$$V_{cBP} \approx AS_0 B_{res} I_{bias} \left\{ \cos\left(2\pi f_{scan} t\right) + \frac{B_{ACmax}}{2B_{DC}} \left[\cos\left(2\pi (f_{scan} - f_{AC})t\right) - \cos\left(2\pi (f_{scan} + f_{AC})t\right)\right] \right\}, \tag{5.20}$$

In the similar manner, the output of the band pass filter in the counterclockwise channel is given by:

$$V_{ccBP} = AS_0 B_{res} I_{bias} \cos\left(2\pi f_{scan} t + \frac{B_{ACmax}}{B_{DC}} \sin(2\pi f_{AC} t)\right). \tag{5.21}$$

The comparators eliminate amplitude modulation of the bandpass filtered signals leaving the phase modulated signal. If the condition stated in Eqn 5.18 is satisfied, the spectrum of this phase modulated signal is equivalent to the spectrum of the amplitude modulated signals, Eqn 5.20: it has a sinusoid at the scanning frequency f_{scan} (the carrier frequency in telecommunications systems) and two sinusoids at the frequencies $f_{\text{scan}} - f_{AC}$ and $f_{\text{scan}} + f_{AC}$, lower and upper sidebands, respectively. The maximum scanning and AC field frequencies are limited by the passband of the bandpass filter. The upper limit is critical; here it is given by: $f_{\text{scan}} + f_{AC} < 1.1$ MHz.

The information on the instantaneous value of the angle $2\alpha \approx 2\frac{B_{ACmax}}{B_{DC}} \sin(2\pi f_{AC} t)$ is encoded in the varying width of the PWM signal. The instantaneous value of the angle α enclosed between the oscillating vector and the reference axis can be found by feeding the XOR signal to the time to digital converter (TDC) and measuring the duration of pulses.
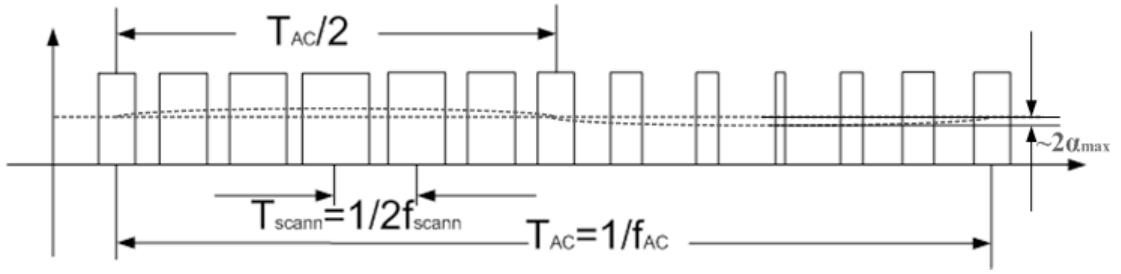
Figure 5.14: XOR output signal for the sensor rotated by 45° with respect to the applied DC reference field (filtered DC and AC values are shown in dashed lines)

The output of the XOR shown in Fig. 5.13 contains the rectified AC signal due to the properties of the XOR gate. The XOR gate reacts on both falling and rising edges. In other words, the sensor does not distinguish between the positive and negative angles. Therefore the chip was rotated by 45° in order to make it sensitive to positive and negative angles, Fig. 5.12b). In this case, the width of the PWM signal is proportional to 90° - 2α, Fig. 5.14. In addition, the "operating point" is placed in the middle of the transfer curve, where linearity is the best.

The scanning frequency of the sensor can be seen as the sampling frequency in sampled electronic systems. According to the sampling theorem, the maximum frequency of the oscillating vector should be at most half the scanning frequency, but oversampling ratios of 7 to 10 are desirable.

The amplitude-frequency characteristic of the sensor was recorded by sweeping the frequency of the AC field and monitoring the sensor's output in the frequency domain. The low pass filter was placed between the XOR output and the input to the spectrum analyzer. The sensor's output in the frequency domain consists of the DC component (downconverted scanning frequency) and the first harmonic at the frequency of the AC field. Higher harmonics are also present due to the properties of the PWM modulation, but their amplitudes are two orders of magnitude lower than that of the first harmonic [71]. The magnitude of the first harmonic is proportional to twice the maximum angle enclosed between the oscillating vector and the reference axis:

$$A_1 \mid_{f_{AC}} \sim 2 \frac{B_{ACmax}}{B_{DC}}. \qquad (5.22)$$

The measured amplitude-frequency characteristic of the sensor is shown in Fig. 5.15. It was recorded for the oscillating vector created by 25 mT DC field and an AC field with 2.25mT amplitude. These values satisfy Eqn 5.18. The maximum AC field frequency for which the sensor outputs correct value of the maximum angle is 200 kHz, or equivalently 12 000 000 rpm. This corresponds to about 71 000 rad/s for this maximum amplitude of the AC field and this angular measurement range. For the measurement range ($\pm$ 45°) this would correspond to 628 000 rad/s. For higher angular frequencies aliasing was observed.

87
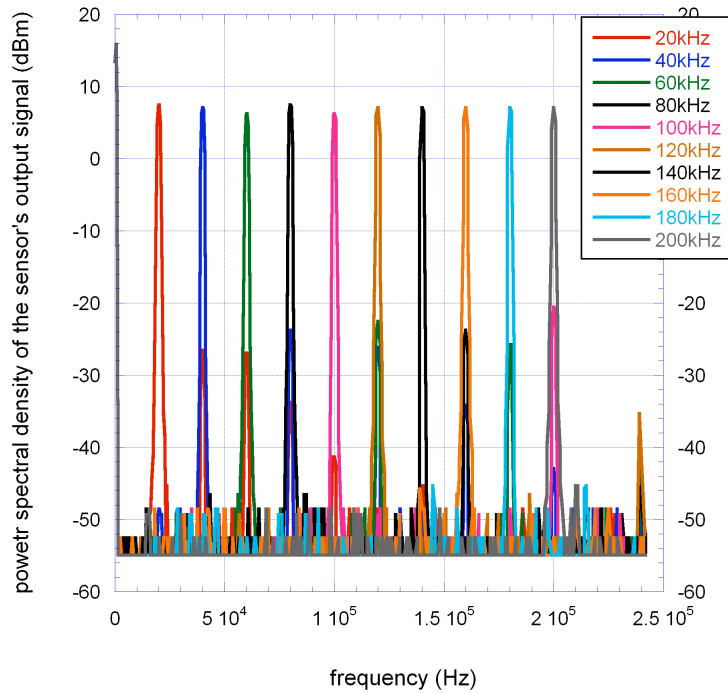
Figure 5.15: Amplitude-frequency characteristic of the sensor for 625 kHz scanning frequency. The frequency of the AC field generating the oscillating magnetic field was swept up to one third of the scanning frequency

The response time of the sensor corresponds approximately to the reciprocal value of the sensor's bandwidth. The bandwidth was designed very high in order to accommodate for the large span of scanning frequencies. The sensor's bandwidth is approximately 1 MHz which gives about 1 μs for the response time.

5.3 High speed magnetic angle sensor with an array of 8CVHDs per channel

The second version of the high speed magnetic angle sensor contains an array of 8CVHDs per channel. The front end of the current transducer consists of an array of four 8CVHDs divided in two pairs, as was described in Chapter 3. Each pair consists of two 8CVHDs. The spinning current method is performed clockwise on the first device and counterclockwise on the second device. The novelty with respect to the previous solutions lies in time shifted spinning current on the two pairs. Namely, the first main sensing phase of the second pair is shifted by half the main sensing step with respect to the first main sensing step of the first pair. The cancellation by clockwise and counterclockwise spinning always yields a residual spike due to the nonidealities discussed above. These residual spikes are at least one order of magnitude smaller than the voltage spikes of one device. More importantly, their polarity is arbitrary. By the addition of the second pair, there are two residual spikes of the

arbitrary polarity per one sensing phase and their influence on the useful signal becomes similar to that of noise. In the frequency domain these residual spikes can be approximated by the white noise. The microphotograph of the sensor is shown in Chapter 6, Fig 6.11.

On the other hand, the additional pair allows for lower biasing current of the 8CVHD. This in turn leads to higher signal-to-residual offset ratio for the array of the four devices. The outputs of the two pairs are summed by means of an eight-input DDA serving as a preamplifier. The preamplifier's input capacitance is C_2= 0.1 pF. According to Eqn 3.22 the approximate settling time is about 6 ns, which poses the theoretical limit to the maximum sensing frequency of around 160 MHz. This would correspond to 5 MHz scanning frequency of the 8CVHD, or the maximum bandwidth of 2.5 MHz.

The block-diagram of the sensor is similar to that shown in Fig. 5.3. The signal conditioning electronics was optimized with respect to the first implementation described in section 5.2. The first preamplifier was redesigned to allow for summing up of the Hall voltages from four 8CVHDs. Instead of the two-input DDA, the first preamplifier has a topology of an eight-input DDA. Instead of the distributed topology of passive filtering, Fig. 5.6, the bandpass filter was designed as an active bandpass filter. It was redesigned to accommodate filtering the 8CVHD's signal at two scanning frequencies: 200 kHz and 1 MHz. The filter's bandwidth around 200 kHz is 48 kHz, while its bandwidth around 1 MHz is 350 kHz. The Schmitt trigger added to the comparators leads to a reduced jitter in the PWM signal. The reduced bandwidth of the bandpass filter led to lower integrated noise and consequently lower amplitude noise of the signal at the comparator's input. The increased signal-to-noise ratio led to the increase of the overall resolution of the Hall magnetometer.

5.3.1   Measurement results: DC characterization

The transfer characteristic of the sensor is shown in Fig. 5.16. The sensor was rotated over 360° in the constant magnetic field created by an electromagnet.

The absolute angular error for the magnetic field 118 mT is shown in Fig. 5.17. The PWM signal was recorded by a high resolution programmable timer/counter/analyzer (Fluke PM6681) without averaging. The recording was then multiplied by the scanning frequency to obtain the angle. The front end design, as discussed in Chapter 3, together with the optimized signal conditioning electronics yields better absolute error (compare with Figs. 5.9 and 5.10). The measured resolution for the scanning frequency 1 MHz and the magnetic field 118 mT is 0.15°. This is an order of magnitude better than 1.3° for 1 MHz in the sensor described in Section 5.2.

In Table 5.2 are summarized results of the two CMOS implementations described above. Version 1 refers to the angular sensor with one 8CVHD per channel, while version 2 refers to the angular sensor with an array of the 8CVHDs per channel. The performance of the angular sensors are compared with the similar CMOS realizations referred to in the state-of-the-art in 5.1. As mentioned above,
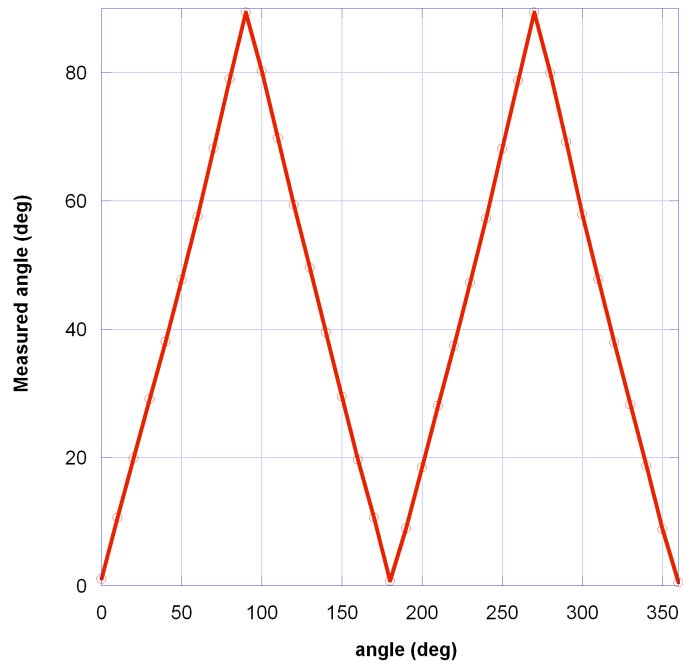
Figure 5.16: Transfer characteristic of the sensor for 1 MHz scanning frequency and 118 mT DC magnetic field
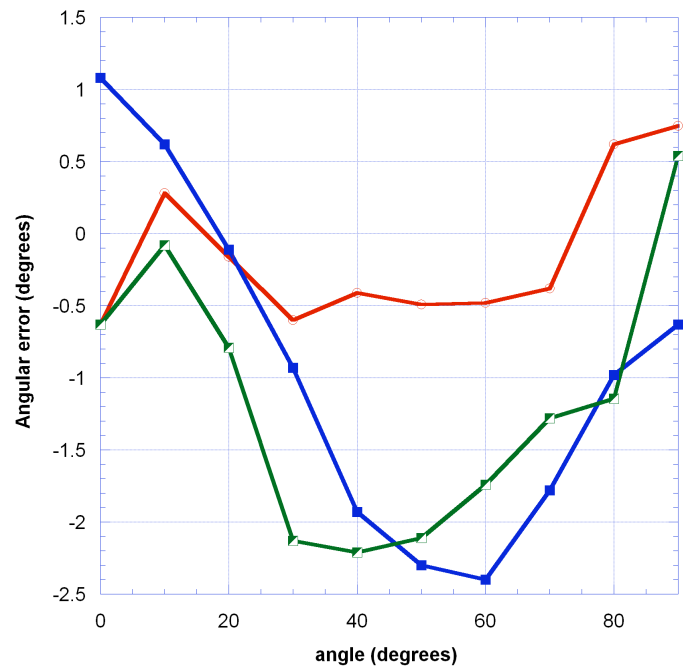
Figure 5.17: Absolute angular error for three samples for 1 MHz scanning frequency and 118 mT DC magnetic field

	[61]	[32]	Version 1	Version 2
Technology	VHT + CMOS	CMOS	CMOS	CMOS
Bandwidth	1.2 MHz	200 Hz	300 kHz	500 kHz
Measurement range ($^{\circ}$)	0 - 360	0 - 360	0 - 90	0 - 90
Resolution, σ ($^{\circ}$)	/	/	1	0.15
Angular error ($^{\circ}$)	$\pm$ 4	$\pm$ 2	$\pm$ 4	$\pm$ 1.5

Table 5.2: Performance comparison of the high bandwidth CMOS angular sensors based on vertical Hall devices

the measurement range of the Version 1 and Version 2 can be extended by replacing the XOR phase detector by a more performant one.

5.4 Comparison of the angular sensor topologies

In Table 5.3 are compared the characteristic performances of the 2D magnetometer used as an angular sensor with two versions of the high speed magnetic angular sensors described in this Chapter. The angular sensors are compared with respect to the design of the front end and its limitations to the sensor's bandwidth, as well as with respect to the system level topology and its limitations to the maximum bandwidth.

The 2D magnetometer utilizes the phase sensitive detection to obtain the components of the in-plane magnetic induction vector, Fig. 4.2. On the front end level, it is the large capacitance of the input preamplifier that limits the maximum spinning frequency, as described in Solution 1, Chapter 3. Speaking of the system level topology, the increase of the spinning frequency invariably leads to the increase of the phase shift introduced by the preamplifier, as in any chopper amplifier topology (as discussed in Chapter 1). Since the demodulation switches are synchronized with the spinning switches (modulation blocks), this phase shift is mistaken for the angle and leads to an angular error. As mentioned in the Section 5.1, this system level topology requires additional arctg function to obtain the angle of the magnetic induction vector.

In contrast to the 2D magnetometer, the differential system level topology of the high speed magnetic angular sensors, Version 1 and Version 2, offers cancellation of the phase shift introduced by the signal conditioning electronics. The improved front end of the Version 2, consisting of the array of the 8CVHDs with clockwise and counterclockwise spinning current method, allows for the highest spinning frequencies and bandwidth.

5.5 Conclusions and outlook

We demonstrated feasibility of a high speed CMOS integrated magnetic angle sensor based on the eight contact vertical Hall device (8CVHD) with spinning current method applied. The novel concept of the sensor features two signal channels with two 8CVHDs carrying the information on

front-end	system topology	device-interface electronics	System BW (kHz)	Main features
8CVHD	phase sensitive detection	$C_2 \gg C_1$ $f_{scanMAX} = 120$ kHz	60	- phase shift at high frequencies - limits BW
two 8CVHDs	differential angular sensor	$C_2 \approx C_1$ guard-band $f_{scanMAX} = 1$ MHz	300	-phase shift at high frequencies cancelled
two arrays of 8CVHDs	differential angular sensor	$C_1 \gg C_2$ clkwise and cclkwise spinning current $f_{scanMAX} = 5$ MHz	500	- best spikes cancellation -best angular accuracy

Table 5.3: Comparison of the angular sensor topologies described in this work

the measured angle in the opposite phases. The use of two devices doubles the sensitivity of the sensor. The quasi-differential structure of the sensor makes it robust to secondary influences. They are translated into "common-mode" disturbances and cancelled out on the system level. The concept together with optimized interface and signal conditioning electronics allows for dramatic increase of the sensor's bandwidth while retaining absolute accuracy and angle resolution comparable to low bandwidth sensors.

The average angular error in the first implementation with one 8CVHD per channel is $\pm$ 4º. The measurement results have shown that the sensor tracks the angle of the in-plane magnetic vector oscillating at 200 kHz, or equivalently 12 000 000 rpm.

The absolute angular error was reduced in the second implementation down to an average $\pm$ 1.5º. The bandwidth of the sensor was increased to about 500 kHz.

The limited measurement range 0-90º can be extended by using a more performant phase detector instead of a simple XOR gate. The use of an SR flip-flop [73] with the transfer characteristics periodical in 2π would extend the measurement range to 0-180º. The use of a sequential logic phase detector [74] having the transfer characteristics periodical in 4π would give a full range 0-360º angular sensor.

Chapter 6

Open-loop current transducer based on the 8CVHD

In this chapter we investigate feasibility of building a high-bandwidth CMOS integrated magnetic sensor based on the 8CVHD for use in open-loop current transducers. State-of-the-art open-loop current transducers dominantly contain magnetic sensors based on horizontal Hall devices. We use a new concept of the current transducer where a magnetic sensor is placed directly on the current carrying conductor. This is why a vertical Hall device is needed as a sensing device in this design.

In addition, open-loop current transducers require magnetic sensors with low temperature cross-sensitivity. Different calibration and auto-calibration techniques are implemented to reduce sensitivity and offset drift of the magnetic sensors with horizontal Hall devices. We examine a novel system level topology and its efficiency to eliminating sensitivity drift with temperature of the magnetic sensor based on the 8CVHD.

Lastly, we want to use the features of the 8CVHD as well as system level concept to extend bandwidth and dynamic range of the open-loop current transducer.

6.1   Introduction

Almost all current transducers offered on the market are based on measurement of magnetic field produced by measured current, also referred to as the primary current. The current transducers based on Hall devices can be divided in two groups [75] depending on the way the primary current is measured:

a. Open-loop current transducers, the principle schematics of which is shown in Fig 6.1. The magnetic flux created by a measured current is concentrated in a magnetic core. The magnetic core has a gap in which a Hall device is placed. The output of a Hall sensor, proportional to the measured field, is processed to provide an exact representation of the primary current. These transducers usually have a bandwidth from DC to several tens of kHz. However, they have low accuracy and are used in cases when measurement error can be well higher than 1%.
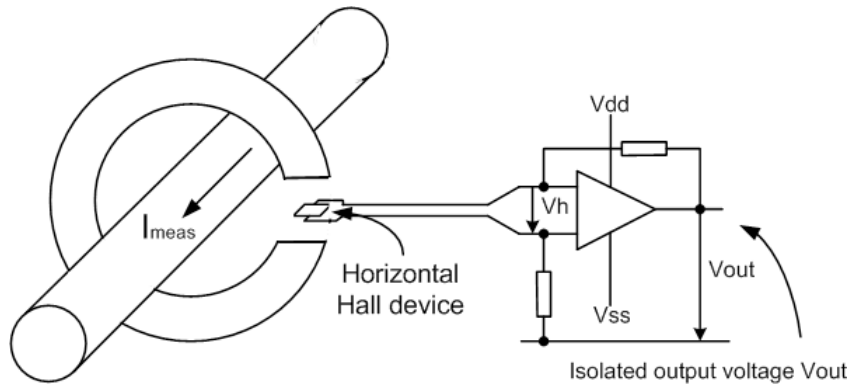
Figure 6.1: Open-loop current transducer
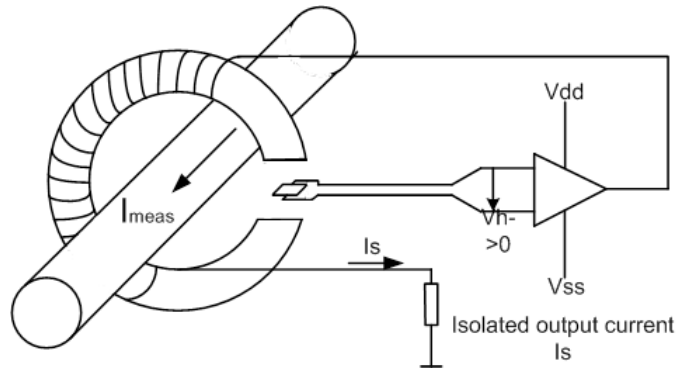
Figure 6.2: Closed-loop current transducer

b. Closed-loop current transducers shown in Fig. 6.2. The magnetic flux of a measured current is compensated by the magnetic flux produced by a current in the secondary coil. The secondary coil is wound around a magnetic core. The compensation current is controlled by the resultant flux sensed by a Hall magnetic sensor, Fig. 6.2. Due to the magnetic negative feedback, the output does not depend on the characteristics of a Hall sensor, to the first approximation. The vast majority of current transducers found in practice today belong to closed-loop current transducers. Their accuracy is usually in the range 0.1 to 1%. Generally, they are low-cost transducers, but at high currents (above 1000 A), they tend to be much more expensive than the open-loop ones.

The magnetic core, usually of ferromagnetic material, brings about a number of parasitic effects, such as non-linearity and hysteresis in the transfer curve, Eddy-current losses, etc. The concept of the current transducers without magnetic core, Fig. 6.3, was patented recently [76]. It can be used in both open-loop and closed-loop configurations. Magnetic sensor is placed directly onto the surface of the conductor through which the measured current is passed, usually referred to as the bus bar. Since the measured magnetic field is horizontal, a Hall device must be a vertical one. Current density through the bus bar must be high in order to generate substantial field at the position of the magnetic sensor. A high-resolution magnetic sensor must be placed as close as possible to the

94
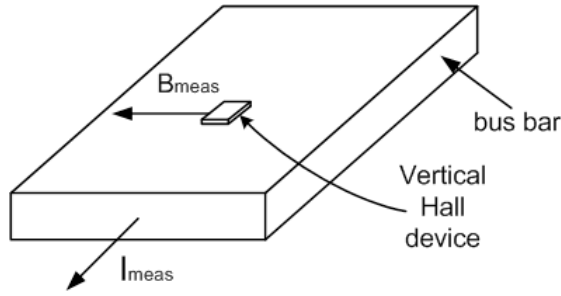
Figure 6.3: Current transducer without magnetic core

surface of the current conductor where the magnetic field is the highest.

Magnetic sensors suffer from sensitivity drift due to temperature, packaging stress, aging, and thermal shocks. The sensitivity drift of uncalibrated Hall sensors available on market ranges from 0.05 %/K to 0.1 %/K. Several approaches to tackling the problem of sensitivity drift due to these influences were reported, among which [77, 29, 78, 30, 15]. It should be noted here that these approaches are uniquely dedicated to calibration of sensitivity drift in the sensors based on horizontal Hall devices. They have in common the use of an integrated coil, or integrated coils, supplied by a reference current in order to create a reference magnetic field. In all solutions the reference magnetic field was supposed temperature insensitive. However, the reference current is usually created as a current through a resistor supplied with a voltage reference. The voltage reference is constant, but the resistance changes with temperature which leads to the change of the reference field.

The Hall device senses both the measured and reference fields. The reference magnetic field is much lower than the measured field. This is why it is difficult to measure it selectively in the total signal. In each solution mentioned above different strategies were proposed to distinguish between the two fields. For instance, frequency separation was employed in [78] where the frequency of the reference field was outside the sensor's operating frequency bandwidth. In [15] spatial coding of the reference and measured fields in a sensor array was introduced. The reference field has opposite direction on each pair of the sensor array whereas the measured field remains in the same direction. In all proposed solutions, signal proportional to the reference field is then compared with a reference voltage in a comparator circuit. The output of a comparator circuit then serves as a feedback signal to close the loop of conventional automatic gain control. The best solutions report stabilization of sensitivity drift in the laboratory environment down to 0.003 %/K [16].

As mentioned above, the structure of the current transducer shown in Fig. 6.3 requires a vertical Hall device and as such is compatible with the 8CVHD. This is why we have chosen it to study the feasibility of using the 8CVHD in current sensing. In addition, we investigate the possibility to reduce the sensitivity drift of the 8CVHD by employing a novel system level concept. We describe the concept in the following Section.

6.2 Concept of the current transducer based on the 8CVHD

The current transducer consists of the primary conductor in the form of a bus bar, as sketched in Fig. 6.4a), and the Hall magnetic sensor placed on top of it [69]. The bus bar is a slab with a smaller cross-section at the position of the sensor in order to increase current density and magnetic field of the measured current. The magnetic field of the measured current, B_{meas}, is perpendicular to the measured current's flow. An external coil serving as a reference coil to create reference magnetic field, B_{ref}, is placed on top of the magnetic sensor. It is supplied by the on-chip reference current source whose value drifts with temperature. The field B_{ref} is collinear with the measured current's flow. The CMOS integrated magnetic sensor, Fig. 6.4b), consists of:

- A high-speed magnetic angle sensor with the 8CVHD as the sensing device. The front end of the sensor is described in Chapter 3, Solution 3, while its block diagram and measured results are shown in Chapter 5, Section 5.3.1. An additional digital module for sign detection was added to extend the measurement range to $\pm$ 90$^{\mathrm{o}}$. It is based on detection of the leading or lagging edges of the inputs to the comparators. The function of the angle sensor is to measure the angle α between the reference magnetic field, B_{ref}, created by an external coil and the resultant magnetic field B_{res}. The resultant magnetic field B_{res} is equal to the vector sum of the reference and measured current's fields. The angle enclosed between B_{res} and B_{ref} changes with temperature due to temperature cross-sensitivity of the reference current source. The angular sensor outputs the angle between the total magnetic field B_{res} and the reference field B_{ref}. Assuming ideal characteristics of the magnetic angle sensor, the measured angle is independent of the sensitivity and offset drifts of the 8CVHDs.

- A tangent converter. It is a nonlinear integrator dedicated to conversion of the PWM signal proportional to the measured angle α into tgα. Thus, the output voltage of the tangent converter is proportional to the measured magnetic field, B_{meas}, and inversely proportional to the reference magnetic field B_{ref}. The tangent converter is designed such that it compensates the change of the angle α due to temperature sensitivity of the reference magnetic field B_{ref}. This was achieved by using the same reference voltage and the same type resistors employed in the design of the reference current source. Finally, the output of the magnetic sensor is a temperature insensitive voltage proportional to the measured current.

- A reference current source. It was designed as a current delivered by the reference voltage through an on-chip resistor. Its value drifts with temperature due to the resistor's drift with temperature (the resistor has a positive temperature coefficient). Thus, the reference field decreases with temperature.
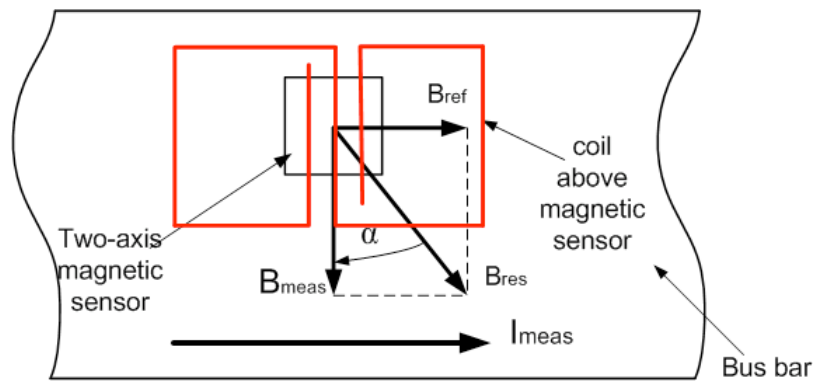
(a) The narrow part of the bus bar (see Fig. 6.13) and magnetic angle sensor with the 8CVHD as the sensing device
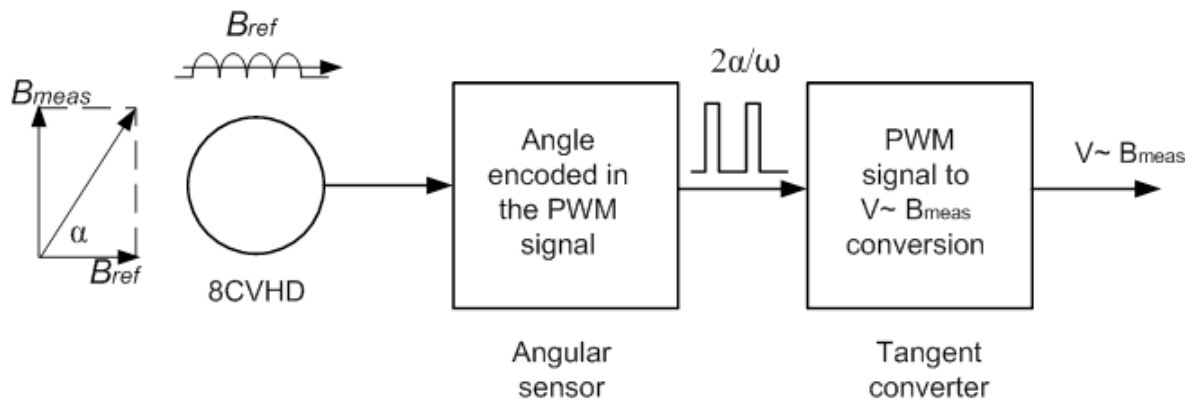
(b) Concept of the magnetic sensor based on the 8CVHD

Figure 6.4: Concept of the current transducer
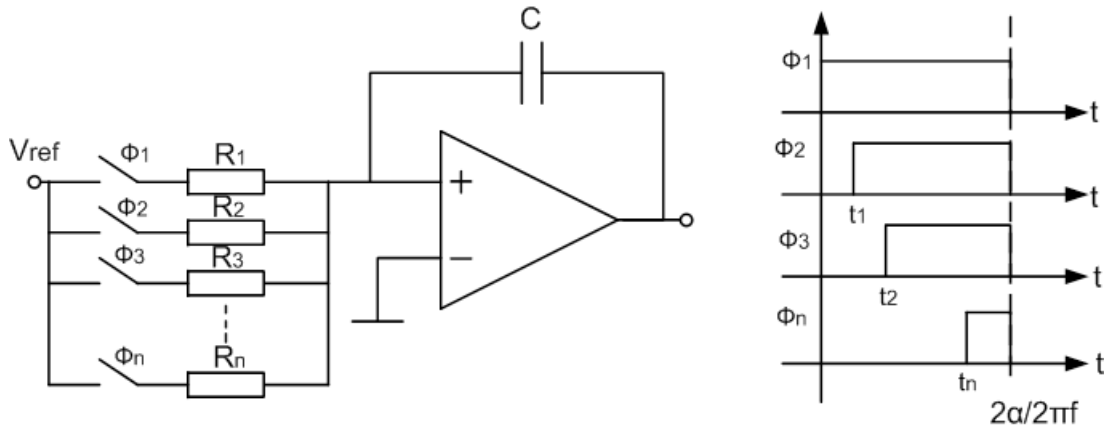
(a) Sequential closing of the switches reduces resistance and leads to nonlinear integration
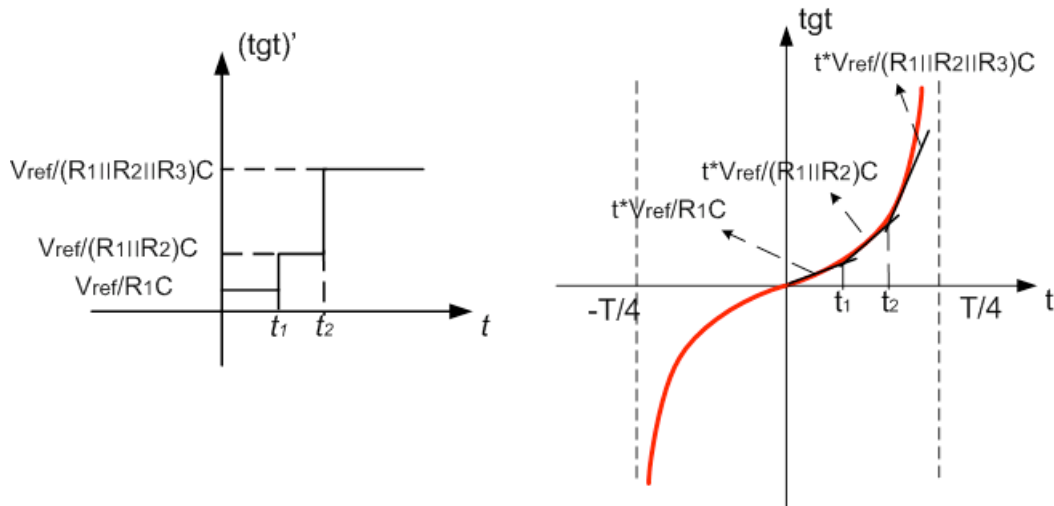
(b) Approximation of the tangent function

Figure 6.5: Tangent converter

6.2.1 Tangent converter

Tangent converter was designed by [79]. It is essentially a nonlinear integrator acting as a phase demodulator in the system.

The operation of the tangent converter and approximation of the tangent function is depicted in Fig. 6.5.

The output of the angle sensor is the PWM pulse proportional to $\alpha/(\pi f_{\mathrm{scan}})$. In the ideal case it is not temperature dependent. It is denoted as ϕ_1 in Fig. 6.5, and serves as the control signal for the beginning and end of the nonlinear integration. The idea here is to approximate function tgα in the following way:

- the control signal ϕ_1 is divided in intervals of equal duration corresponding to the period of the clock frequency. The clock frequency for the tangent converter is $f_{\mathrm{clock}} = 64 f_{scan}$;

- the first derivative of the tangent function is calculated for each interval. The derivative of the function is implemented as a current through the resistors shown in Fig. 6.5b). The sequential switching on of the switches ϕ_1-ϕ_n , Fig. 6.5 a) and b), reduces the equivalent resistance and thus increases the first derivative;

- the first derivative over corresponding interval is integrated to obtain a linear function. This linear function approximates function $tg\alpha$ in the interval in question. This method is known as piecewise linear approximation. The voltage on the capacitor C is the integral of the current through it and is proportional to $tg\alpha$, Fig. 6.5 b).

The voltage on the capacitor C can be expressed as:

$$U_C = \int_0^{\frac{\alpha}{\pi f_{scan}}} (tgt)' \, dt =$$

$$= \frac{1}{C} \left(\int_0^{\frac{\alpha}{\pi f_{scan}}} \frac{V_{ref}}{R_1} dt + \int_{t_1}^{\frac{\alpha}{\pi f_{scan}}} \frac{V_{ref}}{R_1 \parallel R_2} dt + ... + \int_{t_n}^{\frac{\alpha}{\pi f_{scan}}} \frac{V_{ref}}{R_1 \parallel R_2 ... \parallel R_{n+1}} dt \right). \tag{6.1}$$

The integration starts at the rising edge of the PWM pulse from the angular sensor. The time intervals t_1 to t_n are determined by the clock frequency and can be written as:

$$t_i = \frac{i}{64 f_{scan}}, \tag{6.2}$$

where $i=1, ..., n$. The resistances R_2 to R_n can be expressed with respect to a reference resistance R_1 as:

$$R_n = c_n R_1, \tag{6.3}$$

where c_1 to c_n are real numbers.

Substituting Eqns 6.2 and 6.3 in Eqn 6.1 yields:

$$U_C = \frac{V_{ref}}{R_1 C f_{scan}} \left(\frac{\alpha}{\pi} + \frac{c_1 + c_2}{c_2} \left(\frac{\alpha}{\pi} - \frac{1}{64} \right) + ... + \frac{c_1 + c_2 + ... + c_{n+1}}{c_2 ... c_{n+1}} \left(\frac{\alpha}{\pi} - \frac{n}{64} \right) \right), \tag{6.4}$$

where the expression in the bracket is the linear piecewise approximation of the function $tg\alpha$:

$$U_C = \frac{V_{ref}}{R_1 C f_{scan}} tg\alpha, \tag{6.5}$$

where V_{ref} is the reference voltage, R_1 is the resistance in the branch closed during the whole PWM pulse, and f_{scan} is the scanning frequency. The $tg\alpha$ depends only on coefficients c_1 to c_n and is temperature independent. The product $V_{ref}/(R_1 C f_{scan})$ is the temperature dependent scaling factor of the tangent function.

The process of $tg\alpha$ approximation is not an instantaneous one. The integrator needs to be followed by a simple sample-and-hold circuit, as shown in Fig. 6.6 a). Initially all switches ϕ_1-ϕ_n are open and the capacitor C is discharged. With the rising edge of the incoming PWM pulse ϕ_1 is closed and the integration starts (ϕ_empty is open). After maximum one period of the main clock the switch ϕ_2 is closed, after the second period of the main clock the switch ϕ_3 is closed, and so on. With the falling edge of the PWM pulse all switches ϕ_1-ϕ_n are open and the integration stops. In the pause before the arrival of the next PWM pulse, the switch ϕ_{out} is closed and the output voltage of the integrator is transferred to the hold capacitor C, Fig. 6.6 b). The switch ϕ_{empty} is closed to discharge the integrating capacitor C. The sign detector added to the tangent converter and angular sensor controls the polarity of the reference voltage in order to enable measurements of the positive and negative angles in the range $\pm\ 90^\mathrm{o}$.

The reference current source gives the reference current for the reference coil:

$$I_{ref} = \frac{V_{ref}}{R_{ref}},\tag{6.6}$$

where V_{ref} is the reference voltage used in the integrator shown above, and R_{ref} is the on-chip resistance of the same type as R_1.

The $tg\alpha$, Fig. 6.4, is given by:

$$tg\alpha = \frac{B_{meas}}{B_{ref}} = \frac{k_b I_{meas}}{k_c I_{ref}} = \frac{k_b}{k_c}\frac{R_{ref}}{V_{ref}}I_{meas},\tag{6.7}$$

where k_b and k_c are coefficients depending on vacuum magnetic permittivity and the geometries of the bus bar and coil, respectively.

Substituting Eqn 6.7 into Eqn 6.5 yields for the output of the tangent converter:

$$V_{out} = U_C \approx \frac{R_{ref}}{R_1 C f_{scan}}\frac{k_b}{k_c}I_{meas}.\tag{6.8}$$

Since the resistances R_{ref} and R_1 are the same type, their drift with temperature cancels out. The drift of the integrating and sampling capacitances with temperature can be neglected. The temperature drift of the coefficients k_b and k_c can also be neglected. Assuming the ideal angular sensor and constant clock frequency, the output voltage V_out does not depend on the sensitivity drift of the 8CVHD. As in all other solutions, the buffer's offset is neglected since it can be compensated in the laboratory environment.

6.3 Analysis of nonidealities of the magnetic sensor

The above analysis was performed assuming the ideal performance characteristics of the angular sensor and the tangent converter. We discuss below some nonidealities and maximum bandwidth of the magnetic sensor.
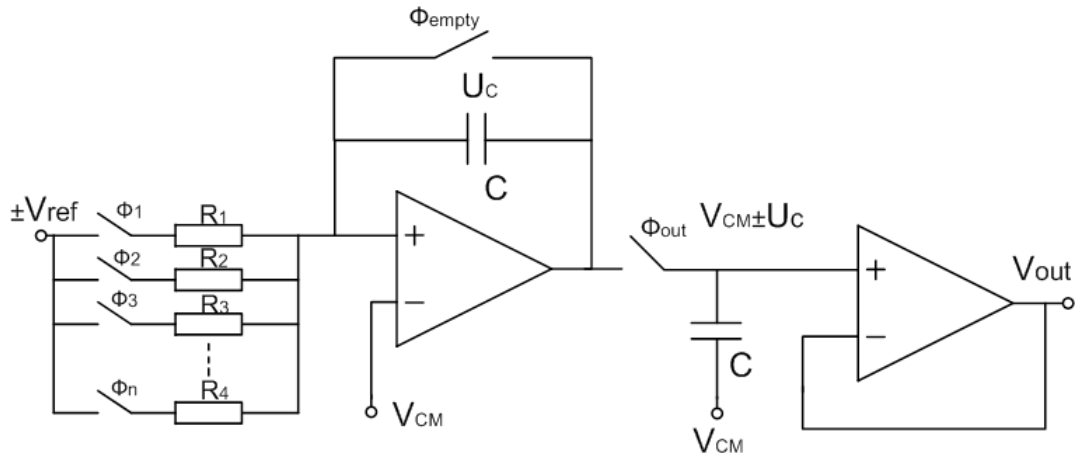
(a) Nonlinear integrator and a sample-and-hold buffer
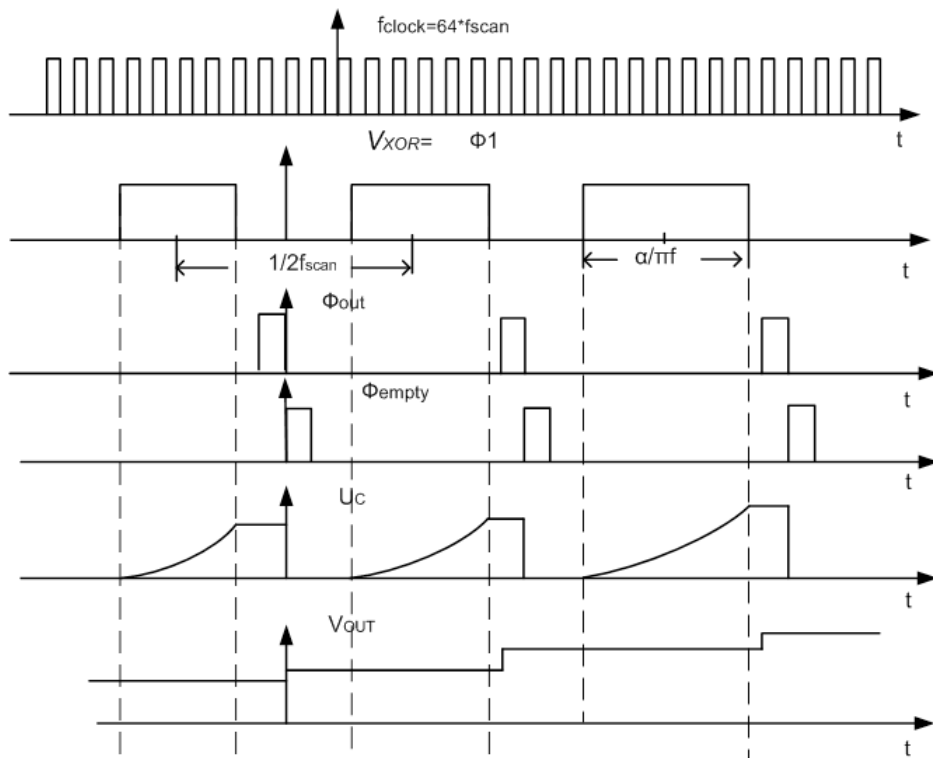
(b) Control and signal waveforms

Figure 6.6: Block-diagram of the tangent converter
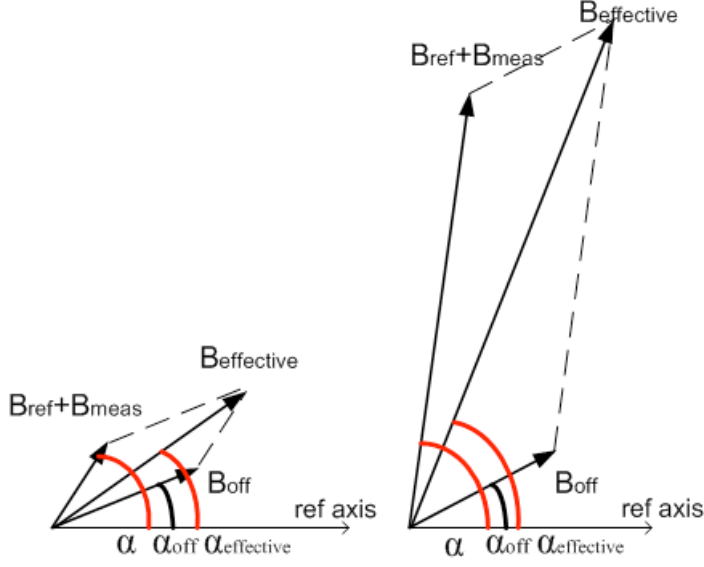
Figure 6.7: The offset equivalent magnetic field vector causes an error in the measured angle. The error depends on the ratio of the magnitudes of the applied and offset equivalent magnetic fields

6.3.1 Temperature dependence of the angular sensor

According to Eqns. 5.12 and 5.13 the first harmonic of the offset voltage causes an angle dependent error. The first harmonic of the offset voltage can be expressed by the offset equivalent mangetic field to be:

$$V_{off} = I_{bias} S_0 B_{off}. \tag{6.9}$$

Then by rearranging Eqn 5.12, the phase shift in the clockwise channel can be expressed as:

$$\alpha_c = arctg \frac{B_{res} \sin \alpha + B_{offc} \sin \alpha_{offc}}{B_{res} \cos \alpha + B_{offc} \cos \alpha_{offc}}, \tag{6.10}$$

where B_{res} is the magnitude of the total in-plane field, α is the physical angle enclosed between B_{res} and the reference axis, B_{offc} is the magnitude of the offset equivalent magnetic field vector in the clockwise channel, α_{offc} is its phase, and α_{c} is the phase shift in the clockwise channel. Similarly, the phase shift in the counterclockwise channel can be expressed as:

$$\alpha_{cc} = -arctg \frac{B_{res} \sin \alpha + B_{offcc} \sin \alpha_{offcc}}{B_{res} \cos \alpha + B_{offcc} \cos \alpha_{offcc}}. \tag{6.11}$$

These equations suggest that the higher the ratio of $B_{\text{res}}/B_{\text{offc}}$, the smaller is the angular error, as sketched in Fig. 6.7.

The offset equivalent vectors in the two channels have arbitrary magnitude and phase. As a result, their influence on the angular reading does not cancel out.
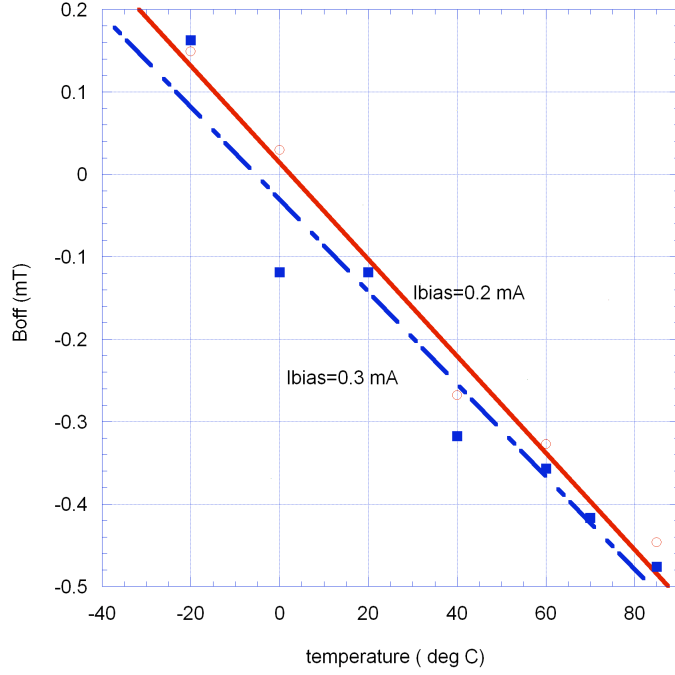
Figure 6.8: First harmonic of the 8CVHD's offset voltage versus temperature

The first harmonic of the residual offset of the 8CVHD drifts with temperature, as shown in Fig. 6.8. The temperature drift of the 8CVHD was found to be about 7 μT/ $^{\mathrm{o}}$C. Taking into account the temperature drift of the offset vector, Eqn 6.10 can be rewritten to be:

$$\alpha_c\left(T\right) = arctg \frac{B_{res}\sin\alpha + B_{offc}(1 - TC_{off}\triangle T)\sin\alpha_{offc}}{B_{res}\cos\alpha + B_{offc}(1 - TC_{off}\triangle T)\cos\alpha_{offc}}, \tag{6.12}$$

where TC_{off} is the temperature coefficient of the first harmonic of the 8CVHD, and T and $\triangle T$ are absolute temperature and temperature difference, respectively. If the total field B_{res} is large enough, the offset field and its drift with temperature cause a negligible error.

In the ideal case, the signal conditioning electronics in the two channels is assumed matched. Any mismatch either in gain or phase shift of the analog blocks is temperature dependent and is only partially cancelled on the system level.

6.3.2 Mismatch equivalent magnetic field of the angular sensor

The mismatch of the first harmonic of the offset voltages in the two channels together with the channels mismatches can be modeled by the "mismatch" equivalent magnetic field. The field super-imposes on the applied magnetic field causing an erroneous angle reading, similar to the sketch in Fig. 6.7. In Fig. 6.9 is shown the measured angle versus applied angle for one sample. The DC magnetic field was swept from 3.6 mT to 83 mT, the angular sensor was rotated over 90$^{\mathrm{o}}$ and its output was recorded. For smaller fields the increment of the measured angle is nonlinear. The angle

103
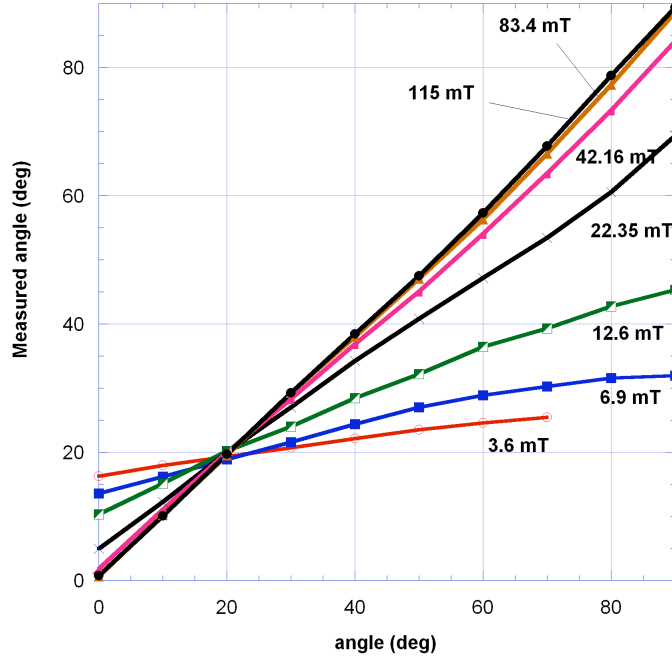
Figure 6.9: Measured angle of the angular sensor (f_{scan}=1 MHz) versus applied angle for DC magnetic field swept from 3.6 mT to 115 mT

increment is linear starting from 22.35 mT onwards. The linearity of the angle increment is crucial for the magnetic sensor.

However, the output of the angular sensor is not proportional to 2α for low magnetic fields. It can be expressed as having the "gain" dependent on the magnetic field:

$$PWM \sim k(B)\frac{2\alpha}{2\pi f_{scan}}. \tag{6.13}$$

The illustration of the "gain" for 1 MHz and 200 kHz scanning frequencies on the same die is given in Fig. 6.10. The gain "1" stands for the angular sensor's output proportional to 2α. The only difference between these two variants is the bandpass filter. Fig. 6.10 suggests that channels are better matched at 1 MHz.

6.3.3   Tangent converter

The maximum absolute angle for which the tangent converter operates with a negligible error is 60º. The tangent converter saturates for all B_{res} enclosing an angle greater than 60º with the reference axis. This means that for a given reference field, B_{ref}, the maximum magnitude of the measured field must be: $B_{measmax} = 1.73B_{\text{ref}}$.

The switching on of the second switch ϕ_2 depends on the phase shift between the rising edge of the PWM pulse and the first rising edge of the clock signal. The maximum delay between the two is one period of the clock signal.

104
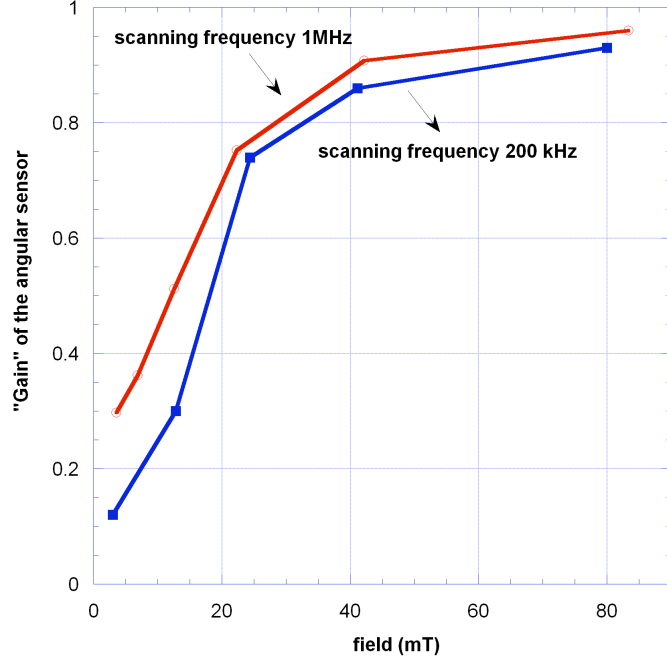
Figure 6.10: "Gain" of the angular sensor for 1 MHz and 200 kHz scanning frequencies

6.3.4 Maximum bandwidth

For the AC fields, the angular sensor up to the comparators, Fig. 5.3, can be modeled as a system carrying a phase modulated (PM) signal. The critical feature of these systems is their bandwidth. In theory, PM signals require an infinite bandwidth to avoid any signal distortion during transmission. The output of the bandpass filter can be written as (neglecting the intrinsic phase shift for simplicity):

$$V_{cBP} = AS_0 B_{res} I_{bias} \cos\left(2\pi f_{scan}t - arctg\left(\frac{B_{measm}}{B_{ref}}\sin(2\pi f_{AC}t)\right)\right), \qquad (6.14)$$

where the measured field is assumed sinusoidal $B_{meas} = B_{measm}\sin(2\pi f_{AC}t)$.

In order to estimate the minimum required bandwidth for the targeted maximum frequency f_{AC}, the arctg function is approximated by its linear term:

$$V_{cBP} \approx AS_0 B_{res} I_{bias} \cos\left(2\pi f_{scan}t - \frac{B_{measm}}{B_{ref}}\sin(2\pi f_{AC}t)\right). \qquad (6.15)$$

The following analysis is only approximate due to the approximation of the arctg function by its linear term. The phase modulated signal in Eqn 6.15 is characterized by the instantaneous phase and instantaneous frequency, respectively:

$$\phi_i = 2\pi f_{scan}t - \frac{B_{measm}}{B_{ref}}\sin(2\pi f_{AC}t), \qquad (6.16)$$

$$f_i = \frac{1}{2\pi}\frac{d\phi_i}{dt} = f_{scan} - f_{AC}\frac{B_{measm}}{B_{ref}}\cos(2\pi f_{AC}t). \qquad (6.17)$$

According to the terminology used in analysis of PM systems, the carrier frequency is the scanning frequency, while the peak frequency deviation and the modulation index are as follows, respectively:

$$\triangle f = f_{AC} \frac{B_{measm}}{B_{ref}}, \tag{6.18}$$

$$m = \frac{\triangle f}{f_{AC}} = \frac{B_{measm}}{B_{ref}} \mid_{max} = 1.73, \tag{6.19}$$

where modulation index m is calculated for the angular limitation imposed by the tangent converter. This is at the same time the greatest modulation index for the system.

The frequency spectrum of the phase modulated signal has spectral components at all frequencies, $f_{scan} \pm nf_{AC}$, where n can be any integer from $-\infty$ to $+\infty$. The minimum practical bandwidth for the signal transmission without distortion is defined by the Carlson's rule:

$$BW = 2f_{AC}(1 + m) = 5.46f_{AC}. \tag{6.20}$$

The 3dB bandwidth of the bandpass filter in the angular sensor must satisfy the Carlson's rule. The above is the most severe requirement for the angular sensor's bandwidth. For the modulation index m =1, which is equivalent to $B_{measm} = B_{ref}$ the required bandwidth is $BW = 4f_{AC}$. In Chapter 5 was shown that the required bandwidth is only $2f_{AC}$ for a small modulation index, or equivalently $B_{measm} \ll B_{ref}$.

In Chapter 3, Section 3.2.5, were given the limitations to the sensor's bandwidth imposed by the front end. The Carlson's rule together with the designed passband of the bandpass filter is a more severe criterion. The design of the passband of the bandpass filter is a trade-off between the accuracy and bandwidth. The smaller the passband, the better the spikes' residues affecting accuracy will be filtered out. On the other hand, reduction of the passband leads to a reduced bandwidth.

6.4   Measurement results for the magnetic sensor

The magnetic sensor was fabricated in 3.3 V 0.35 μm AMS high voltage technology. The chip microphotograph is shown in Fig. 6.11.

The sensor was exposed to a rotating DC magnetic field vector of 80 mT. The output of the sensor in this case is a tangent function of the angle enclosed between the magnetic vector and the reference axis. In Fig. 6.12 is shown the normalized difference between the output of the sensor and the calculated tangent function.
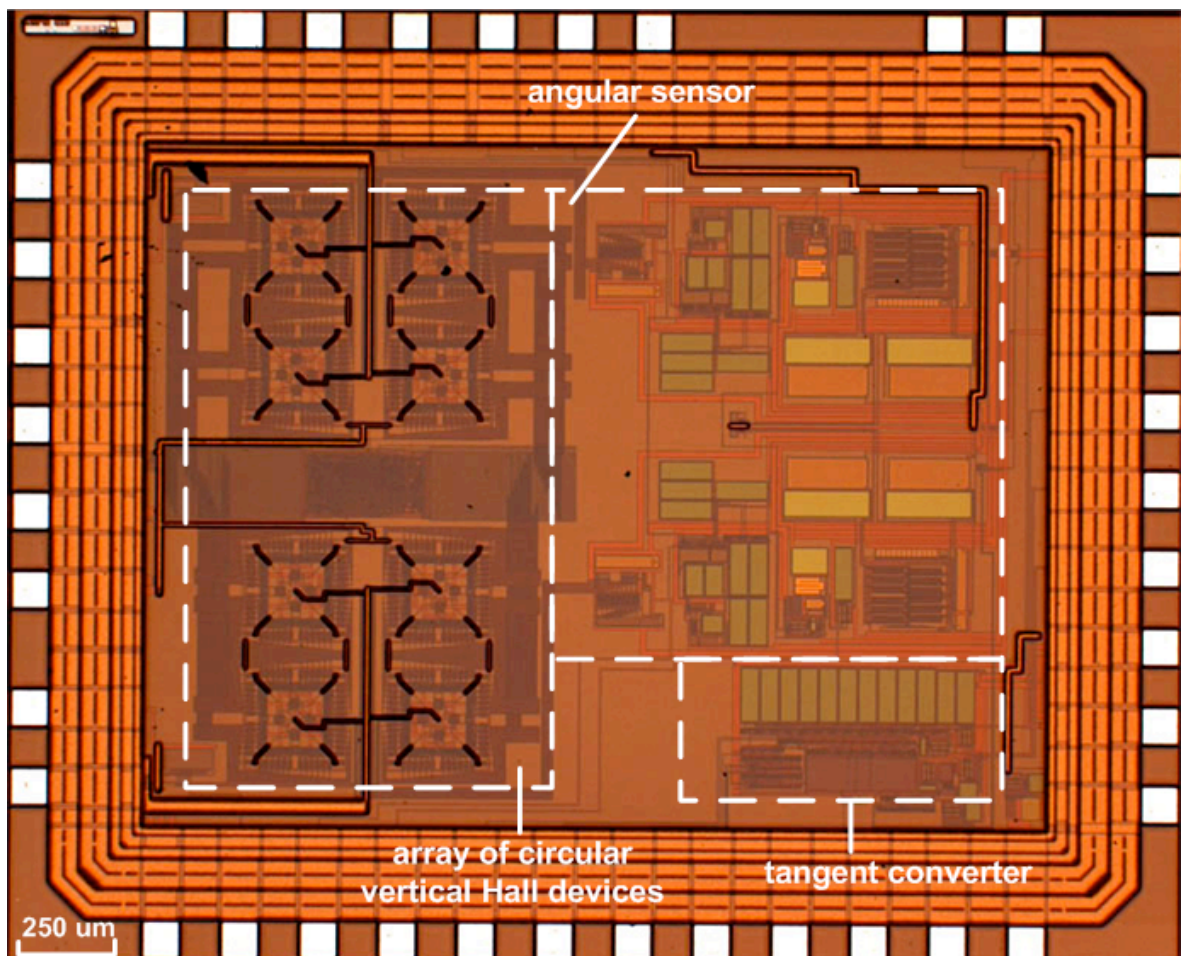
Figure 6.11: Microphotograph of the magnetic sensor. The angular sensor contains an array of four 8CVHDs in the front end (the Version 2 described in Section 5.3)
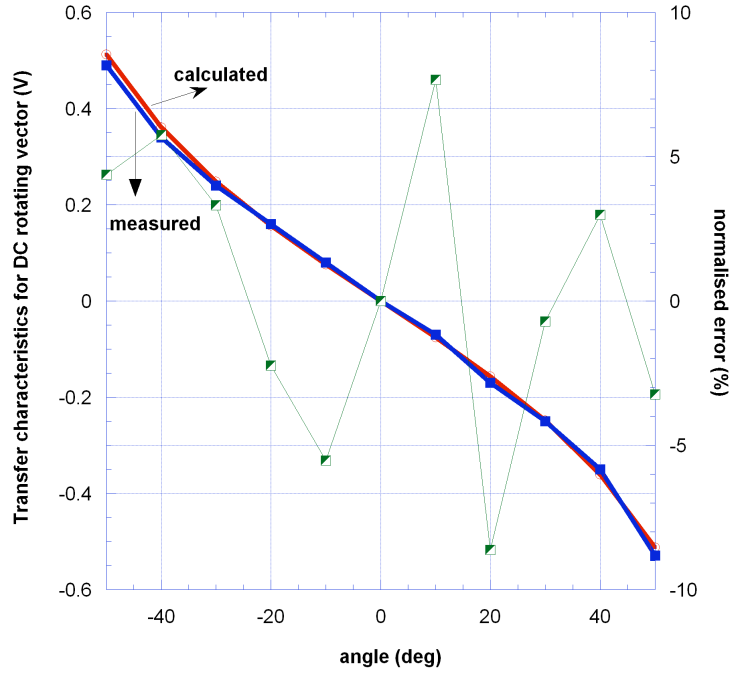
Figure 6.12: Output of the magnetic sensor vs. calculated tangent function for $f_{\text{scan}}= 1$ MHz and 80 mT rotating DC magnetic field

6.5   Measurement results for the current transducer

We show the initial measurements aimed at the characterization of the current transducer.

The die was glued to the non-magnetic PCB and protected by epoxy. The coil was placed on top of the protection and supplied by the on-chip reference current. Its nominal value is 10 mA. In some experiments, the reference coil was replaced by the DC magnet.

The PCB was placed on the bus bar. The bus bar was designed by [80]. It has a narrow part to increase the magnetic field at the position of the sensor. The photograph of the test current transducer is given in Fig. 6.13. Special care was taken to align the sensor's axis with the bus bar's one, as well as to align the coil's axis with the sensor's axis.

As pointed out in Chapter 5, the magnetic sensor was designed for two scanning frequencies: 1 MHz and 200 kHz. The differences on the system level are: the center frequency and the passband of the bandpass filter, as well as the gain in the tangent converter. The switch from one scanning frequency to another one on the same die is regulated by a control pin.

The current transducers were tested for linearity, sensitivity drift with temperature, AC behavior and transient response.

The coefficient k_{b} of the bus bar, Eqn 6.8, is $k_b = 2.57 \cdot 10^{-5}$ T/A. The sensitivities of the magnetic sensor, S in V/T, and the current transducer, S_{ct} in V/A, are related by this coefficient:
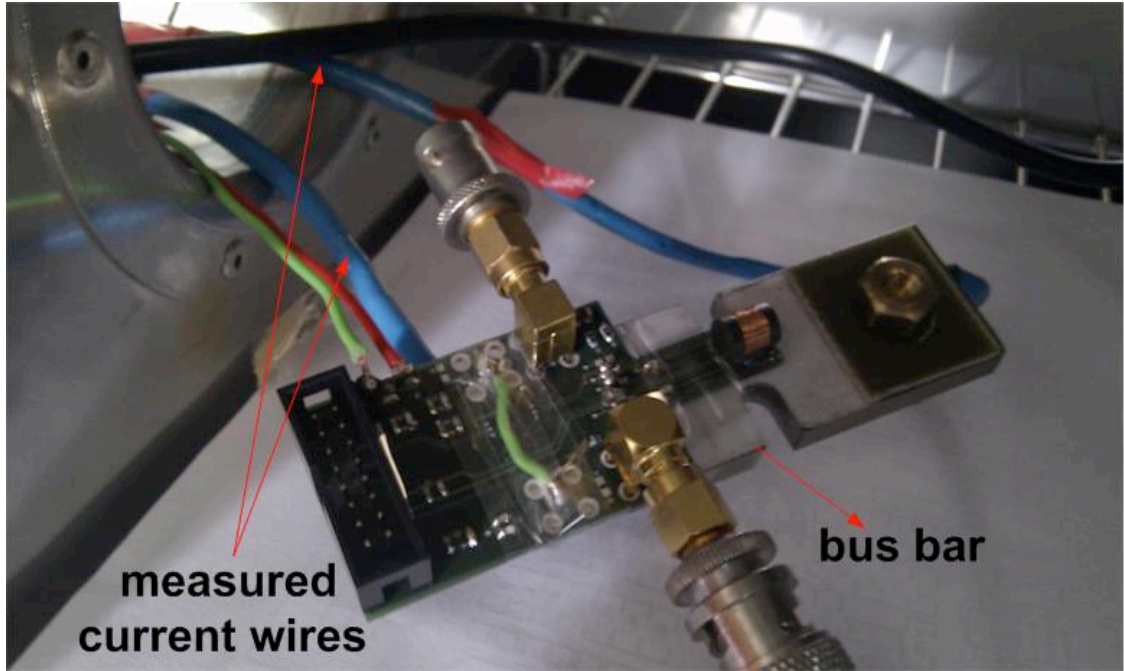
Figure 6.13: Current transducer in the temperature chamber. Magnetic sensor is placed directly on the bus bar. The coil for reference field generation is placed on top of the protected die.

$$S_{ct} = k_b S. \qquad (6.21)$$

6.5.1 High bandwidth current transducer

The transfer characteristics of the current transducer with the magnetic sensor operating at 1 MHz scanning frequency is given in Fig. 6.14. The clock signal for the tangent converter was supplied from a quartz oscillator running at 64 MHz. This signal is processed on-chip to give 32 MHz clock frequency, or equivalently the sensing frequency, for the magnetic angular sensor. The offset voltage of the magnetic sensor was externally compensated. The reference field was generated by the coil and is about 2.5 mT at the position of the sensor. The measured current was swept from -200 to 200 A. This corresponds to 5.14 mT for the maximum magnetic field of the measured current. This corresponds to the angle of 63° for 200 A where nonlinearity is the worst 4%. The increase of the reference field would allow a higher dynamic range.

The sensitivity drift with temperature was tested for the reference field created by the coil $B_{\text{ref}}=$ 2.5 mT. The bus bar together with the quartz oscillator was placed in the temperature chamber. The reference voltage V_{ref} was externally supplied. The temperature was swept from -20 to 80 $^{\circ}$ C. The current 200 A was passed through the bus bar and the output voltage was recorded.

The sensitivity drift of the current transducer in the range -20 to 80 $^{\circ}$ C was found to be about 5 %/K. This high sensitivity drift is primarily due to the substantial drift of the first harmonic of
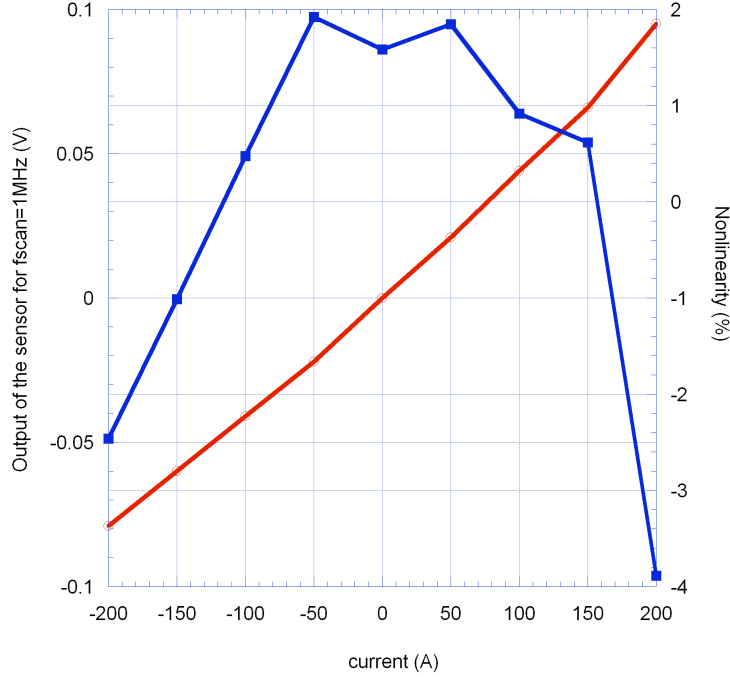
Figure 6.14: Transfer characteristics of the current transducer for f_{scan}= 1 MHz and B_{ref}= 2.5 mT

the offset voltage with temperature, Fig. 6.8 and Eqn 6.12. The maximum value of the reference field is limited by the on-chip current source whose maximum current is 10 mA. This current can be amplified by the off-chip current amplifier and fed into the reference coil to prove the concept. This is left out for future work.

In order to test the transducer's behavior for larger reference fields, we placed a permanent magnet of 60 mT as a reference field. As Eqn 6.12 suggests, the larger the total field, the smaller will be the influence of the drift with temperature of the first harmonics. As an amendment to the concept described in 6.2, Eqn 6.8 can be in this case rewritten to read:

$$V_{out} = U_C = \frac{V_{ref}}{R_1 C f_{scan}} \frac{k_b}{B_{ref}} I_{meas}. \tag{6.22}$$

Assuming the reference voltage V_{ref}, the scanning frequency f_{scan}, and the capacitance C constant, the output voltage of the magnetic sensor is:

$$V_{out} = U_C = \frac{V_{ref}}{C f_{scan} R_1 \left(1 + TC_R\right)} \frac{k_b}{B_{ref} \left(1 + TC_{B_{ref}}\right)} I_{meas}, \tag{6.23}$$

where the temperature coefficients of the resistance R_1 and the permanent magnet are TC_R and TC_{Bref}, respectively. The coefficient TC_R is a positive temperature coefficient of a diffusion resistor. If a permanent magnet with a negative temperature coefficient is chosen, $TC_{Bref} < 0$, the temperature drift of the V_{out} can be greatly reduced. In Fig. 6.15 are shown measurement results in

110
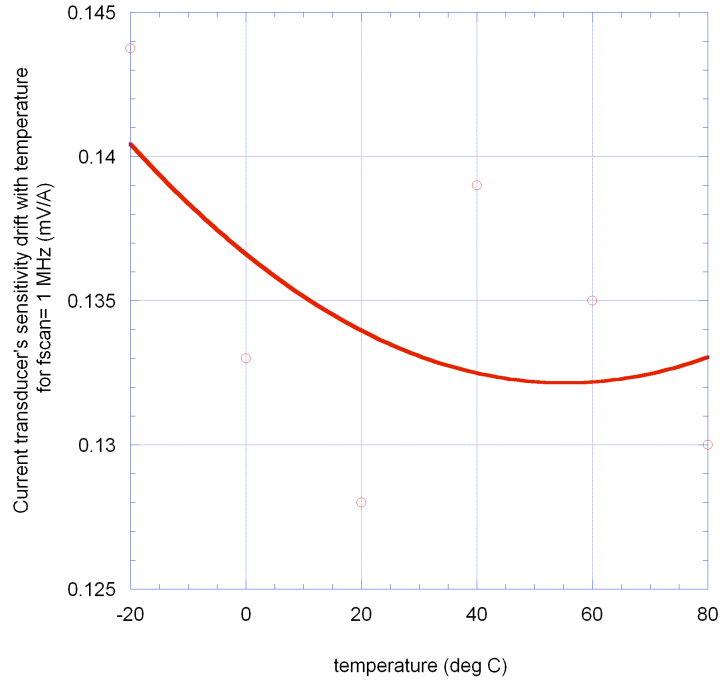
Figure 6.15: Sensitivity vs. temperature of the current transducer for $f_{\text{scan}}=$ 1 MHz and $B_{\text{ref}}=$ 60 mT

which a permanent magnet of 60 mT with a negative temperature coefficient $TC_{Bref}=$ - 0.12 %/K was used. The sensitivity drift was found to be 0.1 %/K.

The scanning frequency of 1 MHz would allow measuring AC fields up to 500 kHz, but in this case it is the bandpass filter in the angular sensor that limits the bandwidth. The bandpass filter has a bandwidth of 350 kHz. The magnitude of the measured and reference fields are 5 mT and 20 mT, respectively. According to Eqn 6.20 and the approximate analysis shown in 6.2, the assessed maximum frequency of the measured field is about 125 kHz.

Fig. 6.16 shows the amplitude-frequency characteristics of the current transducer. It can be seen that there is an amplitude increase for the frequencies approaching 100 kHz. The causes of the amplitude increase are still not clear. One possible explanation is the structure of the current transducer. Namely, a permanent magnet is placed on top of the sensor instead of the coil. It acts as a magnetic filter for higher frequencies of the measured field. In other words, it concentrates the lines of the measured field on the position of the sensor. The end result is that the sensor sees a larger measured field, which leads to somewhat larger "gain" of the angular sensor, Fig. 6.9.

6.5.2 Low bandwidth current transducer

The transfer characteristics of the current transducer with the magnetic sensor operating at 200 kHz scanning frequency is given in Fig. 6.17. The nonlinearity is smaller than 1.5 % over the range - 200 to 200 A.

111

Figure 6.16: Amplitude-frequency characteristics of the current transducer for $f_{\mathrm{scan}}= 1$ MHz and $B_{\mathrm{ref}}= 20$ mT

Figure 6.17: Transfer characteristics of the current transducer for $f_{\mathrm{scan}}= 200$ kHz and $B_{\mathrm{ref}}= 2.5$ mT
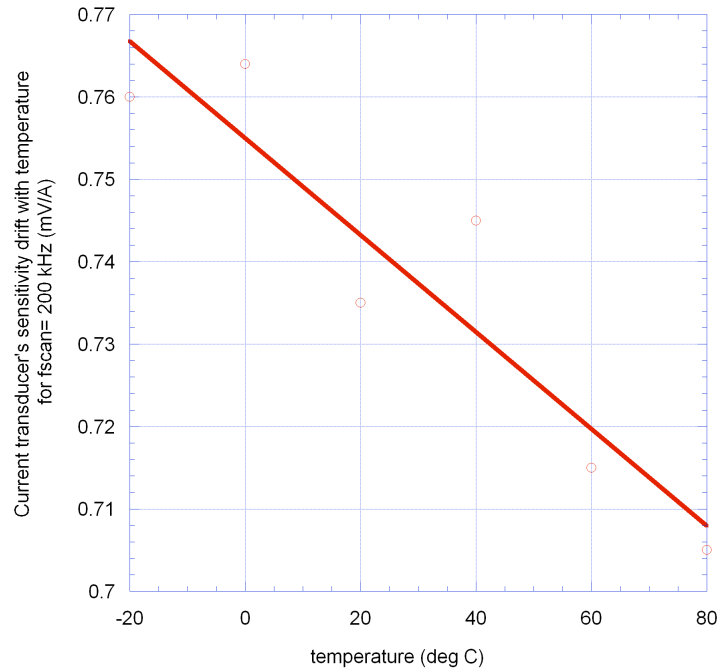
Figure 6.18: Sensitivity vs. temperature of the current transducer for f_{scan}= 200 kHz and B_{ref}= 60 mT

The sensitivity drift with temperature was about 4 %/K for the reference field of 2.5 mT created by the coil. The clock signal for the tangent converter was supplied from an external function generator.

The use of a permanent magnet instead of the reference coil reduced the sensitivity drift down to 0.7%/K, Fig. 6.18. It should be noted here that this sensitivity drift is the same order of magnitude as the sensitivity drift of the magnetic sensors based on horizontal Hall devices.

The scanning frequency of 200 kHz would allow measuring AC fields up to 100 kHz, but the bandpass filter in the angular sensor limits the bandwidth. The bandwidth of the bandpass filter is 48 kHz. The magnitude of the measured and reference fields are 5 mT and 20 mT, respectively. According to Eqn 6.20 and the approximate analysis shown in 6.2, the maximum frequency of the measured field is approximately about 18 kHz. The amplitude-frequency characteristics is shown in Fig. 6.19.

The response of the current transducer to the current pulse is shown in Fig. 6.20. The peak current value is 2.8 kA which corresponds to the slew-rate of 14 MA/s. The current 2.8 kA through the bus bar corresponds to the measured field of about 80 mT. Since the reference field is 20 mT, the maximum angle enclosed is 75.9 º, which leads to saturation of the tangent converter. One positive feature of this concept is that the increase of the reference field extends the dynamic range of the current transducer. The dynamic range of this current transducer is the highest dynamic range for a low cost current transducer available on market.
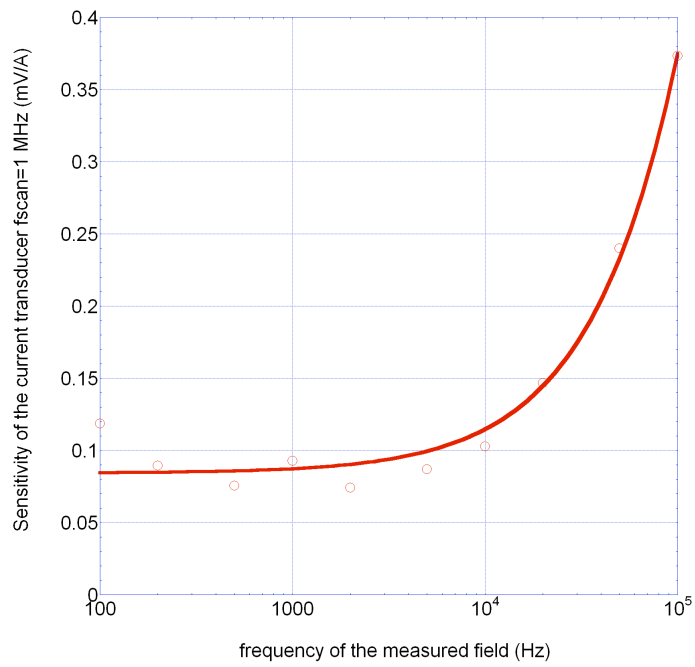
113
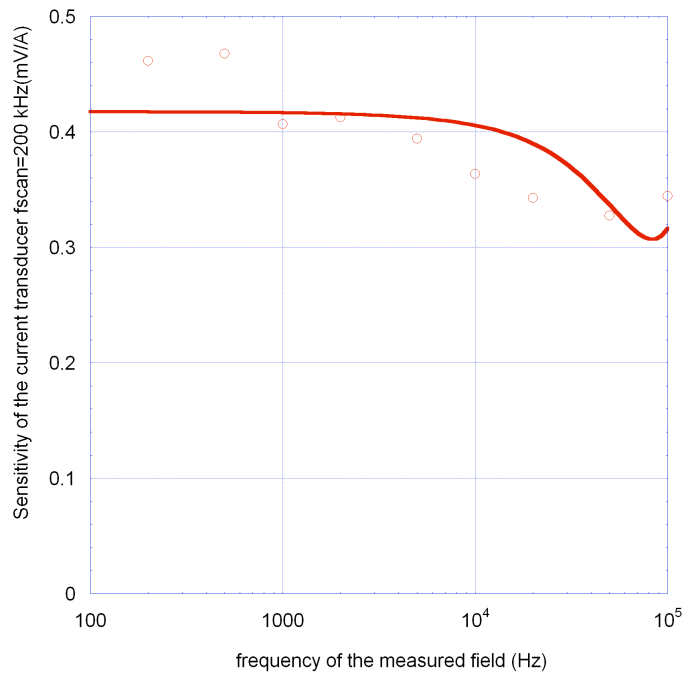
Figure 6.19: Amplitude-frequency characteristics of the current transducer for $f_{\text{scan}}= 200$ kHz and $B_{\text{ref}}= 20$ mT

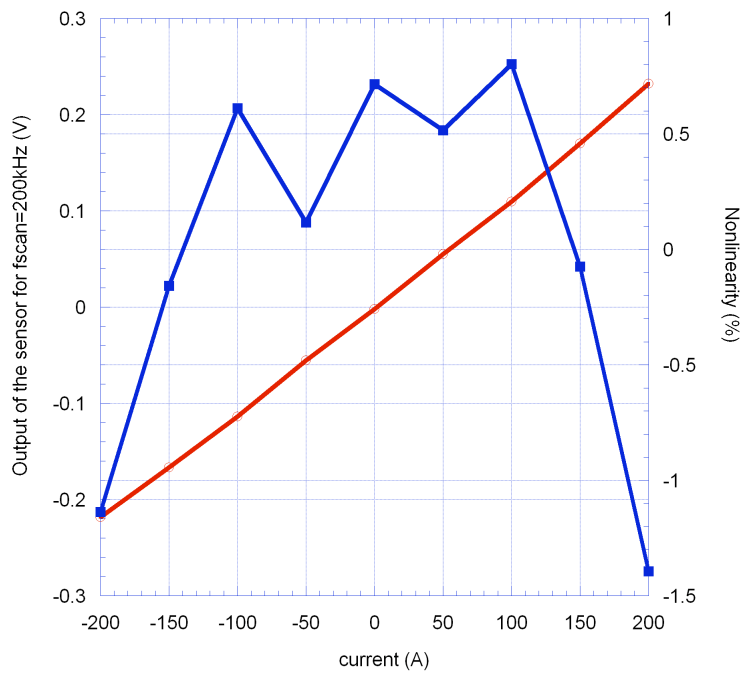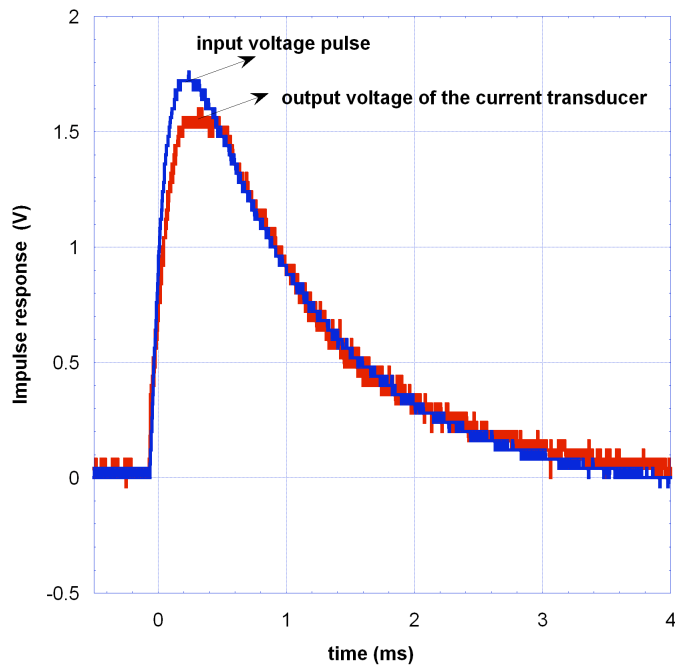Figure 6.20: Response of the current transducer to the current pulse for $f_{\text{scan}}= 200$ kHz and $B_{\text{ref}}= 20$ mT . The amplitude of the current pulse corresponds to the 2.8 kA, whereas its slew-rate is 14 MA/s

6.6   Conclusions and outlook

In this chapter we proved the feasibility of building a current transducer based on a novel concept with the 8CVHD as the sensing device. The initial measurement results of the current transducer's characteristics such as linearity and frequency response are encouraging.

The remaining challenge is the sensitivity drift with temperature. The angular sensors function well for magnetic fields above 60 mT (this is the order of magnitude of the diametrically magnetized magnets used in angular measurements). However, there is still room to optimize the magnetic angular sensor for low magnetic fields. It can be further optimized both on the front end level and the topology level. On the front end level, the miniaturized 8CVHD can be replaced by an optimized 8CVHD described in Chapter 2 having a higher current-related sensitivity. This would increase the signal-to-offset ratio, without substantial change of the front-end's bandwidth (Chapter 3). At the same time, signal-to-offset drift will be increased leading to a lower overall drift of sensitivity. On the system level, the two signal conditioning chains can be interchanged in order to improve their matching. This can be done by placing an additional modulation block in front of the preamplifier, and a demodulation block before comparators.

Chapter 7

Conclusions and Outlook

In this thesis we investigated the limits of the CVHD in terms of the minimum number of contacts and maximum operating frequency. We focused on bandwidth increase with satisfying accuracy in Hall sensors based on the 8CVHD. The optimization of the sensors was done on three structural levels: device level, device-interface electronics level and the system topology level.

On the device level, we have designed and tested the 8-contact circular vertical Hall device (8CVHD) as an ultimate miniaturization of the 64-contact circular vertical Hall device. The sensitivity of a π-curved 5-contact vertical Hall device, which is a unit cell of the 8CVHD, is about 30 % less than the sensitivity of a straight 5-contact vertical Hall device. The offset components, the DC offset and the first harmonic of offset, increase when the number of contacts is reduced. Nevertheless, it was shown that this is not the case for the 8CVHD. Though the geometry of the device leads to a loss in sensitivity, it offers possibility of biasing the whole device in all sensing phase. It is this symmetry that leads to a more efficient offset voltage reduction. The end result is that the residual offset of the 8CVHD is comparable to the offset of the CVHD with a much larger number of contacts.

The remaining challenge for the 8CVHD is further optimization towards higher sensitivity and lower offset voltage. The valid explanation for the sensitivity to the perpendicular magnetic field has yet to be found. The 8CVHD might be optimized towards a compact three-axis device. A more viable use of the third sensing axis would be some kind of self-calibration of the device.

On the device-interface electronics level, we studied the standard case of a horizontal Hall device in a system employing spinning current method. We have shown that both the design of a Hall device and the interface electronics are crucial to increasing bandwidth. Both the device and interface electronics determine contribution of voltage spikes to the overall sensor's accuracy in CMOS integrated Hall sensors. The model of the horizontal Hall device was then extended and applied to the specific case of the 8CVHD. It was shown that in the case of the 8CVHD the voltage spikes and the useful Hall signal can be frequency separated by the proposed Hall voltage retrieval. This is not the case in a traditional Hall sensor topology.

Three solutions to tackling the challenge of increasing the spinning frequency while maintaining the accuracy in the sensors based on the 8CVHD were presented. The first one is a novel solution relying on the high input capacitance of the preamplifier which together with the on-resistance of the sensing switch filters out the voltage spikes. The second solution examines the partial guard band to remove a part of the spikes' energy without compromising the high spinning frequency. The third solution is based on the cancellation of the voltage spikes by the clockwise and counterclockwise spinning current method on two devices. The novelty with respect to the previous similar solutions lies in the additional pair of the clockwise and counterclockwise devices. The spinning current method is applied with a time shift on the additional pair of devices. The outcome is that the residual spikes are of arbitrary amplitude due to mismatches. They are distributed over the spinning phase (sensing phase for the 8CVHD) and behave like noise. These three solutions were employed in three sensors based on the 8CVHD. The third solution permits the use of the highest spinning frequency.

The first solution was employed in the 2D magnetometer based on the 8CVHD. The Hall voltage retrieval from the 8CVHD and the design of the front end allowed efficient removal of the voltage spikes. The novel system level concept for the 2D CMOS integrated magnetometer based on the 8CVHD enables common biasing, signal retrieval, dynamic cancellation of offset and low frequency noise, and front-end signal conditioning electronics for both components of the measured in-plane magnetic field vector. The separation of two channels is postponed to the point where signal levels are high and less susceptible to nonidealities and mismatches of signal conditioning electronics. The magnetometer features bandwidth up to 60 kHz, wide dynamic range 0-1.5 T, high spatial resolution, and a high measurement resolution of 300 µT over wide frequency range 0-30 kHz. The 2D magnetometer can also be used as an angular sensor with full measurement range.

On the system level, we demonstrated feasibility of a high speed CMOS integrated magnetic angle sensor based on two 8CVHDs. The novel concept of the sensor features two signal channels with two 8CVHDs carrying the information on the measured angle in the opposite phases. The use of two devices doubles the sensitivity of the sensor, though at the expense of a reduced measurement range (in present implementation). The quasi-differential structure of the sensor makes it robust to secondary influences. They are translated into "common-mode" disturbances and cancelled out on the system level. The concept together with optimized interface and signal conditioning electronics allows for dramatic increase of the sensor's bandwidth while retaining absolute accuracy and angle resolution comparable to low bandwidth sensors. The current measurement range 0-90º can be extended by using a more performant phase detector instead of a simple XOR gate. The use of an SR flip-flop with the transfer characteristics periodical in 2π would extend the measurement range to 0-180º. The use of a sequential logic phase detector having the transfer characteristics periodical in 4π would give a full range 0-360º angular sensor.

The first implementation of the high-speed magnetic angle sensor has one 8CVHD per channel. It was based on the second solution to voltage spikes reduction stated above. The average angular error was measured to be $\pm$ 4º. The sensor's theoretical bandwidth for this angular error is about 300 kHz. The measurements have shown that the sensor achieves tracking the angle of the in-plane magnetic vector oscillating at 200 kHz, or equivalently 12 000 000 rpm. The state-of-the art CMOS integrated magnetic angle sensors are at 11 000 rpm, but covering a full measurement range.

The second implementation of the high-speed magnetic angle sensor has an array of 8CVHDs per channel. It is based on the second solution to voltage spikes reduction. The absolute angular error was reduced in the second implementation down to an average $\pm$ 1.5º. The bandwidth of the sensor was increased to about 500 kHz. It should be noted here that the spinning frequency, or equivalently sensing frequency, in this sensor is 32 MHz. This is to our knowledge the highest spinning frequency used in Hall sensors so far.

Finally, we proved the feasibility of building a magnetic sensor based on the 8CVHD for use in open-loop current transducers. The magnetic sensor relies on a novel concept involving the angular sensor and the tangent converter. The initial measurement results of the current transducer's characteristics such as linearity and frequency response are encouraging. The remaining challenge is the sensitivity drift with temperature. The angular sensors functions well for magnetic fields above 60 mT (this is the order of magnitude of the diametrically magnetized magnets used in angular measurements). The dominant cause of the sensitivity drift for low magnetic fields is the offset voltage drift with temperature. The offset drift and the sensitivity drift are two distinct phenomena in one-axis devices. In the CVHDs they are intertwined, as shown in Chapter 6. The magnetic sensor can be further optimized for low fields. On the front end level, the use of a device with a higher current-related sensitivity would increase the signal-to-offset ratio. On the system level, the two signal conditioning chains can be interchanged in order to improve their matching. This can be done by placing an additional modulation block in front of the preamplifier, and a demodulation block before comparators. In addition, each building block of the signal conditioning electronics can be temperature compensated on its own and further optimized.

The CMOS Hall sensors designed and verified during the thesis were proof of concepts. They are in no way the ultimate achievements of the devices or concepts used.

References

[1] http://www.isuppli.com/MEMS-and Sensors/News/Pages/Silicon-Magnetic-Sensor-Market-Offers-Attractive-Growth.aspx. (2011)

[2] B. Rezavi, *Design of Analog CMOS Integrated Circuits.* McGraw-Hill International Edition, 2001.

[3] R. S. Popovic, *Hall effect devices*, 2nd ed. IOP Publishing, 2004.

[4] E. Schurig, "Highly sensitive vertical hall sensors in cmos technology," Ph.D. dissertation, EPFL, 2004.

[5] S. Reymond, P. Kejik, and R. Popovic, "True 2D CMOS integrated Hall sensor," in *Book of abstracts of IEEE SENSORS Conference*, 2007.

[6] E. Hall, "On a new action of the magnet on electric current," *Am. J. Math*, vol. 2, pp. 287–92, 1879.

[7] R. S. Popovic and M. Banjevic, "High resolution Hall effect magnetic transducers," in *International Autumn School on High Sensitivity Magnetometers*, 2007.

[8] J. T. Maupin and M. L. Geske, *The Hall effect and its Applications.* New York: Plenum, 1980, ch. The Hall effect in silicon circuits.

[9] S. G. T. et al., "Method for the compensation of the nonequipotental voltage in the Hall voltage and means for its realization," German Patent Application 2333080, 1973.

[10] H. P. Hohe, N. Weber, and D. Seitzer, "Sensor Topology for Offset Reduction in Hall-Effect Devices," in *Proceedings of Eurosensors XIII*, 1999, pp. 605–608.

[11] A. Bilotti, G. Monreal, and R.Vig, "Monolithic Magnetic Hall Sensor Using Dynamic Quadrature Offset Cancellation," *IEEE Journal of Solid-State Circuits*, vol. 32, no. 6, June 1997.

[12] R. S. Popovic, Z. Randjelovic, and D. Manic, "Integrated Hall-effect magnetic sensors," *Sensors and Actuators A*, vol. 91, pp. 46–50, 2001.

[13] P. Gray, P. Hurst, S. Lewis, and R. Meyer, *Analysis and design of analog Integrated circuits*, fourth edition ed. John Wiley and Sons, 2001.

[14] Z. Randjelovic, "Low-power high sensitivity integrated Hall magnetic sensor microsystems," Ph.D. dissertation, EPFL, no 2198, 2000.

[15] M. Demierre, "Improvements of CMOS Hall microsystems and application for angular position measurements," Ph.D. dissertation, EPFL, no 2844, 2003.

[16] M. Pastre, "Methodology for the digital calibration of analog circuits and systems: application to a Hall sensor microsystem," Ph.D. dissertation, EPFL, no 3210, 2005.

[17] C. C. Enz and G. C. Temes, "Circuit techniques for Reducing the Effects of Op-Amp Imperfections: Autozeroing, Correlated Double Sampling, and Chopper Stabilization," in *Proceedings of the IEEE*, vol. 84, no. 11, Nov 1996.

[18] P. E. Allen and D. R. Holberg, *CMOS Analog Circuit Design*, 2nd ed. Oxford University Press, 2002.

[19] A. Bakker, A. Bellekom, S. Middelhoek, and J. H. Huijsing, "Low offset low noise 3.5 mV CMOS spinning current Hall effect sensor with integrated chopper amplifier," in *Proceedings of the XIII Europen Conference on Solid-State Tranducers, Hague*, September 1999.

[20] J. C. van der Meer, F. R. Riedijk, P. C. de Jong, E. A. van Kampen, M. J. Meekel, and J. H. Huijsing, "A fully integrated CMOS Hall sensor with a 3.65 uT 3sigma offset for compass applications," in *Proceedings of IEEE International Solid-State Circuits Conference*, 2005.

[21] V. Frick, L. Hebrard, P. Poure, and F. Braun, "CMOS Microsystem Front-End for MicroTesla Resolution Magnetic Field Measurements," *Analog Integrated Circuits and Signal Processing*, vol. 36, pp. 165–174, 2003.

[22] M. Motz, U. Ausserlechner, W. Scherr, and E. Katzmaier, "An Integrated Hall Sensor Platform Design for Position, Angle and Current Sensing," in *Proceedings of IEEE Sensors*, 2006.

[23] P. Kejik, E. Schurig, F. Bergsma, and R. Popovic, "First fully CMOS-integrated 3D Hall probe," in *Proceedings of the 13th International Conference on Solid-State Sensors, Actuators and Microsystems*, 2005.

[24] J. Pascal, L. Hebrard, V. Frick, J. P. Blonde, J. Felblinger, and J. Oster, "3D Hall probe in standard CMOS technology for magnetic field monitoring in MRI environment," in *Proceedings of European Magnetic Sensors and Actuators Conference (EMSA '08)*, 2008.

[25] R. Popovic, P. Drljaca, and P. Kejik, "CMOS magnetic sensors with integrated ferromagnetic parts," *Sensors and Actuators A*, pp. 94–99, 2006.

[26] W. D. Jones, "A compass in every smartphone," IEEE Spectrum, February 2010.

[27] "AK8975B by Asahi Kasei Microdevices," Datasheet 2010.

[28] J. Trontelj, O. Roman, and A. Pletersek, "Integrated circuit with a magnetic field sensor," EP19940118310, 1995.

[29] P. Simon, P. de Vries, and S. Middelhoek, "Autocalibration of silicon hall devices," in *Proceedings of TRANSDUCERS*, 1995, pp. 337–240.

[30] M. Pastre, H. Blanchard, and M. Kayal, "Continuously calibrated magnetic field sensor," EP 137898 A1.

[31] P. Kejik, S. Reymond, and R. S. Popovic, "Circular hall transducer for angular position sensing," in *Digest of technical papers vol.2 for TRANSDUCERS '07 and XXI Eurosensors Conference*, 2007, pp. 2593–2596.

[32] ——, "Ultra low-power angular position sensor for high-speed portable applications," in *IEEE Sensors Conference*, 2009.

[33] W. Thomson, "On the effects of magnetisation on the electric conductivity of metal," vol. A146, pp. 736–51, 1856.

[34] S. Sze, *Semiconductor Devices, Physics and Technology*, 2nd ed. John Wiley and Sons.

[35] R. S. Popovic, "The Vertical Hall-effect Device," *IEEE Electron Device Letters*, vol. 5, no. 9, 1984.

[36] C. Schott, "Accurate magnetic field transducers based on silicon Hall sensors," Ph.D. dissertation, EPFL, 1999.

[37] F. Burger, "High precision miniaturized magnetic angular encoder," Ph.D. dissertation, EPFL, 2000.

[38] R. S. Vanha, F. Kroener, T. Olbrich, R. Baresch, and H. Baltes, "Trench-Hall devices," *Journal of Microelectromechanical Systems*, vol. 9, 2000.

[39] P. Besse, C. Schott, and R. Popovic, "Analytical Study of Vertical Hall (VH)-Devices Using an Adapted Conform Mapping Technique," in *Technical Proceedings of the 1998 International Conference on Modeling and Simulation of Microsystems*, 1998.

[40] U. Falk, "A symmetrical vertical Hall-effect device," *Sensors and Actuators A: Physical*, vol. 22, pp. 751–753, June 1989.

[41] E. Schurig, C. Schott, P.-A. Besse, M. Demierre, and R. S. Popovic, "0.2 mt residual offset of cmos integrated vertical hall sensors," *Sensors and Actuators A: Physical*, vol. 110, pp. 98–104, 2004.

[42] J. Pascal, L. Hebrard, V. Frick, J.-B. Kammerer, and J.-P. Blonde, "First vertical Hall device in standard 0.35 um CMOS technology," *Sensors and Actuators A: Physical*, vol. 147, pp. 41–46, 2009.

[43] J. Pascal, L.Hebrard, V. Frick, J.-B. Kammerer, and J.-P. Blonde, "Intrinsic limits of the sensitivity of CMOS integrated vertical Hall devices," *Sensors and Actuators A: Physical*, vol. 152, pp. 21–28, 2009.

[44] M. Banjevic, S.Reymond, and R. Popovic, "On performance of series connected CMOS vertical Hall devices," in *Proceedings of the 26th IEEE International Conference on Microelectronics, MIEL*, 2008.

[45] P. Ruther, U. Schiller, W. Buesser, R. Janke, and O. Paul, "Influence of the Junction Field Effect on the Offset Voltage of Integrated Hall Plates," in *Proceedings of European Conference on Solid State Transducers*, 2002, pp. 709–710.

[46] E. Säckinger and W. Guggenbühl, "A versatile Building Block: The CMOS Differential Difference Amplifier," *IEEE Journal of Solid State Circuits*, vol. SC-22, no. 2, 1987.

[47] H. Weiss, *Structure and application of galvanomagnetic devices.* Pergamon Oxford Great Britain, 1969.

[48] R. S. Popovic, P. Kejik, and S. Reymond, "Magnetic Field Sensor Measuring a Direction of a Magnetic Field in a Plane," International Publication Number WO 2008/145662 A1.

[49] M. Banjevic, S. Reymond, and R. Popovic, "Miniaturized Circular Vertical Hall Device," *Sensor Letters*, vol. 7, pp. 325–328, 2009.

[50] Q. Huang and C. Menolfi, "A 200 nV Offset 6.5 nV/sqrt(Hz) Noise PSD 5.6 kHz Chopper Instrumentation Amplifier in 1 um Digital CMOS," in *Proceedings of IEEE International Solid-State Circuits Conference*, 2001.

[51] P. Munter, "Spinning-current method for offset reduction in silicon Hall plates," Ph.D. dissertation, Delft University Press, 1992.

[52] M. Motz, D. Draxelmayr, T.Werth, and B.Forster, "A Chopped Hall Sensor With Small Jitter and Programmable "True Power-On" Function," *IEEE Journal of Solid-State Circuits*, vol. 40, no. 7, pp. 1533–1540, July 2005.

[53] C. Eichenberger and W. Guggenbühl, "Charge Injection of Analogue CMOS Switches," *IEE Proceedings-G*, vol. 138, no. 2, 1991.

[54] P. Dimitropoulos, P. Drljaca, R. S. Popovic, and P. Chatzinikolaou, "Horizontal HALL devices: A lumped-circuit model for EDA simulators," *Sensors and Actuators A*, vol. 145-161, 2008.

[55] P. D. Dimitropoulos, S. Reymond, P. M. Drljaca, and R. Popovic, "A Completely Scalable Lumped-Circuit Model for Horizontal and Vertical Hall Devices," in *Book of abstracts of IEEE SENSORS Conference*, 2007.

[56] F. Burger, P. A. Besse, and R. Popovic, "New fully integrated 3-D silicon Hall sensor for precise angular-position measurements," *Sensors and Actuators A*, vol. 67, pp. 72–76, 1998.

[57] M. Banjevic, B. Furrer, and R. Popovic, "2D CMOS Magnetometer based on the Miniaturized Circular Vertical Hall Device," in *15th IEEE Conference on Solid-State Sensors, Actuators and Microsystems, Denver, Colorado, USA, June 21-25*, 2009.

[58] M. Metz, A. Häberli, M. Schneider, R. Steiner, C. Maier, and H. Baltes, "Contactles Angle Measurement Using Four Hall Devices on Single Chip," in *Proceedings of TRANSDUCERS*, 1997, pp. 385–388.

[59] R. Popovic, C. Schott, P. Drljaca, and R. Racz, "A new CMOS Hall angular position sensor," *Technisches Messen*, vol. 6, pp. 286–291, 2001.

[60] M. Demierre, E. Schurig, C. Schott, P. Besse, and R. S. Popovic, "Contactles 360 Â^{o} absolute angular CMOS microsystem based on vertical Hall sensors," *Sensors and Actuators A*, vol. 116, pp. 39–44, 2004.

[61] M. Kayal, F. Burger, and R. S. Popovic, "Magnetic angular encoder using an offset compensation technique," *IEEE Sensors Journal*, vol. 4, no. 6, pp. 759–763, December 2004.

[62] S. Lozanova and C. Roumenin, "Angular position device with 2D low-noise Hall microsensor," *Sensors and Actuators A*, vol. 162, pp. 167–171, 2010.

[63] P. Semiconductors, *Electronic Compass Design using KMZ51 and KMZ52, Application note AN00022*.

[64] C. Giebler, D. J. Adelerhof, A. E. T. Kuiper, J. B. A. van Zon, D. Oelgeschläger, and G. Schulz, "Robust GMR sensors for angle detection and rotation speed sensing," *Sensors and Actuators A*, vol. 91, pp. 16–20, 2001.

[65] S. M. R. Hasan, "A novel 0.7 V high sensitivity complementary differential MAGFET sensor for contactless mechatronic applications," *Sensors and Actuators A*, vol. 163, pp. 138–149, September 2010.

[66] K. Nakano, T. Takashi, and S. Kawahito, "A CMOS rotary encoder using magnetic sensor arrays," *IEEE Sensors Journal*, vol. 5, no. 5, pp. 889–894, October 2005.

[67] G. Malinowski, M. Hehn, F. Montaigne, A. Schuhl, C. Duret, R. Nantua, and G. Chaumontet, "Angular magnetic field sensor for automotive applications based on magnetic tunnel junctions using a current loop layout configuration," *Sensors and Actuators A*, vol. 144, pp. 263–266, 2008.

[68] R. F. Post, "A new Look at an old idea: The electromechanical battery," *Science and Technology Review University of California*, pp. 12–19, 1996.

[69] R. S. Popovic and M. Banjevic, "Magnetic field sensor measuring a direction of a magnetic field in a plane and current sensor," International patent Application, October 2009.

[70] L. Bolomey, E. Meurville, and P.Ryser, "Implantable ultra-low power DSP-based system for miniature chemico-rheological biosensors," *Procedia Chemistry 1*, pp. 1235–1238, 2009.

[71] Z. Song and D. V. Sarwate, "The frequency spectrum of pulse width modulated signals," *Signal Processing*, vol. 83, pp. 2227–2258, 2003.

[72] D. Popovic, S. Dimitrijevic, M. Blagojevic, P. Kejik, E. Schurig, and R. Popovic, "Three-axis teslameter with integrated Hall probe," *IEEE Trans. Instrumentation and Measurement*, vol. 56, pp. 1396–1402, 2007.

[73] T. H. Lee, *The Design of CMOS Radio-Frequency Integrated Circuits*, 2nd ed. Cambridge University Press, 2004.

[74] H. Meyr and G. Ascheid, *Synchronization in Digital Communications. Phase-, Frequency-Locked Loops, and Amplitude Control.* John Wiley and Sons, 1990.

[75] E. Favre and W. Teppan, "Capteurs de courant: à chacun son argument," *Mesures*, no. 763, March 2004.

[76] R. S. Popovic, "Sensor and procedure for measuring bus bar current with skin effect correction," international application number PCT/RS2007/000016, publication date 13.03.2008.

[77] J. Petr and H. LienHard, "Compensating circuit for a magnetic field sensor," US Patent 4752733, 1988.

[78] J. Trontelj, "Optimization of integrated magnetic sensor by mixed signal processing," in *Proceedings of IEEE Instrumentation and Measurement Technology Conference*, vol. 1, May 1999, pp. 299–302.

[79] B. Furrer, "Sensitivity stabilizing subsystem," EPFL, Marie Curie FP7 IHACS project, 2010.

[80] M. Blagojevic and S. Dimitrijevic, "Measurement setup for the current transducer," AD SEN-TRONIS, Marie Curie FP7 IHACS project, 2010.

CURRICULUM VITAE

——

PERSONAL DATA

Name: Mirjana Banjevic

Date of birth: 22.01.1980

Place of birth: Niksic, Montenegro

Nationality: Montenegrin

——

EDUCATION

- Graduate studies (November 2006- September 2011)

Thesis advisor: Prof. Radivoje Popovic, Ecole Polytechnique Fédérale de Lausanne (EPFL),
Switzerland

- M.Sc. Degree in Electronics, Computers and Telecommunications (2004-2006)

Faculty of Electrical Engineering, University of Montenegro, Montenegro

- B.Sc. Degree in Electrical Engineering (Dipl. Ing. in EE) (1998-2003)

Faculty of Electrical Engineering, University of Montenegro, Montenegro

- B.Sc. Degree in English Language and Literature (1998-2005)

Faculty of Philosophy, University of Montenegro, Montenegro

——

WORK EXPERIENCE

- Research and teaching assistant (2006-2011)

Ecole Polytechnique Fédérale de Lausanne (EFPL), Switzerland

- Research and teaching assistant (2004-2006)

Faculty of Electrical Engineering, University of Montenegro, Montenegro

- Research visitor (2005)

Faculty of Electrical Engineering, Institute for Electrical Measurements and Circuit Design
Group, Circuit Design Group, Vienna University of Technology, Austria

- Internship (2002)

Helsinki University of Technology, Helsinki, Finland

——

AWARDS

- EPFL Fellowship for the doctoral studies (2007)

- Royal Family Karadjordjevic Award for 100 best students in Serbia and Montenegro (2003)

——

LANGUAGES

- English: fluent

- French: fluent
- Italian: fair
- German: basic
- Serbian: mother tongue

_____

PUBLICATIONS AND INTERNAL REPORTS RELATED TO THIS PhD RESEARCH:

[1] M. Banjevic, S. Reymond, R. S. Popovic, "Characterisation of resolution of Hall devices", Technical report for Asahi Kasei Company, Japan, July 2007

[2] Radivoje S. Popovic and Mirjana Banjevic, "High resolution Hall effect magnetic transducers", 2007 International Autumn School High Sensitivity Magnetometers, Blainville-sur-Mer, France, September 23-28, 2007

[3] R. S. Popovic, S. Reymond, P. Kejik, M. Banjevic, "Integrated Magnetic Angle Sensors", 31st International Convention MIPRO, Croatia, May 2008

[4] M. Banjevic, Serge Reymond, Radivoje S. Popovic, "On performance of series connected CMOS vertical Hall devices", 26th IEEE International Conference on Microelectronics, MIEL, Serbia, May 2008

[5] M. Banjevic, S. Reymond, and R. S. Popovic, "Miniaturized circular vertical Hall device", European Magnetic Sensors and Actuators Conference, June 30-July 2, 2008, Caen, France, Book of abstracts, pp. 146

[6] M. Banjevic, S. Reymond, and R. S. Popovic, Miniaturized Circular Vertical Hall Device, Sensor Letters, Volume 7, Number 3, pp. 325–328, June 2009

[7] M. Banjevic, B. Furrer, and R. S. Popovic, "2D CMOS Magnetometer based on the Miniaturized Circular Vertical Hall Device", 15th IEEE Conference on Solid-State Sensors, Actuators and Microsystems, Denver, Colorado, USA, June 21-25, 2009

[8] R. Popovic and M. Banjevic, "Magnetic Field Sensor Measuring a Direction of a Magnetic Field in a Plane and Current Sensor", International patent Application, published on 15.10.2009.

[9] M. Banjevic, B. Furrer, and R. S. Popovic,"High-speed CMOS Magnetic Angle Sensor Based on Miniaturized Circular Vertical Hall Devices", submitted to Sensors and Actuators A, Physical

[10] M. Banjevic, F. Liakou, B. Furrer, S. Dimitrijevic, M. Blagojevic, P. D. Dimitropoulos and R.S Popovic, "Open-loop CMOS current transducer with low temperature cross-sensitivity", EUROSENSORS, Athens, 4-7 September 2011

[11] M. Banjevic, B. Furrer, and R. S. Popovic, "Study on bandwidth increase in Hall sensors with spinning current method and application to Hall sensors based on the circular vertical Hall device", in preparation

[12] M. Banjevic, B. Furrer, and R. S. Popovic,"Open-loop current transducer based on the miniaturized circular vertical Hall device", in preparation

Other publications:

[13] M. Banjevic, N. Tadic, "1.5 V Rail-to-Rail Constant Gm CMOS Differential Amplifier", WSEAS Transactions on Circuits and Systems, Volume 5, Number 8, pp. 1266-1270, August 2006

[14] N Tadic, M Banjevic, F Schloegl, H. Zimmermann, "Input adapter based BiCMOS operational amplifier with rail-to-rail capability", Proceedings of 26th IEEE International Conference on Microelectronics, pp. 403-407, MIEL, Serbia, May 2008

[15] N. Tadic, M. Banjevic, F. Schloegl, and H. Zimmermann, "Rail-to-rail BiCMOS operational amplifier using input signal adapters with floating outputs", Analog Integrated Circuits and Signal Processing, Springer Publishers, pp. 433-449, Volume 63, Number 3, June 2010

[16] N. Tadic, M. Zogovic, M. Banjevic, and H. Zimmermann, "Low-Voltage CMOS Adapter Circuit Suitable for Input Rail-to-Rail Operation", International Journal of Electronics, pp. 1283-1309 , Volume 97, Issue 11, 2010